DISSERTATION
SUBMITTED TO THE
COMBINED FACULTIES FOR NATURAL SCIENCES AND MATHEMATICS
OF THE RUPERTO-CAROLA UNIVERSITY OF HEIDELBERG
FOR THE DEGREE OF
DOCTOR OF NATURAL SCIENCES

PUT FORWARD BY

MASTER PHYS. PAUL ANDREW BOLEY
BORN IN: MERRIAM, KANSAS, USA

ORAL EXAMINATION: FEBRUARY 5TH, 2013

High-resolution studies of circumstellar material around massive young stellar objects

Referees: Prof. Dr. Thomas Henning
Prof. Dr. Cornelius Dullemond

Abstract

In this thesis, I investigate the nature of circumstellar material around massive young stellar objects (MYSOs). I make extensive use of spatially-resolved observations, and examine spatial structure at scales ranging from tens of astronomical units up to nearly a parsec.

In the first of three scientific studies presented in this thesis, I present the results of a survey to observe MYSO candidates with the Very Large Telescope Interferometer at mid-infrared wavelengths, using the MIDI instrument. I consider the properties of this sample of 20 objects as a whole, and address the sources individually.

In the second study, I focus on the well-known MYSO IRAS 13481-6124. By combining interferometric data from both near- and mid-infrared wavelengths, I derive a temperature profile for the circumstellar disk around this object, which I discuss in the context of theoretical disk models.

In the third study, I examine the high-luminosity source AFGL 4176 at wavelengths of $\sim 1\ \mu$m–1 mm. I construct one-dimensional radiative transfer models of the envelope, and interpret the interferometric observations in terms of parameterized a disk model.

The observations and results presented in this thesis will be of use to future studies of MYSOs, both theoretical and observational, and provide an important groundwork for observations of such objects with the next generation of interferometric instruments at the Very Large Telescope.

Zusammenfassung

In dieser Doktorarbeit untersuche ich die Natur des zirkumstellaren Materials um sogenannte massereiche junge stellar Objekte (MYSOs). Hierzu verwende ich vorrangig Beobachtungen, die die entscheidenen Konfigurationen räumlich auflösen können. Ich untersuche diese räulichen Strukturen auf Skalen, die von einigen zehn astronomischen Einheiten bis hin zu fast einem Parsec reichen.

In der ersten der drei Studien in dieser Arbeit zeige ich die Resultate einer Multi–Objekt–Studie zu MYSO–Kandidaten. Diese beruht auf Beobachtungen im mittleren Infrarot mit dem MIDI–Instrument des sogenannten Very Large Telescope Interferometers. Ich betrachte hierbei zum einen die Eigenschaften und Trends, die sich für das Sample als ganzes ergeben, als auch die Besonderheiten einzelner Objekte aus dem Sample.

In der zweiten Untersuchung konzentriere ich mich auf das bekannte MYSO namens IRAS 13481–6124. Ich kombiniere hier interferometrische Daten aus dem nahen und mittleren Infrarot. Darauf aufbauend leite ich ein Temperaturprofil für die zirkumstellare Scheibe dieses Objektes ab, welches ich im Rahmen von modifizierten Scheibenmodellen diskutiere.

In der dritten Studie untersuche ich die sehr leuchkräftige Quelle AFGL 4176 bei Wellenlängen, die den Bereich von rund 1 μm bis zu 1 mm umspannen. Ich erstelle 1D–Strahlungstransport–Modelle der Hülle, und interpretiere die interferometrischen Beobachtungen im Rahmen eines parametrisierten Scheibenmodells.

Die in dieser Arbeit vorgestellten Beobachtungen und Resultate werden für die weitere Untersuchung von MYSOs, auf der theoretischen wie auch auf der beobachtenden Seite, nützlich sein. Sie stellen des weiteren ein wichtige Vorstudie dar für die nächste Generation von interferometrischen Instrumenten am Very Large Telescope.

Contents

Chapter 1

Introduction

Stars with masses greater than 8 $M_\odot$ (synonymous with "massive stars" in the context of this thesis) make up less than 0.4% of the initial stellar content of all stars formed during the present epoch of the universe (Kroupa, 2001). Despite this seemingly small fraction, these stars are expected to account for about 17% of the total initial stellar mass of a population of newly-formed stars. They not only exert a tremendous influence on their immediate surroundings, but also affect galactic evolution on the whole.

Nearly all massive stars form as members of stellar clusters (de Wit et al., 2004, 2005), which themselves form inside dense molecular clouds and represent the dominant form of Galactic star formation (Lada and Lada, 2003). The high effective temperatures ($\gtrsim$20 000 K) and luminosities ($\gtrsim 10^4$ $L_\odot$) of massive stars mean they can ionize large amounts of Hydrogen gas in the surrounding interstellar medium. This intense irradiation can significantly influence circumstellar disks around other cluster members in close proximity to the massive star (e.g. O'Dell et al., 1993; Fang et al., 2009), and, consequently, may even affect planet formation around these stars. More globally, the H II region created by the massive star will expand due to the increased pressure from the photoelectrons. This expansion disperses the surrounding gaseous material, which can ultimately disrupt the parent molecular cloud and halt further star formation.

The role of massive stars in the dynamics of stellar clusters is complicated. Besides harsh irradiation, dynamical interactions with massive stars may also disrupt disks around other cluster members (Olczak et al., 2012). The correlation observed between the masses of embedded stellar clusters and their most massive members (Weidner and Kroupa, 2006) suggests that massive stars may influence the overall cluster evolution, and the change in the cluster-wide gravitational potential due to dispersal of gas by massive stars may be responsible for the apparently high mortality rate of massive clusters (Stahler, 2012).

For most of their life, massive stars fuse Hydrogen into Helium in their cores. After about 10-30 Myr, these stars leave the main sequence and begin to produce progressively heavier elements in their interiors, up through Iron, through the process of stellar nucleosynthesis. Finally, the synthesis of additional heavy elements takes place when the star explodes as a supernova, which also serves to inject these elements into the interstellar (and even intergalactic) medium. These elements not only provide important building blocks for life, but also drastically change the conditions of star formation and the structure of subsequently-formed stars, by providing additional radiative cooling mechanisms (e.g Schulz, 2005; Osterbrock and Ferland, 2006).

Despite these important effects on star-forming clusters and regions, galactic evolution, and enrichment of the interstellar/intergalactic media, very little is known about how massive stars form. The difficulties of forming a massive star as a result of spherical collapse (e.g. Kahn, 1974; Wolfire and Cassinelli, 1987) can be resolved by non-spherical geometries, for example, in the form of a disk (e.g. Yorke and Sonnhalter, 2002; Krumholz et al., 2007; Kuiper et al., 2012). However, many aspects of disk physics remain uncertain and/or disputed, and in this respect, observations which can constrain theoretical models are especially important. For a recent investigation into this theoretical aspect of massive star formation, I refer to the PhD thesis of Kuiper (2009) and references therein.

The inherent rarity of massive stars is heightened by their exceptionally short lifetimes compared to solar-type stars ($\sim$ 10 Myr vs. $\sim$ 10 Gyr): the small fraction of stars formed with masses $\gtrsim$8 $M_\odot$ is decreased even further for populations of evolved stars, as the massive stars explode as supernova fairly quickly. One of the most pertinent consequences of this rarity is that typical distances to young massive stars often exceed 1 kpc; thus, spatially resolving such objects is only possible using techniques which provide extremely high spatial resolution (i.e., better than 100 mas).

This thesis represents over three years of effort devoted to investigations of young massive stars in the course of my doctoral studies. In Chapter 2, I review both the historical and present-day state of research into massive stars and young stellar objects, and set the context for the present study. Then, in Chapter 3, I provide an introduction to interferometric observables and instruments. Much of the research presented in this thesis is based on observational material obtained with long-baseline optical/infrared interferometers, and the conventions, strengths and limitations of such techniques may be unfamiliar to the reader. Chapter 3 also describes the Very Large Telescope Interferometer, which was used to obtain most of the observational data presented in this thesis.

The three scientific studies which form the core of my doctoral research are presented in Chapters 4–6. Chapter 4 presents the results of a mid-infrared interferometric survey of 20 young massive stars, focusing exclusively on the interferometric observations with the use of relatively simple models. In Chapter 5, I apply a more sophisticated geometric modeling approach to one of these objects, IRAS 13481-6124, and complement the mid-infrared interferometric observations presented in Chapter 4 with previously-published near-infrared interferometric observations. Finally, in Chapter 6, I conduct a comprehensive study of another object from the sample, AFGL 4176. The multiple-wavelength approach which is used represents the current state of the art, and employs radiative transfer modeling to simultaneously reproduce both the spatial and spectral behavior of this object, at scales ranging from $\sim$ 10 AU up to half a parsec, and at near-infrared through millimeter wavelengths.

Future directions, applications and prospects for interferometric/high-resolution studies of massive young stars are discussed in Chapter 7. Finally, a summary and conclusions of the thesis are given in Chapter 8.

References

de Wit, W. J., Testi, L., Palla, F., Vanzi, L., and Zinnecker, H.: 2004, The origin of massive O-type field stars. I. A search for clusters. *Astronomy and Astrophysics* **425**, 937–948

de Wit, W. J., Testi, L., Palla, F., and Zinnecker, H.: 2005, The origin of massive O-type field stars: II. Field O stars as runaways. *Astronomy and Astrophysics* **437**, 247–255

Fang, M., van Boekel, R., Wang, W., et al.: 2009, Star and protoplanetary disk properties in Orion's suburbs. *Astronomy and Astrophysics* **504**, 461–489

Kahn, F. D.: 1974, Cocoons around early-type stars. *Astronomy and Astrophysics* **37**, 149–162

Kroupa, P.: 2001, On the variation of the initial mass function. *Monthly Notices of the Royal Astronomical Society* **322**, 231–246

Krumholz, M. R., Klein, R. I., and McKee, C. F.: 2007, Radiation-Hydrodynamic Simulations of Collapse and Fragmentation in Massive Protostellar Cores. *Astrophysical Journal* **656**, 959–979

Kuiper, R., Klahr, H., Beuther, H., and Henning, T.: 2012, A solution to the radiation pressure problem in the formation of massive stars. *arXiv 1211.7064*

Kuiper, R. G.: 2009, *Modeling the formation of massive stars*, *Ph.D. thesis*, Ruperto-Carola University of Heidelberg

Lada, C. J. and Lada, E. A.: 2003, Embedded Clusters in Molecular Clouds. *Annual Review of Astronomy and Astrophysics* **41**, 57–115

O'Dell, C. R., Wen, Z., and Hu, X.: 1993, Discovery of new objects in the Orion nebula on HST images - Shocks, compact sources, and protoplanetary disks. *Astrophysical Journal* **410**, 696–700

Olczak, C., Spurzem, R., Henning, T., et al.: 2012, Dynamics in Young Star Clusters: From Planets to Massive Stars, in *Advances in Computational Astrophysics: Methods, Tools, and Outcome*, R. Capuzzo-Dolcetta, M. Limongi, and A. Tornambè (eds.), Vol. 453 of *Astronomical Society of the Pacific Conference Series*, p. 241

Osterbrock, D. E. and Ferland, G. J.: 2006, *Astrophysics of gaseous nebulae and active galactic nuclei*, University Science Books, Sausalito, CA

Schulz, N. S.: 2005, *From Dust To Stars: Studies of the Formation and Early Evolution of Stars*, Praxis Publishing Ltd., Chichester, UK

Stahler, S. W.: 2012, The birth and death of star clusters in the milky way. *Physics Today* **65(10)**, 46–52

Weidner, C. and Kroupa, P.: 2006, The maximum stellar mass, star-cluster formation and composite stellar populations. *Monthly Notices of the Royal Astronomical Society* **365**, 1333–1347

Wolfire, M. G. and Cassinelli, J. P.: 1987, Conditions for the formation of massive stars. *Astrophysical Journal* **319**, 850–867

Yorke, H. W. and Sonnhalter, C.: 2002, On the Formation of Massive Stars. *Astrophysical Journal* **569**, 846–862

Chapter 2

Massive young stellar objects

This thesis is devoted to the study of massive young stellar objects (massive YSOs, MYSOs). This empirically-established class of highly-luminous infrared objects is thought to represent young massive stars, possibly (but not necessarily) Hydrogen-burning, surrounded by circumstellar envelopes and/or disks. In this chapter, I provide a brief overview of the historical developments, as well as observational and physical characteristics of these objects. I also summarize past and present directions in research of these objects, both theoretical and observational, by introducing a few key studies.

2.1 MYSOs: An early history

An early attempt to identify contracting intermediate- and high-mass stars in nature was given by Herbig (1960). In this work, three simple criteria were proposed to observationally identify stars in the mass range of ~ 3–$20\ \mathrm{M}_\odot$ which are still in the process of accreting material: 1) the star must have a spectral type of B or A (thus constraining the mass range); 2) the star must show emission lines in its optical spectrum (indicative of excited circumstellar material); 3) the star illuminates nearby dense material as a reflection nebulosity (i.e., physical association with dense interstellar material).

These criteria lead to the definition of a new class of young stars, known today as Herbig Ae/Be (HAeBe) stars. These objects have been, and continue to be, intensively studied in their own right (see, for example, the work by Hillenbrand et al. (1992), the review by Waters and Waelkens (1998), and the recent work by Alecian et al. (2012)). However, the definition of HAeBe stars is centric to optical wavelengths; as a result these objects are, by definition, not heavily obscured by foreground material. Thus, envelope-dominated sources, and sources which are still embedded in their parent molecular clouds, are excluded from this class *a priori.* This point is particularly important for high-mass stars, as the timescales for both their pre-main-sequence evolution (e.g. Zinnecker and Yorke, 2007) and the destruction of their circumstellar disks (e.g. Hollenbach et al., 2000) are very short. Consequently, by the time the material from the natal molecular cloud has been dispersed (allowing the star to become visible at optical wavelengths), any evidence of how it actually formed has already been erased: i.e., there are no "Herbig Oe" stars. In order to study these earlier phases in the lives of massive stars, it is therefore necessary to move to infrared wavelengths.

One of the prototypes for a young massive star seen at infrared wavelengths is the Becklin-Neugebauer (BN) object (Becklin and Neugebauer, 1967), which is a bright infrared source located in the Orion star-forming region. That this object represents an embedded star heating a dust "cocoon" around it was demonstrated in the work by Becklin et al. (1973); this work also suggested that the interior heating source is a pre-main-sequence object or protostar, rather

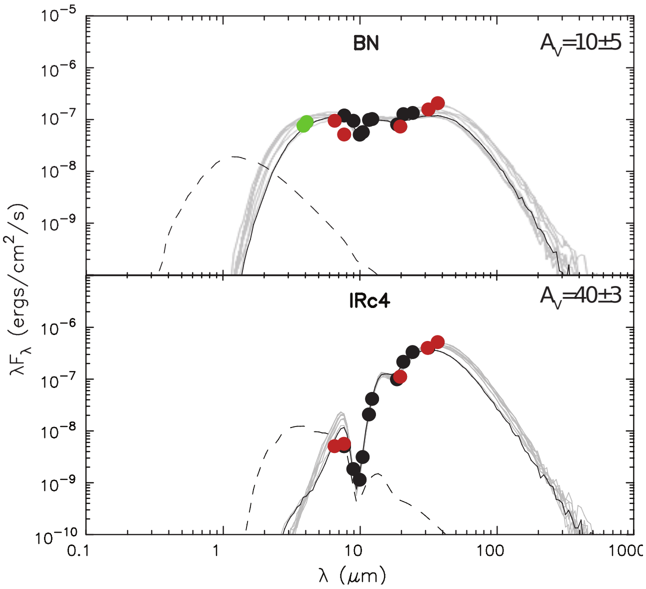

Figure 2.1: SED of Orion BN (above) and the more embedded source Irc4 (below). The gray lines show radiative transfer fits from the Robitaille et al. (2006) grid. Figure adapted from De Buizer et al. (2012).

than an evolved star. Support for this hypothesis was given via modeling of the infrared spectral energy distribution (SED), initially by Bedijn et al. (1978); however, it should be noted that there is also a possibility that BN is a main sequence B star ejected from the Orion Nebular Cluster (Tan, 2004).

Regardless of the true nature of BN, it has been established as a *de facto* prototype for massive YSOs. Several authors began compiling lists of objects which have infrared properties similar to those of BN (Wynn-Williams, 1982; Henning et al., 1984), while initial radiative transfer models of BN-like objects showed that dust in the "cocoon" or envelope dominates their SEDs at near-infrared through sub-millimeter wavelengths (e.g. Yorke and Shustov, 1981; Gürtler and Henning, 1986).

The spectral energy distribution of BN, shown in Fig. 2.1, shows several defining characteristics of BN-type objects. First, these objects have essentially no emission at optical wavelengths. This is due to extinction by dust, as evidenced by the deep silicate absorption feature at a wavelength of 10 μm. Second, the SED shows a very broad peak at far-infrared wavelengths, typically lying at $\sim$ 50–200 μm, which arises from thermal emission from circumstellar dust. Finally, these objects are highly luminous: the integrated luminosity of BN itself, for example, is $\sim 10^4$ $L_\odot$ (Scoville et al., 1983; De Buizer et al., 2012).

With the increased availability of ground-based near- and mid-infrared observing facilities, and especially with the launch of the Infrared Astronomical Satellite (IRAS) in 1983 (Neugebauer et al., 1984), the number of MYSO candidates grew. The catalog of BN-like objects by Henning et al. (1984) was expanded by Chan et al. (1996); samples of infrared objects with or without associated ultra-compact H II regions were formed by Palla et al. (1991) and Molinari et al. (1996), and also by Walsh et al. (1997). In total, by the end of the 1990s, the number of infrared-bright MYSO candidates grew to several hundred.

Initial modeling of the spectra of some MYSOs showed the presence of H_2O and NH_3 ice (e.g Lee and Draine, 1985) around these objects. The Infrared Space Observatory (ISO), launched into a geocentric orbit in 1995, provided spectral coverage at wavelengths of 2.5–200 μm. This broad spectral range led to the discovery of many more important species around MYSOs, including CO_2 ice (Guertler et al., 1996); CH_3OH and CH_4 ices (Gürtler et al., 2002); gas-phase CO_2 (Boonman et al., 2003) and H_2O (Boonman and van Dishoeck, 2003); and abundant polycyclic aromatic hydrocarbons (PAHs; e.g. Peeters, 2002).

During this time period, nearly all studies of the infrared SEDs of MYSOs relied heavily on one-dimensional radiative transfer modeling (e.g. Gürtler and Henning, 1986; Siebenmorgen, 1993). However, a common complication of these one-dimensional models was a failure to reproduce the observed near-infrared flux levels. The first spatially-resolved observations of MYSOs (e.g. Simon et al., 1985; Dougados et al., 1993; Schertl et al., 2000) and compact H II regions (e.g. Feldt et al., 1998) at near-infrared wavelengths began to reveal the importance of substructure and asymmetries in these objects; however, even tentative two-dimensional modeling of the circumstellar environment around real MYSOs became feasible only in the next century.

2.2 Studies of MYSOs today

Much progress has been made in studies of MYSOs since the discovery of the BN object in 1967. The studies detailed above laid the foundations for a new era in MYSO research, which came to include studies of larger samples of objects, more complete wavelength coverage, and, eventually, the possibility of *spatially resolving* the compact emission around some MYSOs, using both optical and radio interferometers.

At radio wavelengths, using both single-dish and interferometric measurements, several studies (e.g. Shepherd and Churchwell, 1996; van der Tak et al., 2000; Beuther et al., 2002; Wu et al., 2004) helped to establish that dense molecular outflows are a ubiquitous feature of MYSOs. The presence of outflows around some MYSOs suggests that they may also harbor circumstellar disks, which are commonly seen around lower-mass young stars. Searches using radio interferometers eventually revealed large, rotating dusty structures (commonly referred to as "tori" in the literature) around many MYSOs (e.g. Gibb et al., 2004; Beltrán et al., 2005). Structures which seem to resemble classical disks have been reported for intermediate-mass YSOs (e.g. Shepherd et al. (2001); Cesaroni et al. (2005); Patel et al. (2005); Schreyer et al. (2006); see also the work by Comito et al. (2008)). However, unambiguous confirmation of a classical circumstellar disk around a massive star at long wavelengths is made difficult by the resolving power of existing facilities, and remains elusive to this day[1].

These studies at radio wavelengths are well-suited for tracing cold molecular material, but to study the inner regions of circumstellar disks, where heated dust is the dominant source of emission, it is necessary to move to near- and mid-infrared wavelengths. To this end, a powerful tool for understanding the infrared SEDs of YSOs was presented by Robitaille et al. (2006), who pre-computed a grid of 200 000 two-dimensional radiative transfer models of YSOs at various evolutionary stages, for stellar masses in the range 0.1–50 $M_\odot$. This tool is particularly useful for sources which are not envelope-dominated (e.g. Robitaille et al., 2007), however, as noted by Thamm et al. (1994) and Men'shchikov and Henning (1997), SED fitting of YSOs can be a very degenerate process. In particular, the dangers of using the aforementioned grid for massive YSOs were reiterated by Robitaille (2008).

Nonetheless, the degeneracy of SED fitting can be partially alleviated by making use of spatially-resolved observations. Some studies (e.g. de Wit et al., 2009) have attempted to do this with single-telescope imaging at wavelengths dominated by dust emission, however the large distances to most MYSOs mean these objects are, at best, only marginally resolved by

---

[1] This situation may be expected to change imminently, with the exploitation of the new Atacama Large Millimeter Array.

single telescopes. Other studies (e.g. Wheelwright et al., 2010; Ilee et al., 2012) have applied the technique of spectroastrometry to trace the kinematics of excited gas close to massive stars. This technique is particularly useful, because it can provide the spatial resolution needed to resolve structures down to ~ 1 AU (Wheelwright et al., 2010).

Finally, beginning in 2007, there have been a number of case studies using long-baseline interferometry at near-/mid-infrared wavelengths. Many of these studies (e.g. Linz et al., 2009; de Wit et al., 2010; Follert et al., 2010; Kraus et al., 2010; de Wit et al., 2011; Grellmann et al., 2011) have used the interferometric observations as a check on the plausibility of the best-fit SED models returned by the Robitaille et al. (2006) grid of radiative transfer models. A select few case studies (e.g. de Wit et al., 2007; Acke et al., 2008; Vehoff et al., 2010) have attempted to include the interferometric data more directly into various aspects of the model-fitting process. However, a comprehensive understanding of the circumstellar environment of MYSOs on scales of $\lesssim 100$ AU, as well as unified models for these objects which incorporate observations spanning orders of magnitude (~ 100–$100\,000$ AU), are lacking.

References

Acke, B., Verhoelst, T., van den Ancker, M. E., et al.: 2008, MWC 297: a young high-mass star rotating at critical velocity. *Astronomy and Astrophysics* **485**, 209–221

Alecian, E., Wade, G. A., Catala, C., et al.: 2012, A high-resolution spectropolarimetric survey of Herbig Ae/Be stars - I. Observations and measurements. *arXiv 1211.2907*

Becklin, E. E. and Neugebauer, G.: 1967, Observations of an Infrared Star in the Orion Nebula. *Astrophysical Journal* **147**, 799

Becklin, E. E., Neugebauer, G., and Wynn-Williams, C. G.: 1973, On the Nature of the Infrared Point Source in the Orion Nebula. *Astrophysical Journal Letters* **182**, L7

Bedijn, P. J., de Jong, T., and Habing, H. J.: 1978, Model infrared spectra for accreting stars. *Astronomy and Astrophysics* **69**, 73–84

Beltrán, M. T., Cesaroni, R., Neri, R., et al.: 2005, A detailed study of the rotating toroids in G31.41+0.31 and G24.78+0.08. *Astronomy and Astrophysics* **435**, 901–925

Beuther, H., Schilke, P., Sridharan, T. K., et al.: 2002, Massive molecular outflows. *Astronomy and Astrophysics* **383**, 892–904

Boonman, A. M. S. and van Dishoeck, E. F.: 2003, Abundant gas-phase H_2O in absorption toward massive protostars. *Astronomy and Astrophysics* **403**, 1003–1010

Boonman, A. M. S., van Dishoeck, E. F., Lahuis, F., and Doty, S. D.: 2003, Gas-phase CO_2 toward massive protostars. *Astronomy and Astrophysics* **399**, 1063–1072

Cesaroni, R., Neri, R., Olmi, L., et al.: 2005, A study of the Keplerian accretion disk and precessing outflow in the massive protostar IRAS 20126+4104. *Astronomy and Astrophysics* **434**, 1039–1054

Chan, S. J., Henning, T., and Schreyer, K.: 1996, A catalogue of massive young stellar objects.. *Astronomy and Astrophysics Supplement Series* **115**, 285

Comito, C., Schilke, P., Endesfelder, U., Jiménez-Serra, I., and Martín-Pintado, J.: 2008, High-resolution mm interferometry and the search for massive protostellar disks: the case of Cep-A HW2. *Astrophysics and Space Science* **313**, 59–63

De Buizer, J. M., Morris, M. R., Becklin, E. E., et al.: 2012, First Science Observations with SOFIA/FORCAST: 6-37 μm Imaging of Orion BN/KL. *Astrophysical Journal Letters* **749**, L23

de Wit, W. J., Hoare, M. G., Fujiyoshi, T., et al.: 2009, Resolved 24.5 micron emission from massive young stellar objects. *Astronomy and Astrophysics* **494**, 157–178

de Wit, W. J., Hoare, M. G., Oudmaijer, R. D., and Lumsden, S. L.: 2010, The origin of mid-infrared emission in massive young stellar objects: multi-baseline VLTI observations of W33A. *Astronomy and Astrophysics* **515**, A45

de Wit, W. J., Hoare, M. G., Oudmaijer, R. D., and Mottram, J. C.: 2007, VLTI/MIDI 10 μm Interferometry of the Forming Massive Star W33A. *Astrophysical Journal Letters* **671**, L169–L172 de Wit, W. J., Hoare, M. G., Oudmaijer, R. D., et al.: 2011, Mid-infrared interferometry towards the massive young stellar object CRL 2136: inside the dust rim. *Astronomy and Astrophysics* **526**, L5

Dougados, C., Lena, P., Ridgway, S. T., Christou, J. C., and Probst, R. G.: 1993, Near-infrared imaging of the Becklin-Neugebauer-IRc2 region in Orion with subarcsecond resolution. *Astrophysical Journal* **406**, 112–121

Feldt, M., Henning, T., Lagage, P. O., et al.: 1998, The Chamaeleon infrared nebula revisited. Infrared imaging and spectroscopy of a young stellar object. *Astronomy and Astrophysics* **332**, 849–856

Follert, R., Linz, H., Stecklum, B., et al.: 2010, Mid-infrared interferometry of massive young stellar objects. II. Evidence for a circumstellar disk surrounding the Kleinmann-Wright object. *Astronomy and Astrophysics* **522**, A17

Gibb, A. G., Hoare, M. G., Mundy, L. G., and Wyrowski, F.: 2004, A Search for Disks around Massive Young Stellar Objects, in *Star Formation at High Angular Resolution*, M. G. Burton, R. Jayawardhana, and T. L. Bourke (eds.), Vol. 221 of *IAU Symposium*, p. 425

Grellmann, R., Ratzka, T., Kraus, S., et al.: 2011, Mid-infrared interferometry of the massive young stellar object NGC 2264 IRS 1. *Astronomy and Astrophysics* **532**, A109

Guertler, J., Henning, T., Koempe, C., et al.: 1996, Detection of an absorption feature at the position of the 4.27-μm band of solid CO_2_.. *Astronomy and Astrophysics* **315**, L189–L192

Gürtler, J. and Henning, T.: 1986, Circumstellar dust shells around very young and massive stars. *Astrophysics and Space Science* **128**, 163–175

Gürtler, J., Klaas, U., Henning, T., et al.: 2002, Detection of solid ammonia, methanol, and methane with ISOPHOT.. *Astronomy and Astrophysics* **390**, 1075–1087

Henning, T., Friedemann, C., Gürtler, J., and Dorschner, J.: 1984, A catalogue of extremely young, massive and compact infrared objects. *Astronomische Nachrichten* **305**, 67–78

Herbig, G. H.: 1960, The Spectra of Be- and Ae-TYPE Stars Associated with Nebulosity. *Astrophysical Journal Supplement Series* **4**, 337

Hillenbrand, L. A., Strom, S. E., Vrba, F. J., and Keene, J.: 1992, Herbig Ae/Be stars - Intermediate-mass stars surrounded by massive circumstellar accretion disks. *Astrophysical Journal* **397**, 613–643

Hollenbach, D. J., Yorke, H. W., and Johnstone, D.: 2000, Disk Dispersal around Young Stars, in *Protostars and Planets IV*, V. Mannings, A. P. Boss, and S. S. Russell (eds.), pp 401–428

Ilee, J. D., Wheelwright, H. E., Oudmaijer, R. D., et al.: 2012, CO bandhead emission of massive young stellar objects: determining disc properties. *arXiv 1212.0554*

Kraus, S., Hofmann, K.-H., Menten, K. M., et al.: 2010, A hot compact dust disk around a massive young stellar object. *Nature* **466**, 339–342

Lee, H. M. and Draine, B. T.: 1985, Infrared extinction and polarization due to partially aligned spheroidal grains - Models for the dust toward the BN object. *Astrophysical Journal* **290**, 211–228

Linz, H., Henning, T., Feldt, M., et al.: 2009, Mid-infrared interferometry of massive young stellar objects. I. VLTI and Subaru observations of the enigmatic object M8E-IR. *Astronomy and Astrophysics* **505**, 655–661

Men'shchikov, A. B. and Henning, T.: 1997, Radiation transfer in circumstellar disks.. *Astronomy and Astrophysics* **318**, 879–907

Molinari, S., Brand, J., Cesaroni, R., and Palla, F.: 1996, A search for precursors of ultracompact HII regions in a sample of luminous IRAS sources. I. Association with ammonia cores.. *Astronomy and Astrophysics* **308**, 573–587

Neugebauer, G., Habing, H. J., van Duinen, R., et al.: 1984, The Infrared Astronomical Satellite (IRAS) mission. *Astrophysical Journal Letters* **278**, L1–L6

Palla, F., Brand, J., Comoretto, G., Felli, M., and Cesaroni, R.: 1991, Water masers associated with dense molecular clouds and ultracompact H II regions. *Astronomy and Astrophysics* **246**, 249–263

Patel, N. A., Curiel, S., Sridharan, T. K., et al.: 2005, A disk of dust and molecular gas around a high-mass protostar. *Nature* **437**, 109–111

Peeters, E.: 2002, *Polycyclic aromatic hydrocarbons and dust in regions of massive star formation PAHs and dust in HII regions*, *Ph.D. thesis*, Proefschrift, Rijksuniversiteit Groningen

Robitaille, T. P.: 2008, SED Modeling of Young Massive Stars, in *Massive Star Formation: Observations Confront Theory*, H. Beuther, H. Linz, and T. Henning (eds.), Vol. 387 of *Astronomical Society of the Pacific Conference Series*, p. 290

Robitaille, T. P., Whitney, B. A., Indebetouw, R., and Wood, K.: 2007, Interpreting Spectral Energy Distributions from Young Stellar Objects. II. Fitting Observed SEDs Using a Large Grid of Precomputed Models. *Astrophysical Journal Supplement Series* **169**, 328–352

Robitaille, T. P., Whitney, B. A., Indebetouw, R., Wood, K., and Denzmore, P.: 2006, Interpreting Spectral Energy Distributions from Young Stellar Objects. I. A Grid of 200,000 YSO Model SEDs. *Astrophysical Journal Supplement Series* **167**, 256–285

Schertl, D., Balega, Y., Hannemann, T., et al.: 2000, Diffraction-limited bispectrum speckle interferometry and speckle polarimetry of the young bipolar outflow source S140 IRS1. *Astronomy and Astrophysics* **361**, L29–L32

Schreyer, K., Semenov, D., Henning, T., and Forbrich, J.: 2006, A Rotating Disk around the Very Young Massive Star AFGL 490. *Astrophysical Journal Letters* **637**, L129–L132

Scoville, N., Kleinmann, S. G., Hall, D. N. B., and Ridgway, S. T.: 1983, The circumstellar and nebular environment of the Becklin-Neugebauer object - 2-5 micron wavelength spectroscopy. *Astrophysical Journal* **275**, 201–224

Shepherd, D. S. and Churchwell, E.: 1996, Bipolar Molecular Outflows in Massive Star Formation Regions. *Astrophysical Journal* **472**, 225

Shepherd, D. S., Claussen, M. J., and Kurtz, S. E.: 2001, Evidence for a Solar System-Size Accretion Disk Around the Massive Protostar G192.16-3.82. *Science* **292**, 1513–1518

Siebenmorgen, R.: 1993, The spectral energy distribution of star-forming regions. *Astrophysical Journal* **408**, 218–229

Simon, M., Peterson, D. M., Longmore, A. J., Storey, J. W. V., and Tokunaga, A. T.: 1985, Lunar occultation observations of M8E-IR. *Astrophysical Journal* **298**, 328–339

Tan, J. C.: 2004, The Becklin-Neugebauer Object as a Runaway B Star, Ejected 4000 Years Ago from the θ^1 Orionis C System. *Astrophysical Journal Letters* **607**, L47–L50

Thamm, E., Steinacker, J., and Henning, T.: 1994, Ambiguities of parametrized dust disk models for young stellar objects. *Astronomy and Astrophysics* **287**, 493–502

van der Tak, F. F. S., van Dishoeck, E. F., Evans, II, N. J., and Blake, G. A.: 2000, Structure and Evolution of the Envelopes of Deeply Embedded Massive Young Stars. *Astrophysical Journal* **537**, 283–303

Vehoff, S., Hummel, C. A., Monnier, J. D., et al.: 2010, Mid-infrared interferometry of the massive young stellar object NGC 3603 - IRS 9A. *Astronomy and Astrophysics* **520**, A78

Walsh, A. J., Hyland, A. R., Robinson, G., and Burton, M. G.: 1997, Studies of ultracompact HII regions - I. Methanol maser survey of IRAS-selected sources. *Monthly Notices of the Royal Astronomical Society* **291**, 261–278

Waters, L. B. F. M. and Waelkens, C.: 1998, Herbig Ae/Be Stars. *Annual Review of Astronomy and Astrophysics* **36**, 233–266

Wheelwright, H. E., Oudmaijer, R. D., de Wit, W. J., et al.: 2010, Probing discs around massive young stellar objects with CO first overtone emission. *Monthly Notices of the Royal Astronomical Society* **408**, 1840–1850

Wu, Y., Wei, Y., Zhao, M., et al.: 2004, A study of high velocity molecular outflows with an up-to-date sample. *Astronomy and Astrophysics* **426**, 503–515

Wynn-Williams, C. G.: 1982, The search for infrared protostars. *Annual Review of Astronomy and Astrophysics* **20**, 587–618

Yorke, H. W. and Shustov, B. M.: 1981, The spectral appearance of dusty protostellar envelopes. *Astronomy and Astrophysics* **98**, 125–132

Zinnecker, H. and Yorke, H. W.: 2007, Toward Understanding Massive Star Formation. *Annual Review of Astronomy and Astrophysics* **45**, 481–563

Chapter 3

Astronomical interferometry

A large part of the observational data presented in this thesis were obtained in the mid-infrared ($\sim 8 - 13\ \mu$m) wavelength range using a method called *interferometry*. This technique is highly specialized, and the fundamental quantities measured, reported and modeled in this thesis may be unfamiliar to the reader. In this chapter, I provide a brief introduction[1] to the theory of interferometry and the realities of interferometric imaging, and describe the Very Large Telescope Interferometer (VLTI) of the European Southern Observatory (ESO), which was used to obtain the majority of the interferometric observations presented in Chapters 4–6.

3.1 Introduction

One of the fundamental characteristics of nearly any astronomical observation is the *spatial* (or *angular*) *resolution* of the measurement. The spatial resolution is, broadly speaking, the angular scales for which one can meaningfully resolve details of the source structure. In general, this quantity can depend on the wavelength of the observations, the details of the instrument and detector, and, for ground-based observations, on the properties and conditions of the Earth's atmosphere.

In the context of astronomical observations, interferometry is a mode of observing where the signals from multiple telescopes (or multiple apertures from a single telescope) are combined coherently, which allows one to exceed the traditional spatial resolution limitations of single-telescope measurements. The angular resolution thus achieved can be orders of magnitude higher than is possible using the largest single telescopes, making interferometry an extremely powerful tool for probing the spatial structures of distant astrophysical objects.

This is not a new technique. That the wave nature of light implies interference phenomena will arise was been known since the time of Hooke (1665) and Huygens (1690), and diffraction patterns arising from interference were observed by Grimaldi (1665). Fizeau (1868) was the first to suggest the application of interferometric techniques to astronomy, and the first attempts at measuring stellar diameters were made by Stéphan (1874), who established an upper limit for stellar diameters of $\sim 0\farcs158$. The first successful measurements were made by Michelson and Pease (1921), who used a six-meter interferometer operating at visual wavelengths to measure the diameters of nearby giant stars. Since that time, astronomical applications of interferometry have grown to include near- and mid-infrared wavelengths with so-called optical interferometers, sub-mm through cm wavelengths with traditional radio interferometers, and even to meter wavelengths with phased-array interferometers.

---

[1] For more extensive coverage, the interested reader is referred to *Principles of long baseline interferometry* (Lawson, 2000), *An introduction to optical stellar interferometry* (Labeyrie et al., 2006) and the introductory articles by Haniff (2007a,b).

3.2 Primer to astronomical interferometry

One of the quantities most frequently referred to by interferometrists is known as the *complex visibility*, indicated as V. As the name suggests, this is a complex quantity, and not every type of interferometer can measure both the amplitude and full phase. A detailed derivation of the complex visibility is beyond the scope of this introduction (for more information, refer to the references at the beginning of this chapter), but here I merely state its relation to the image intensity distribution $I(\alpha, \beta)$, given by the van Cittert-Zernike theorem:

$$V(u, v) = \frac{\int\int I(\alpha, \beta) e^{-2\pi i(u\alpha + v\beta)} \mathrm{d}\alpha \mathrm{d}\beta}{\int\int I(\alpha, \beta) \mathrm{d}\alpha \mathrm{d}\beta}. \tag{3.1}$$

I.e., the complex visibility is the (normalized) Fourier transform of the image intensity distribution. The spatial coordinates α and β (typically measured in radians or arcseconds) have corresponding coordinates u and v (typically measured in fringe cycles/radian or fringe cycles/arcsecond) in the frequency domain, which are known as spatial frequencies. Thus, by accessing the visibility with interferometers, we learn something about the relative importance of certain spatial scales to the underlying image intensity distribution.

Just as the visibility can be expressed as the Fourier transform of the image intensity distribution, so too can the intensity distribution be described as the (inverse) Fourier transform of the visibility. Thus, if one measures the visibility $V(u, v)$ for an infinite number of spatial frequencies u and v, the original image can be recovered by taking the inverse Fourier transform of the complex visibility. For a finite (but large) number of measurements, the original image can be reconstructed using a variety of techniques; this is a routine procedure for producing high-resolution images at radio wavelengths, where current technology makes arrays with large numbers of antennas possible.

However, if the coverage of spatial frequencies (i.e., the "*uv* coverage") is sparse, as is often the case at optical/infrared wavelengths, so-called model-independent image reconstruction is impossible. On the other hand, if the underlying source structure is known (or can be supposed) *a priori*, then even a single visibility measurement may be extremely valuable.

Example: Measuring the diameter of a star with interferometry

A particularly illustrative example of the value even a single interferometric measurement can have is the determination of a star's diameter. If we make the *ansatz* that a star's intensity distribution on the sky is well described by a uniform, axisymmetric disk with a diameter Θ, then the visibility as a function of spatial frequency is given by

$$V(u, v) = 2\frac{J_1(\pi\Theta\sqrt{u^2 + v^2})}{\pi\Theta\sqrt{u^2 + v^2}} \tag{3.2}$$

(c.f. Berger and Segransan, 2007), where J_1 is the first-order Bessel function. Since this is a function of only one parameter (the disk diameter Θ), measuring the value of V for a single spatial frequency $\sqrt{u^2 + v^2}$ can, in principle, be sufficient to determine the star's diameter. The essence of this statement is expressed visually in Fig. 3.1, where the visibility amplitude $|V|$ as a function of spatial frequency is shown for a uniform disk with a diameter of 47 mas (i.e., the diameter of Betelgeuse measured by Michelson and Pease) as a black solid line. Corresponding curves for diameters of 90% and 110% of this value are shown as gray solid lines. If an appropriate spatial frequency is chosen (e.g., as indicated with the dashed line), it is a simple matter to assign a diameter to the star. On the other hand, for some spatial frequencies (e.g., the frequency indicated with a dotted line), there be many plausible diameters which give the

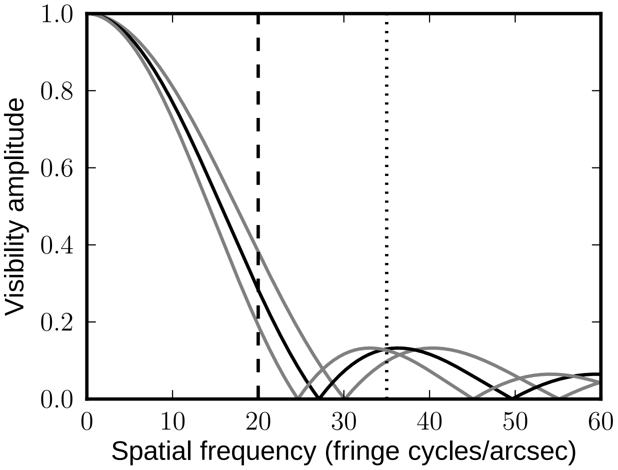

Figure 3.1: Visibility function for a uniform disk with a diameter of 47 mas (black line), and corresponding curves for diameters of 90% and 110% of this value (gray lines). The dashed line represents a spatial frequency for which the diameter can be easily determined from a single measurement of the visibility amplitude; the dotted line represents a spatial frequency for which the diameter can not be uniquely determined by a single measurement.

same visibility level, meaning there is not a unique solution for a single visibility measurement. In such cases, additional measurements which probe other spatial frequencies can be helpful[2]. Additional measurements are also important for checking the validity of our *ansatz*: for example, besides a simple uniform disk, it may be necessary to account for limb darkening, stellar companions, elongation, etc.

A musical analogy

It can be enlightening to consider the basic problem of interferometric measurements at discrete spatial frequencies in terms of a field which is closer to Earth and human experience. In the upper panel of Fig. 3.2, I show a musical score of the opening line of the classic bluegrass tune “Salt Creek.” Below that, I show the time-compressed power spectrum (i.e., the Fourier transform of the signal multiplied by its complex conjugate) of a six-second recording of this phrase, played on a mandolin. In this analogy, the musical phrase (as we perceive it with our ears) is equivalent to the image intensity pattern on the sky, and the power spectrum is equivalent to the visibility amplitude which we measure with our interferometer. The spatial frequencies u and v from Eq. 3.1 correspond directly to the acoustic frequency.

By measuring the power at specific frequencies, we can learn about the relative importance of specific musical notes to the composition. For example, by noting that the power spectrum shows peaks at frequencies corresponding the musical notes A, B, C♯, D, E, F♯ and G♯ we may conclude that the piece is probably in the key of A major or F♯ minor. If we are particularly clever with our sampling of frequencies, we may even notice the peak at G_6 (an accidental in the normal A major scale), which would tell us that the key of the piece is neither purely “major” nor “minor,” but actually in the so-called Mixolydian mode, and so has a certain “feel” to it.

Also in direct analogy to the case of astronomical interferometry, the information we extract from the Fourier transform of “Salt Creek” is of a very specific sort. We can tell the musical

---

[2] For a recent example, see the publication by Ohnaka et al. (2009), where the visibility function for Betelgeuse was measured out to the fifth lobe.

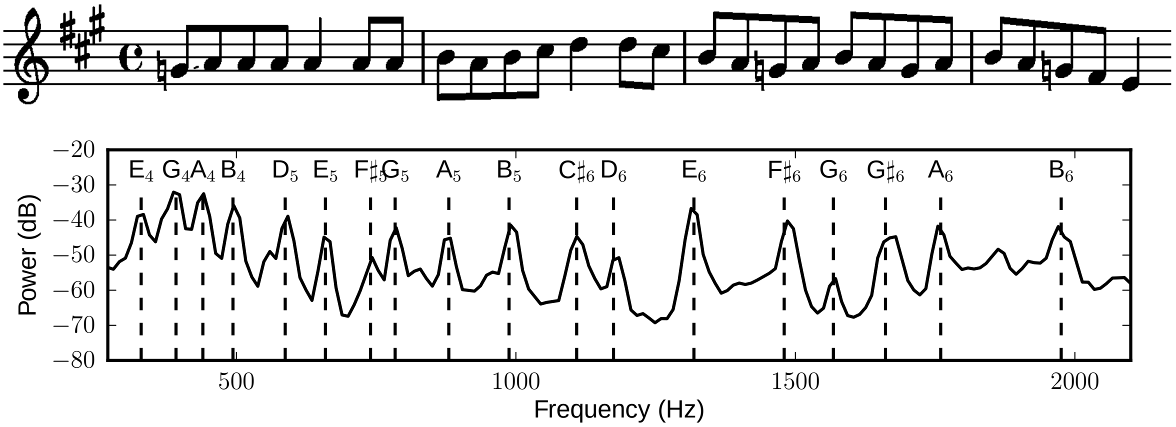

Figure 3.2: *Above:* Musical score of the opening phrase to "Salt Creek." *Below:* Time-compressed power spectrum of a recording of the phrase. The six-second recording was made by P. Boley on an Ibanez M510-OVS mandolin; dashed horizontal lines mark the frequencies of selected musical notes.

range, what key and musical mode the piece is in. With experience, we may be able to extend the analysis of the power spectra of musical compositions to tell us, for example, if the second A string of the mandolin was slightly out of tune (it was), was a plastic or metal plectrum used (plastic), and even what genre (bluegrass) and ethnic elements (Irish and American) the piece may contain.

However, due to the sparse frequency sampling (and particularly due to the lack of phase information), such an analysis will never tell us *what the piece actually sounds like!* Returning to the case of sparsely-sampled interferometric measurements of light from astronomical sources, we may be able to tell the size of something, whether it looks round, like a point source, like a disk, etc. But just as we cannot appreciate the richness of the musical composition from a few measurements of the power spectrum, we cannot reconstruct the full complexity of the image intensity distribution from a few measurements of the visibility amplitude.

3.3 The Very Large Telescope Interferometer

One of the premier facilities for performing optical long-baseline interferometric measurements is the Very Large Telescope (VLT) of the European Southern Observatory (ESO), located at 2600 m on Cerro Paranal, Chile. In total, the VLT consists of four stationary 8.2 m "Unit Telescopes" (UTs), each of which can be used independently, and an additional four movable 1.8 m "Auxiliary Telescopes" (ATs), which are used only in interferometric mode. When operating in interferometric mode, these instruments are known collectively as the Very Large Telescope Interferometer (VLTI).

In Fig. 3.3, I show a schematic of the entire VLTI layout, as viewed from above the mountain. The four large, fixed UT telescopes (indicated as U1–U4) are separated by distances ranging from 47 to 130 m. The smaller, movable AT telescopes can be installed at the interferometric stations, which are indicated by circles with the station names (A0, J6, M0, etc.). The distances between the different AT stations range from 8 to 200 m. In the schematic, there are AT telescopes installed at the G0 and I1 stations.

In order to perform interferometric observations of an astronomical target, it is necessary to observe the target simultaneously with multiple telescopes. Using a series of optical elements,

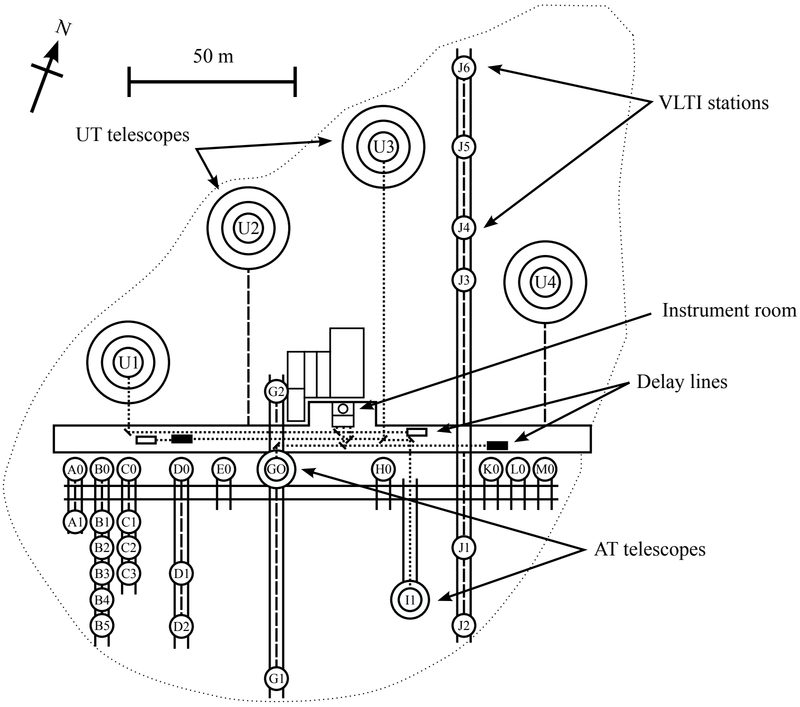

Figure 3.3: Layout of telescopes and interferometric stations of the VLTI. In the configuration shown, AT telescopes are operating at stations G0 and I1. The dotted line shows the optical path from these two 1.8 m telescopes, as well as two of the 8.2 m telescopes, UT1 and UT2. The signals from the telescopes are directed through the delay lines and to the instrument room, where they are coherently combined.

light is directed from the telescopes down through a series of underground delay lines, which serve to equalize the optical paths of the individual beams, so that they can be combined interferometrically in the instrument room (the “VLTI lab”). Here, light from up to four telescopes is fed to one of the interferometric instruments for coherent analysis, two of which are described below[3].

AMBER: Astronomical Multi-BEam combineR

Some of the interferometric data analyzed in this thesis (see Chapter 5) were measured using the VLTI instrument AMBER (Petrov et al., 2007). This is a three-telescope instrument operating at near-infrared wavelengths (1.0–2.4 μm), which simultaneously combines the light from three telescopes for spectrally-dispersed interferometric observations. The instrument can operate at resolutions of $R = \lambda/\Delta\lambda$ from ~ 35 up to $\sim 12\,000$, and measures the visibility amplitude for three baselines simultaneously, as well as the wavelength-dependent closure phase (i.e., the sum of the phases of the three baselines).

With the ability to measure three baselines simultaneously, as well as the closure phase, comes the possibility of obtaining sufficient uv coverage to perform limited image reconstruction,

---

[3] Presently, three instruments are located at the VLT on Paranal. Besides the official ESO instruments AMBER and MIDI, which are briefly described here, the four-telescope instrument PIONIER (Le Bouquin et al., 2011) is currently installed as a visitor instrument. The VINCI (Kervella et al., 2000) instrument was used during commissioning of the VLTI in 2001–2004. Future VLTI instruments are planned to include MATISSE (Lopez et al., 2008) and GRAVITY (Eisenhauer et al., 2011).

using specialized algorithms developed for this purpose (see, for example, the results of the 5th interferometric imaging "beauty contest", Baron et al., 2012). For example, a 2.2 μm image of IRAS 13481-6124, one of the objects covered in this thesis, was derived from AMBER measurements by Kraus et al. (2010).

MIDI: MID-infrared Interferometric instrument

The vast majority of the observations presented and analyzed in this thesis were measured at mid-infrared wavelengths (8–13 μm), using the two-telescope instrument MIDI (Leinert et al., 2003). MIDI can use either a prism or a grism as the dispersive element, offering a resolution R of ~ 30 or ~ 230, respectively. In contrast to AMBER, MIDI measures the correlated flux (the quantity in the numerator on the right-hand side of Eq. 3.1) directly, although the measurements are often normalized by the total (uncorrelated) flux and reported in terms of the visibility amplitude. Besides the correlated flux/visibility amplitude, MIDI also measures the so-called "differential phase," which is related to the derivative of the phase with respect to wavelength (see Sec 6.3).

The slow rate at which *uv* space can be covered with MIDI (typically 40-60 minutes is required to make a single calibrated visibility measurement), and the limited phase information available makes image reconstruction with MIDI extremely difficult, if not impossible. Nonetheless, MIDI represents the present state of the art of mid-infrared interferometric instruments, and is one of only two such instruments in the world[4].

---

[4] With the decommissioning of the Keck interferometer (e.g. Colavita et al., 2004) in 2012, the only other long-baseline mid-infrared interferometer is the UC Berkeley Infrared Spatial Interferometer Array (Hale et al., 2000).

References

Baron, F., Cotton, W. D., Lawson, P. R., et al.: 2012, The 2012 interferometric imaging beauty contest, in *Optical and Infrared Interferometry*, Vol. 8445 of *Society of Photo-Optical Instrumentation Engineers (SPIE) Conference Series*

Berger, J. P. and Segransan, D.: 2007, An introduction to visibility modeling. *New Astronomy Reviews* **51**, 576–582

Colavita, M. M., Wizinowich, P. L., and Akeson, R. L.: 2004, Keck Interferometer status and plans, in *New Frontiers in Stellar Interferometry*, W. A. Traub (ed.), Vol. 5491 of *Society of Photo-Optical Instrumentation Engineers (SPIE) Conference Series*, p. 454

Eisenhauer, F., Perrin, G., Brandner, W., et al.: 2011, GRAVITY: Observing the Universe in Motion. *The Messenger* **143**, 16–24

Fizeau, H.: 1868, Prix Bordin: Rapport sur le concours de l'année. *Comptes Rendus Hebdomadaires des Séances de l'Académie des Sciences* **66**, 932–934

Grimaldi, F. M.: 1665, *Physicomathesis de lumine, coloribus, et iride, aliisque annexis*, Vittorio Bonati, Bologna

Hale, D. D. S., Bester, M., Danchi, W. C., et al.: 2000, The Berkeley Infrared Spatial Interferometer: A Heterodyne Stellar Interferometer for the Mid-Infrared. *Astrophysical Journal* **537**, 998–1012

Haniff, C.: 2007a, An introduction to the theory of interferometry. *New Astronomy Reviews* **51**, 565–575

Haniff, C.: 2007b, Ground-based optical interferometry: A practical primer. *New Astronomy Reviews* **51**, 583–596

Hooke, R.: 1665, *Micrographia: or some physiological descriptions of minute bodies made by magnifying glasses*, Royal Society, London

Huygens, C.: 1690, *Traité de la lumière*, Pieter van der Aa, Leiden

Kervella, P., Coudé du Foresto, V., Glindemann, A., and Hofmann, R.: 2000, VINCI: the VLT Interferometer commissioning instrument, in *Interferometry in Optical Astronomy*, P. Léna and A. Quirrenbach (eds.), Vol. 4006 of *Society of Photo-Optical Instrumentation Engineers (SPIE) Conference Series*, pp 31–42

Kraus, S., Hofmann, K.-H., Menten, K. M., et al.: 2010, A hot compact dust disk around a massive young stellar object. *Nature* **466**, 339–342

Labeyrie, A., Lipson, S. G., and Nisenson, P.: 2006, *An Introduction to Optical Stellar Interferometry*, Cambridge University Press, Cambridge

Lawson, P. R. (ed.): 2000, *Principles of Long Baseline Stellar Interferometry*, Pasadena, Jet Propulsion Laboratory

Le Bouquin, J.-B., Berger, J.-P., Lazareff, B., et al.: 2011, PIONIER: a 4-telescope visitor instrument at VLTI. *Astronomy and Astrophysics* **535**, A67

Leinert, C., Graser, U., Przygodda, F., et al.: 2003, MIDI - the 10 \mum instrument on the VLTI. *Astrophysics and Space Science* **286**, 73–83

Lopez, B., Antonelli, P., Wolf, S., et al.: 2008, MATISSE: perspective of imaging in the mid-infrared at the VLTI, in *Optical and Infrared Interferometry*, M. Schöller, W. C. Danchi, and F. Delplancke (eds.), Vol. 7013 of *Society of Photo-Optical Instrumentation Engineers (SPIE) Conference Series*

Michelson, A. A. and Pease, F. G.: 1921, Measurement of the diameter of alpha Orionis with the interferometer.. *Astrophysical Journal* **53**, 249–259

Ohnaka, K., Hofmann, K.-H., Benisty, M., et al.: 2009, Spatially resolving the inhomogeneous structure of the dynamical atmosphere of Betelgeuse with VLTI/AMBER. *Astronomy and Astrophysics* **503**, 183–195

Petrov, R. G., Malbet, F., Weigelt, G., et al.: 2007, AMBER, the near-infrared spectro-interferometric three-telescope VLTI instrument. *Astronomy and Astrophysics* **464**, 1–12

Stéphan, E.: 1874, Sur l'extrême petitesse du diamètre apparent des étoiles fixes. *Comptes Rendus Hebdomadaires des Séances de l'Académie des Sciences* **78**, 1008–1012

Chapter 4

The VLTI/MIDI MYSO Survey*

In this chapter, I present the results of a survey to observe 20 MYSOs with the VLTI, using the mid-infrared interferometric instrument MIDI. This study aims to characterize the distribution and composition of circumstellar material around young massive stars, and to investigate exactly which physical structures are probed by long-baseline mid-infrared interferometric observations.

We fit the measured visibilities with geometric models to derive the emission scales, orientation and elongation of the circumstellar material, and, for a subset of the objects, fit the silicate feature seen in absorption in the correlated fluxes, allowing us to constrain the composition and absorptive properties of the circumstellar material.

Nearly all of the massive young stellar objects observed show significant asymmetries at mid-infrared wavelengths. In general, the mid-infrared emission can trace *both* disks and/or outflows, and in many cases it is not possible to disentagle these components with the *uv* coverage which can be provided by current long-baseline interferometers. For the majority of objects in this sample, the absorption is physically detached from the scales on which mid-infrared emission occurs, and in many cases the absorbing material shows signs of significant grain growth. Finally, the physical extent of the mid-infrared emission around these sources is correlated with the total luminosity, albeit with significant scatter.

4.1 Introduction

Circumstellar disks and outflows are essential components in, and natural byproducts of, the process of star formation, and commonly detected around low-mass T Tauri stars, and intermediate-mass Herbig Ae/Be stars. For “massive” ($\gtrsim 10\ \mathrm{M}_\odot$) stars, extended outflows have been detected around a number of massive young stellar objects (e.g. Mitchell et al., 1991; De Buizer et al., 2009). However, direct observations of material in circumstellar disks around MYSOs are complicated by the typically large distances ($\gtrsim$ 1 kpc) to these objects, as the required spatial resolution ($\lesssim 0\overset{\prime\prime}{.}1$) is difficult to achieve at infrared wavelengths, where thermal disk emission is expected to dominate.

Mid-infrared interferometry provides an important tool for achieving the high spatial resolution required to study the circumstellar material around young stars. The spatial scales probed by interferometric measurements are given roughly by $\lambda/2B$, where λ is the wavelength ($8 - 13\ \mu$m for the observations presented here), and B is the projected baseline between the telescopes forming the interferometer (up to 128 m for VLTI observations). For a fairly typical projected baseline of 50 m, this corresponds to angular scales of tens of milliarcseconds at a

---

[*] The material in this chapter is being prepared for publication in *Astronomy and Astrophysics* in early 2013, by P. Boley, H. Linz, R. van Boekel, T. Henning, M. Feldt, L. Kaper, C. Leinert, I. Pascucci, M. Robberto, B. Stecklum, R. Waters and H. Zinnecker.

wavelength of 10 μm, or to linear distances of tens of AU at typical distances to MYSOs (~ 1 to several kpc). Furthermore, due to the sharp cut-off of the Wien tail, material emitting thermally in the N band must have be warmer than roughly 200 K.

However, even with state-of-the-art facilities like the Very Large Telescope Interferometer (VLTI) on Cerro Paranal, performing interferometric observations is a time-consuming and challenging process. Consequently, obtaining sufficient uv coverage to perform true model-independent image reconstruction remains difficult at near-infrared wavelengths, and effectively impossible at mid-infrared wavelengths. Practically speaking, N-band observations are generally limited to a handful of visibility amplitude measurements, with no or extremely limited information about the phase of the complex visibility. Consequently, interpreting such measurements is challenging.

In the present work, we report the results of a campaign to observe intermediate- and high-mass YSO candidates with the two-telescope mid-infrared interferometric instrument MIDI (Leinert et al., 2003) on the VLTI. This survey was begun in 2004, and uses time within the guaranteed time for observations (GTO) program of the Max Planck Institute for Astronomy (MPIA). We present long-baseline ($\sim 10 - 130$ m), spatially-resolved observations for these sources. Where available, we combine these long-baseline observations with the aperture-masking measurements made with the Keck telescope and presented earlier by Monnier et al. (2009).

As a simple first analysis of this data, we examine the entire sample in terms of geometric models. This approach makes it possible to assess interferometric observations with sparse uv coverage, and extract fundamental parameters (size, orientation, elongation, brightness distribution) about the sources. For select sources, we fit the silicate absorption feature seen in the correlated flux spectra, which provides information about the composition and distribution of absorbing material.

4.2 Sample

The initial aim of our survey was to resolve MYSOs which are both bright at mid-infrared wavelengths, and were unresolved in previous imaging with 4-8 m-class telescopes. In particular, the first target selection focused largely on Becklin-Neugebauer (BN)-type objects (e.g Henning et al., 1990), including several massive disk candidates. Later, we extended the sample to include lower-luminosity sources, namely several early B-type stars with evidence for circumstellar disks (e.g. Herbig Be stars). Thus, the luminosities of the sample of 20 intermediate- to high-mass YSOs presented here range from $\sim 10^3$ to $\sim 10^5$ $L_\odot$.

In Table 4.1, we show the sources which make up the target sample. The coordinates shown are our best estimate of the infrared position, and were generally taken from the 2MASS point source catalog, when possible. The last four sources shown in Table 4.1 are objects for which fringes were not found, despite successful target acquisition by both telescopes; these objects are discussed in more detail in Sec. 4.4.3.

Where available, we have compiled values for distance and luminosity, as well as disk and/or outflow orientation, collected from the references listed. We emphasize that these properties range from being very well determined, to virtually unknown[1]. For disk orientation, we limit ourselves to near-infrared (generally interferometric and/or polarimetric) detections. For the

---

[1] For example, the distance to the Orion star-forming region, which hosts Orion BN, has been measured very precisely by Menten et al. (2007) using parallax measurements. At the same time, the distance to R Mon has never been measured, yet is generally quoted as being 800 pc, based on distance measurements to a star cluster which is *one full degree* away from the source on the sky. We regard such determinations as highly uncertain, but defer comments on specific sources to Sec. 4.5.4.

Table 4.1: Source properties

Source	RA (J2000) (h:m:s)	Dec (J2000) (d:m:s)	Distance (kpc)	$\log_{10} \frac{L}{L_\odot}$	Outflow PA (deg)	Disk PA (deg)
AFGL 2136	18:22:26.38	-13:30:12.0	2.0^{1}	5.0^{2}	135^{3}	46 ± 3^{4}
AFGL 4176	13:43:01.70	-62:08:51.2	5.3^{5}	5.5		
G305.20+0.21	13:11:10.45	-62:34:38.6	4.8 ± 1.7^{6}			
HIP 90617	18:29:25.69	-06:04:37.2	1.8 ± 0.20^{7}	5.1 ± 0.10^{7}		4 ± 3^{8}
IRAS 13481-6124	13:51:37.86	-61:39:07.5	3.6^{5}	4.5^{9}	26 ± 9^{9}	120^{9}
IRAS 17216-3801	17:25:06.51	-38:04:00.4	3.1 ± 0.60^{6}			
M17 SW IRS1	18:20:19.48	-16:13:29.8	2.1 ± 0.20^{10}	4.3^{11}		
M17 UC1	18:20:24.82	-16:11:34.9	2.1 ± 0.20^{10}			
M8E-IR	18:04:53.18	-24:26:41.4	1.2^{12}	3.8^{13}	324^{14}	
Mon R2 IRS2	06:07:45.80	-06:22:53.5	0.83 ± 0.050^{15}	3.8^{16}		162^{17}
Mon R2 IRS3 A	06:07:47.84	-06:22:56.2	0.83 ± 0.050^{15}	4.1^{16}		147^{17}
Mon R2 IRS3 B	06:07:47.86	-06:22:55.4	0.83 ± 0.050^{15}			
NGC 2264 IRS1	06:41:10.16	+09:29:33.7	0.91 ± 0.11^{18}	3.6^{19}	353^{20}	
Orion BN	05:35:14.10	-05:22:22.9	0.41 ± 0.0070^{21}	4.1 ± 0.21^{22}		36^{23}
R CrA	19:01:53.65	-36:57:07.6	0.14 ± 0.016^{24}			185 ± 5^{25}
R Mon	06:39:09.95	+08:44:10.7	0.80^{26}	3.1^{26}	350^{27}	
S255 IRS3	06:12:54.02	+17:59:23.6	1.6 ± 0.070^{28}	4.7^{29}	63^{30}	
V1028 Cen	13:01:17.80	-48:53:18.8	1.7 ± 0.23^{31}	3.2 ± 0.080^{31}		
V921 Sco	16:59:06.78	-42:42:08.3	1.1 ± 0.15^{32}	4.0 ± 0.15^{32}		145 ± 1.3^{33}
VY Mon	06:31:06.92	+10:26:04.9	0.90 ± 0.20^{34}	3.1^{35}		
Sources without fringe detections:						
GGD27 ILL	18:19:12.08	-20:47:30.9				
Herschel 36 SE	18:03:40.22	-24:22:43.2				
IRAS 17136-3617	17:17:02.29	-36:21:08.2				
Orion SC3	05:35:16.34	-05:23:22.6				

References. (1) Kastner et al. (1992); (2) de Wit et al. (2011); (3) Kastner et al. (1994); (4) Minchin et al. (1991); (5) Fontani et al. (2005); (6) This work; (7) Miroshnichenko et al. (2004); (8) Wang et al. (2012); (9) Kraus et al. (2010); (10) Hoffmeister et al. (2008); (11) Follert et al. (2010); (12) Prisinzano et al. (2005); (13) Linz et al. (2009); (14) Mitchell et al. (1991); (15) Herbst and Racine (1976); (16) Henning et al. (1992); (17) Yao et al. (1997); (18) Baxter et al. (2009); (19) Grellmann et al. (2011); (20) Schreyer et al. (2003); (21) Menten et al. (2007); (22) De Buizer et al. (2012); (23) Jiang et al. (2005); (24) Ortiz et al. (2010); (25) Kraus et al. (2009); (26) Cohen et al. (1984); (27) Brugel et al. (1984); (28) Rygl et al. (2010); (29) Longmore et al. (2006); (30) Tamura et al. (1991); (31) Verhoeff et al. (2012); (32) Borges Fernandes et al. (2007); (33) Kraus et al. (2012); (34) Casey and Harper (1990); (35) Henning et al. (1998).

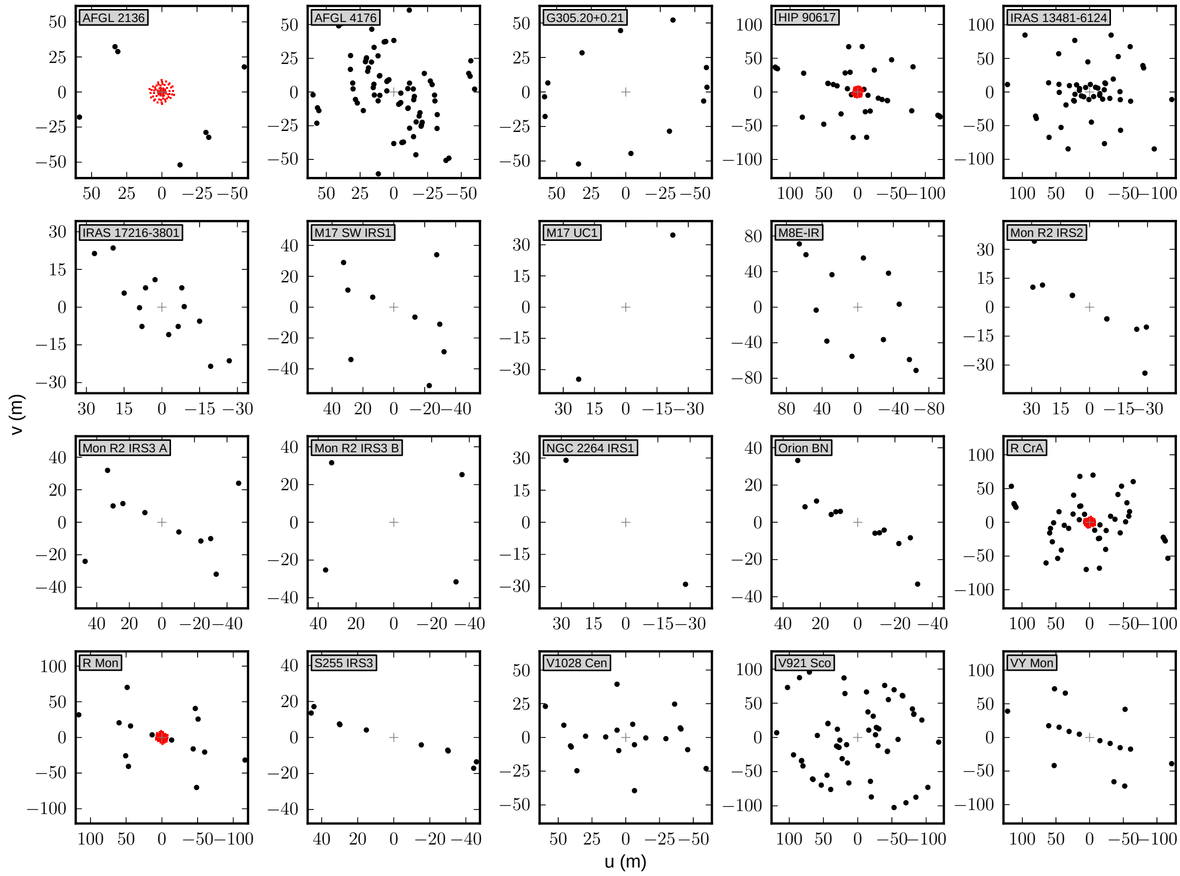

Figure 4.1: The *uv* coverage for each source. The observations from MIDI are shown in black, while the Keck data from Monnier et al. (2009) are shown in red (only available for select sources).

outflow orientation, we use a variety of signatures and wavelengths, ranging from optical detections of Herbig-Haro objects to radio maps of dense gas.

For two sources where a distance estimate was not available, we used the rotation curve of Reid et al. (2009) together with radial velocity measurements from molecular line data. Specifically, for G305.20+0.21, Hindson et al. (2010) found $V_{\mathrm{LSR}} = -42.0$ km s^{-1} from observations of the NH$_3$(3,3) line at 24 GHz, which corresponds to a kinematic distance of 4.8 ± 1.7 kpc, with no near/far distance ambiguity. For IRAS 17216-3801, however, no thermal molecular line data have been published to date. Several studies list OH maser detections (e.g. Cohen et al., 1995; Argon et al., 2000), but the measured V_{LSR} velocities cover a range from -18 to -24 km s^{-1}. We therefore adopt a velocity of -22.0 km s^{-1}, based on recently-conducted APEX measurements in the H^{13}CO^{+}(4–3) line (Linz et al., in preparation). This corresponds to a near distance of 3.1 ± 0.6 kpc, which we adopt in this work, and a far distance of 13 ± 0.6 kpc.

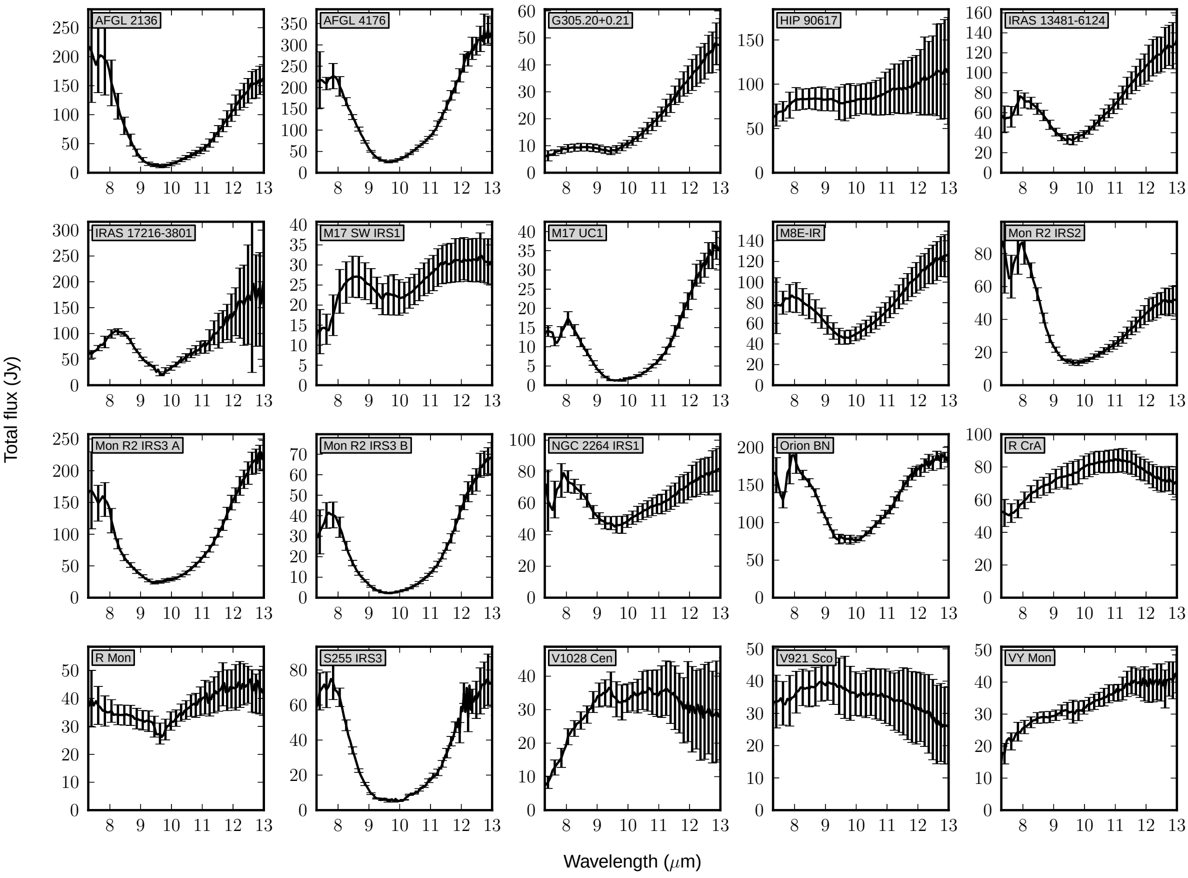

Figure 4.2: Total N-band spectra of the sources.

4.3 Observations and data reduction

4.3.1 Long-baseline interferometry with VLTI

Observations with the MIDI instrument at the VLTI facility of the European Southern Observatory (ESO) on Cerro Paranal were performed in the period 2004 – 2012, using both the 8.2 m Unit Telescopes (UTs) and the 1.8 m Auxiliary Telescopes (ATs). MIDI, operating at the VLTI continuously since 2003, is a two-telescope interferometric instrument, which measures correlated flux, spectrally dispersed over the *N* band ($\sim 8 - 13\ \mu$m). The nominal observation procedure with MIDI has already been described by Leinert et al. (2004), and we refer to that publication for a more detailed discussion.

We summarize the observations in Table 4.4, where we show the time of the fringe track, the telescopes/stations used, as well as the projected baseline and position angle. For four of the targets, despite good weather conditions and no apparent technical problems, we did not detect fringes; these non-detections are summarized at the end of Table 4.4. All data presented here used the prism ($\lambda/\Delta\lambda \approx 35$), and were carried out in the HIGHSENS mode, meaning the correlated flux and photometric measurements are made separately. The *uv* coverage for the 20 targets is shown in Fig. 4.1, where black points indicate the MIDI measurements. Besides the observations conducted within the framework of the present survey, we also include data previously published by other investigators: one *uv* point for AFGL 2136 (de Wit et al., 2011), and 12 points for R CrA (Correia et al., 2008).

We reduced the raw MIDI data using version 2.0Beta1 (8 Nov. 2011) of the MIA+EWS package. This new version of MIA+EWS includes significant improvements for sources with low correlated flux. In particular, we make use of the `faintpipe` procedures to create masks from the interference fringe pattern of all the calibrators. For each night and baseline configuration, we create a median mask from the individual calibrator masks, which we use for extracting the correlated flux and total spectra from the science measurements.

For each target, we created a median spectrum of the total *N*-band flux from the individual photometric measurements with MIDI. For sources which were measured with both the UTs and ATs, we used only the spectra observed with the UTs.

4.3.2 Aperture-masking interferometry with Keck-1

For four of the sources in our sample, we also make use of previously-published aperture-masking interferometric observations with the Keck-1 telescope, as part of the segment-tilting experiment by Monnier et al. (2009). These visibility measurements are not spectrally resolved, but rather were taken with a 10.6 μm filter (transmission curve shown in Fig. 4.3). The *uv* coverage provided is uniform, with projected baselines of 0.5–9 m. We show the location of these measurements in *uv* space as red points in Fig. 4.1.

4.4 Results

4.4.1 Geometric fits to wavelength-averaged visibilities

The MIDI instrument provides spectrally-dispersed interferometric visibilities over the entire *N*-band, at projected baselines which range from about 5 to 130 m for the observations presented here. However, in order to both simplify the analysis, and homogenize the union of the VLTI and Keck observations (available for five of the 20 sources presented here), we first examine the complete data set at a single wavelength of 10.6 μm, which corresponds to the center of the filter used for the Keck observations (Fig. 4.3). By multiplying the MIDI visibilities by

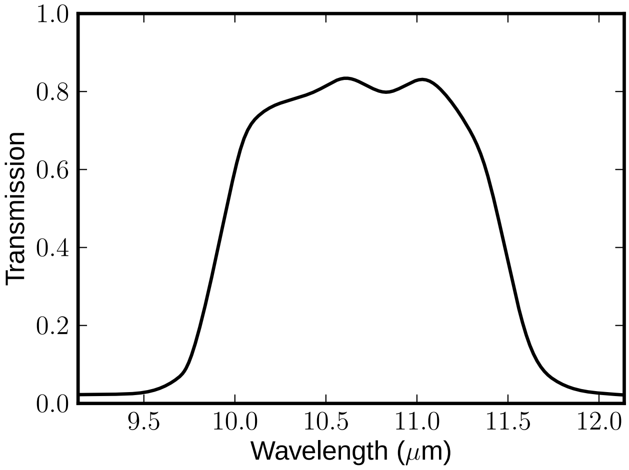

Figure 4.3: Transmission curve of the Keck 10.6 μm filter.

the transmission curve of the Keck filter, we thus derive an average visibility level in the filter, allowing us to directly compare the VLTI and Keck data.

Uniform *uv*-coverage remains difficult to achieve with long-baseline mid-infrared interferometric observations. In Fig. 4.1, it can be seen that the coverage ranges anywhere from a single *uv* point (e.g. M17 UC1) up to several dozen (e.g. IRAS 13481-6124). For some objects, radial coverage is quite good, while measurements at multiple position angles are lacking (e.g. S255 IRS3). For other objects (e.g. M8E-IR), position angles are well sampled, but radial coverage is deficient.

To deal with this variety of *uv* coverage, we fit up to a maximum of four geometric models to the visibility levels at 10.6 μm, depending on the distribution of observations in *uv* space. In order of increasing complexity, these models are: a one-dimensional Gaussian (denoted “1D”); a one-dimensional Gaussian plus an overresolved component (“1DOR”); a two-dimensional Gaussian plus an overresolved component (“2DOR”); and a two-dimensional Gaussian plus a one-dimensional Gaussian (“2D1D”). For the two-dimensional models, we constrain the two components to be centered, meaning all the models are point symmetric.

We show the best-fit parameters for each of these models in Table 4.5. The uncertainties on the fitting parameters are derived using a Monte-Carlo approach, where we generate synthetic observations, normally-distributed about the mean observed visibility level with a standard deviation equal the measurement uncertainty, and repeat the optimization process. In Fig. 4.4, we show the observed 10.6 μm visibility levels for each source, together with each best-fit model. The image intensity distributions of the best-fit models are shown in Fig. 4.5 (angular scale) and Fig. 4.6 (linear scale).

4.4.2 Characterization of the spectrally-dispersed correlated flux levels

Besides the wavelength-averaged visibility levels, the MIDI measurements can also be considered in terms of their spectral behavior. Here, rather than the visibility amplitude (i.e., the ratio of the correlated flux to the total flux), we focus on the correlated flux measured in each observation.

We show the correlated flux as a function of wavelength for each point in *uv* space for one source, Orion BN, in Fig. 4.7. The remaining objects are presented in Figs. 4.11–4.29 of the online version of the journal. In general, we note that sources which show silicate absorption in

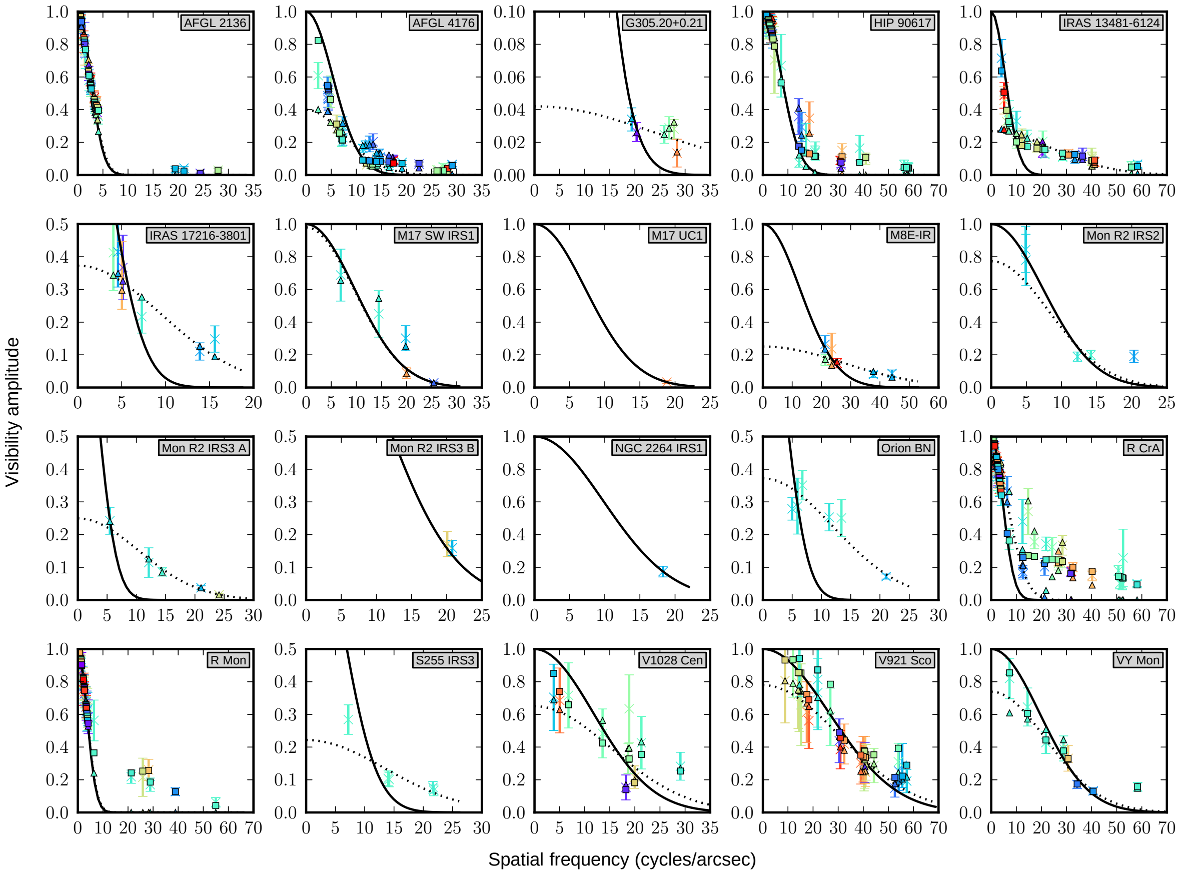

Figure 4.4: Best-fit geometric models to the 10.6 μm visibilities. The observations are shown as crosses with error bars. The 1D model is shown as a solid line, and the 1DOR model is shown as a dotted line. The triangles show the 2DOR model, while the squares show the 2D1D model. For a description of the different models, see Sec. 4.4.1.

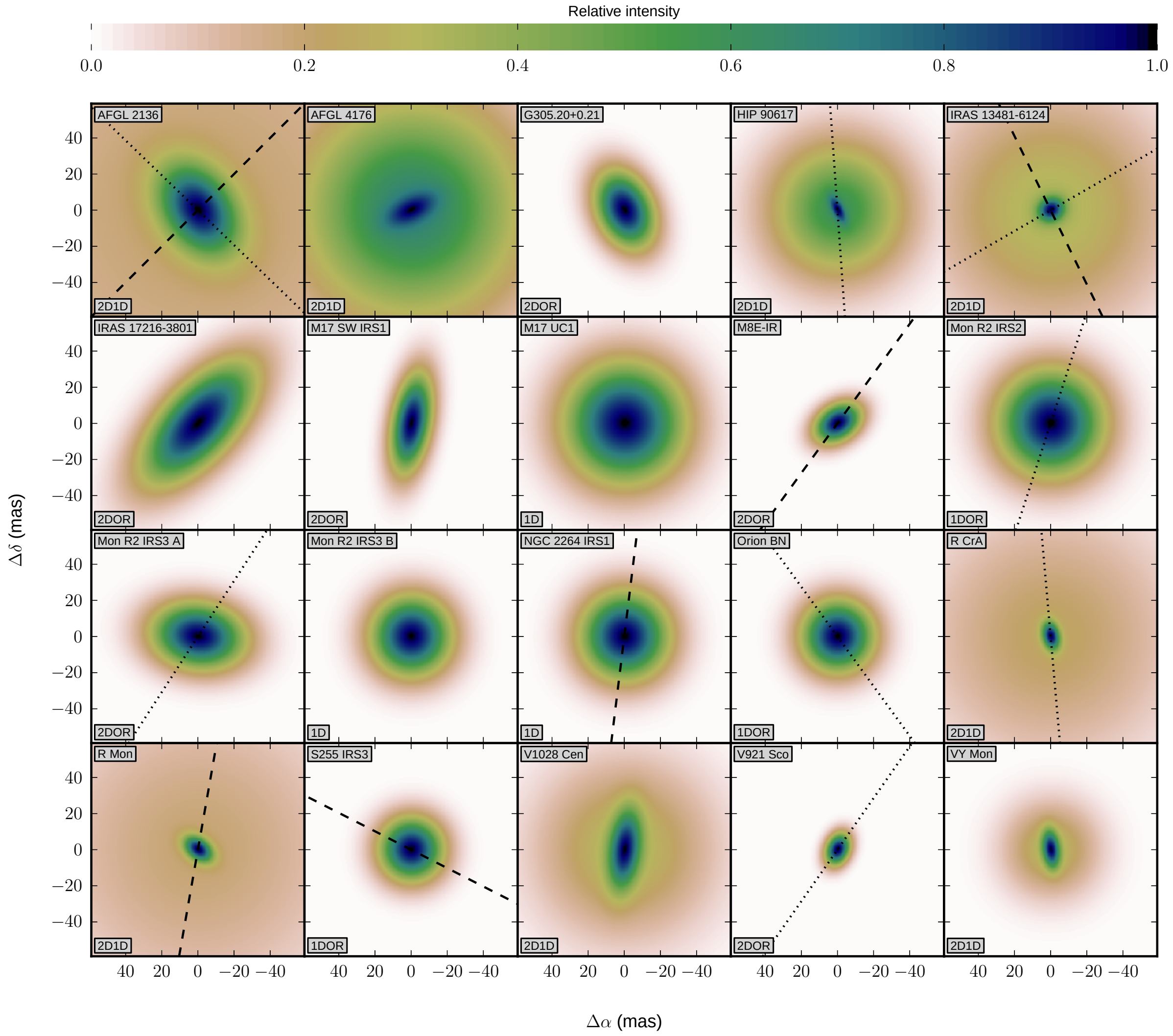

Figure 4.5: The intensity distributions of the best-fit models described in Sec. 4.4.1. The model parameters are shown in Table 4.5. Where available, we have indicated outflow and/or disk orientations as dashed and dotted lines, respectively (see Table 4.1 for disk/outflow directions and references).

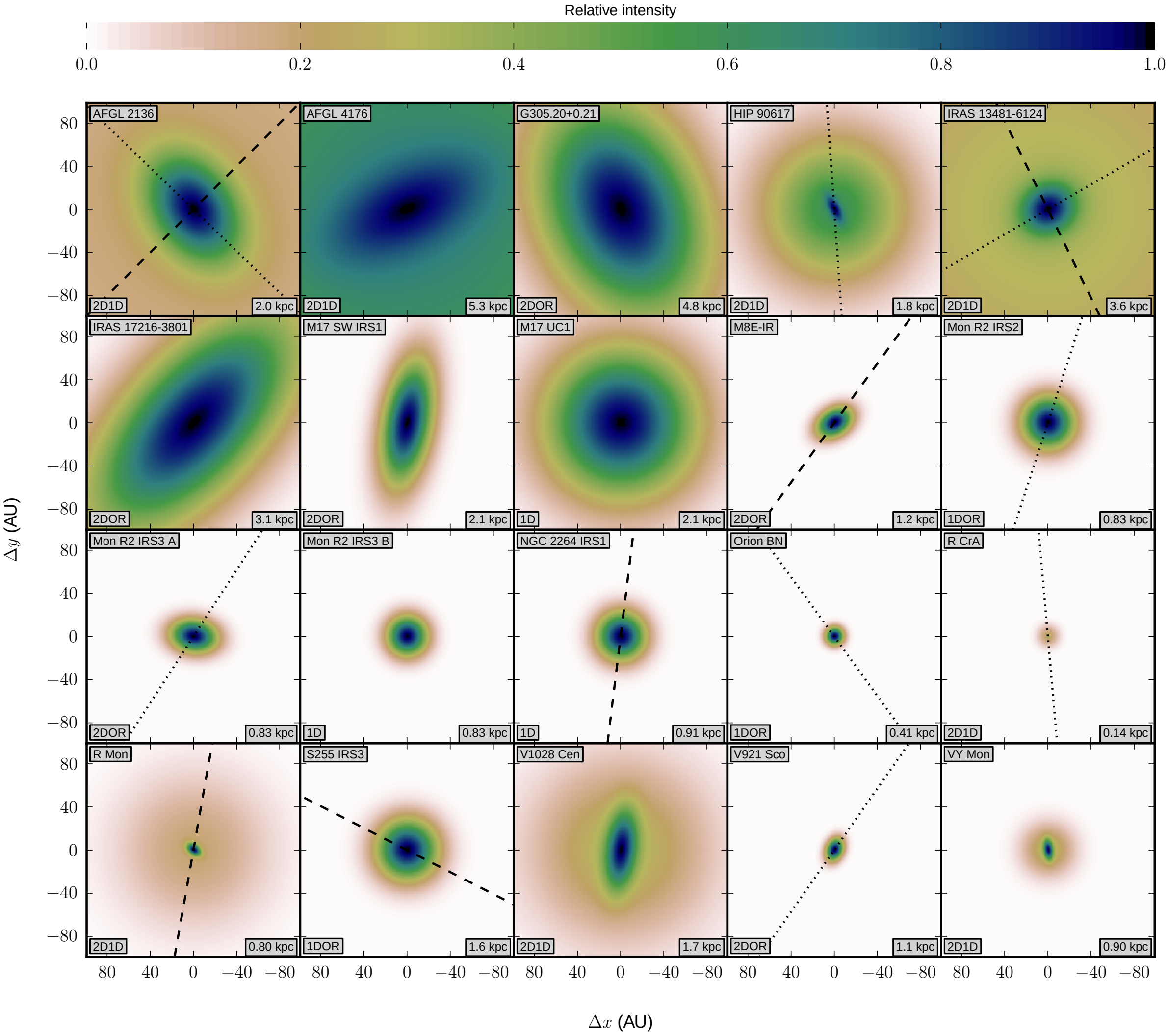

Figure 4.6: Same as Fig. 4.5, but the images have been scaled to linear distances in AU using the distances from Table 4.1.

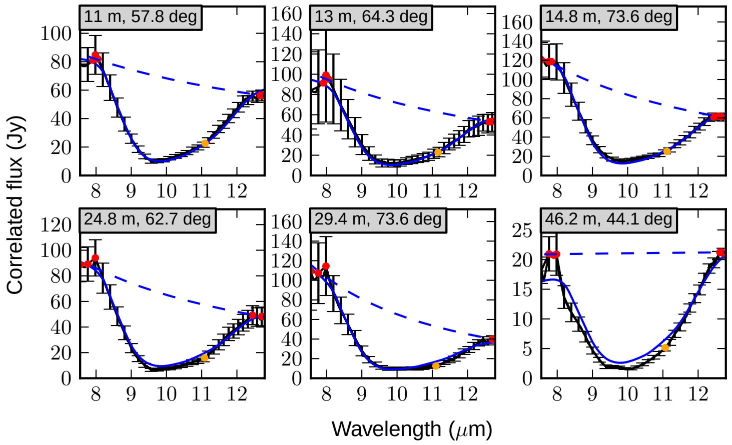

Figure 4.7: Measured correlated flux levels (solid black line and error bars) for Orion BN, in order of increasing projected baseline. The caption shows the projected baseline and position angle of the observation, as well as the slope p of the continuum fit (dashed blue line) to the red points. The solid blue line shows the best fit to the absorption spectrum (see Sec. 4.4.2).

their total N-band spectra (Fig. 4.2) also show absorption in the correlated flux. Qualitatively, this is to be expected, as foreground material (which may include an extended envelope, in addition to the diffuse ISM) will indiscriminately absorb both total and correlated flux. However, departures from this may be observed if the absorption occurs on scales resolved by MIDI. Additionally, the contribution of emission to the total and (spatially-filtered) correlated flux levels can, in general, depend on both the spatial distribution and spectral characteristics of the emitting material.

In order to evaluate the depth of the silicate feature in each individual spectrum, we fit a continuum in the form of a power law, shown as a blue line in Figs. 4.7 and 4.11–4.29, to the correlated flux in the ranges 7.5–8.2 μm and 12.4–12.8 μm (shown as red points in the figures). We evaluate the optical depth of the silicate feature as $\tau_\nu(\lambda) = \ln\left(F_\nu(\lambda)/F_\nu^{(c)}(\lambda)\right)$, where F_ν is the measured correlated flux, and $F_\nu^{(c)}$ is the continuum fit. In Table 4.2, for the sources which show silicate absorption, we show the derived optical depth at a wavelength of 10.2 μm[2], where we have taken the mean value and standard deviation of each target over all the observed baselines and position angles.

Fitting the correlated flux absorption spectra

A common approach used to model mid-infrared spectra, much simpler than full radiative transfer modeling, is to fit the observed spectrum with a blackbody or power-law spectrum, modified by experimental and/or laboratory dust opacities. For spectra which show little or no absorption, this approach has been used to analyze the composition of material around T Tauri stars (e.g Olofsson et al., 2010) and Herbig Ae/Be stars (e.g. Juhász et al., 2010).

Here, we apply a similar approach to the *absorption* spectra of 13 of the objects in our sample, which have spectra dominated by silicate absorption[3]. In our model, we let the correlated flux

---

[2] Although the central wavelength of the silicate feature is nominally ~ 9.7 μm, the 9.3–10.1 μm region of the N-band is affected by ozone absorption.

[3] We exclude Mon R2 IRS3A from this analysis, which has a much wider absorption feature than can be fit by pyroxne and olivine (see Fig. 4.21).

Table 4.2: Optical depth of the silicate absorption feature in the correlated flux, averaged over all measurements.

Source	$< \tau_\nu(10.2\ \mu\mathrm{m}) >$	σ_{τ_ν}
AFGL 2136	2.33	0.195
AFGL 4176	1.82	0.287
G305.20+0.21	1.71	0.763
IRAS 13481-6124	1.28	0.139
IRAS 17216-3801	0.962	0.201
M17 UC1	1.81	—
M8E-IR	0.738	0.0922
Mon R2 IRS2	1.27	0.0509
Mon R2 IRS3 A	2.65	0.169
Mon R2 IRS3 B	2.69	0.0626
NGC 2264 IRS1	0.347	—
Orion BN	1.88	0.311
R Mon	0.919	0.255
S255 IRS3	2.25	0.321

F_ν be described by a power-law continuum extincted by foreground material, i.e.

$$F_\nu(\lambda) = C\lambda^p e^{-\tau_\nu(\lambda)}, \tag{4.1}$$

where the absorption optical depth $\tau_\nu(\lambda)$ is 1) given by the product of the column density and extinction cross-section (defined by the dust composition) of the absorbing material, and 2) defined to be the same for all baselines/position angles. In this context, this "foreground" absorbing material then includes components from both the source envelope, in addition to the diffuse ISM along the line of sight. and diffuse ISM, with the former most likely being the dominant contributor.

For the dust components, we limit ourselves to two sizes each (0.1 and 1.5 μm) of spherical grains of amorphous material, in the form of olivine ($\mathrm{Mg}_{2x}\mathrm{Fe}_{2-2x}\mathrm{SiO}_4$) and pyroxene ($\mathrm{Mg}_x\mathrm{Fe}_{1-x}\mathrm{SiO}_3$) glasses. We find that the pure $\mathrm{Mg}_2\mathrm{SiO}_4$/$\mathrm{MgSiO}_3$ grains presented by Jäger et al. (2003) are unable to reproduce the observed absorption spectra, and that at least some amount of iron is required; we therefore adopt a fixed Mg/Fe ratio and take the optical properties of the grains from Dorschner et al. (1995) for $x = 0.5$ (equal Mg/Fe content). We calculate mass absorption coefficients for each grain type and size, shown in Fig. 4.8, using Mie scattering theory.

This simplified model makes two important assumptions about the correlated flux spectra which may not hold in all cases. Namely, that the underlying emission is well-described by a power law, and that the foreground absorbing screen, which implicitly includes contributions from both an envelope and the diffuse ISM, is independent of spatial scale. Deviations from a power law for the emission can occur not only in the form of spectral features in the emitting material, but can also arise from signatures of the spatial structure in the correlated flux (e.g. from a binary signal or zero crossings in the visibility amplitude). That the foreground absorbing screen is independent of spatial scale means that this absorbing material is essentially uniform on the spatial scales probed by the observations. This may not be true, for example, if significant absorption is occurring at scales already resolved by MIDI. These two assumptions are difficult to verify *a priori*, but for now we merely take them as postulates, and discuss their validity for individual sources in Sec. 4.5.4.

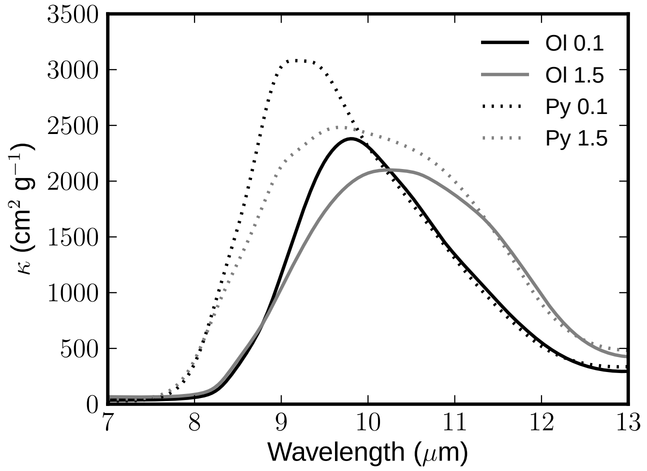

Figure 4.8: Mass absorption coefficients for amorphous $MgFeSiO_4$ (solid lines) and amorphous $Mg_{0.5}Fe_{0.5}SiO_3$ (dotted lines). Black lines are for a grain radius of 0.1 μm, and the gray lines are for a grain radius of 1.5 μm.

Table 4.3: Derived column densities and relative contributions (by mass) of absorbing material.

		$MgFeSiO_4$		$Mg_{0.5}Fe_{0.5}SiO_3$	
Source	Mass col. density (10^{-4} g cm^{-2})	$r = 0.1$ μm (%)	$r = 1.5$ μm (%)	$r = 0.1$ μm (%)	$r = 1.5$ μm (%)
AFGL 2136	$12.7^{+0.78}_{-1.1}$	$2.5^{+30.2}_{-2.3}$	$2.1^{+22.1}_{-2.0}$	$75.5^{+13.8}_{-39.8}$	$19.9^{+50.3}_{-10.0}$
G305.20+0.21	$7.75^{+0.37}_{-0.37}$	$63.9^{+24.1}_{-30.6}$	$2.9^{+34.0}_{-2.6}$	$29.9^{+19.1}_{-13.2}$	$3.3^{+44.9}_{-3.0}$
IRAS 17216-3801	$4.67^{+0.080}_{-0.074}$	$79.9^{+5.5}_{-10.4}$	$0.8^{+7.5}_{-0.8}$	$18.9^{+8.8}_{-2.6}$	$0.3^{+3.8}_{-0.3}$
M17 UC1	$8.77^{+0.49}_{-0.35}$	$89.6^{+34.2}_{-26.1}$	$3.5^{+43.9}_{-3.2}$	$2.5^{+30.7}_{-2.3}$	$4.4^{+61.5}_{-4.2}$
M8E-IR	$3.68^{+0.034}_{-0.048}$	$70.6^{+5.0}_{-9.5}$	$28.2^{+8.9}_{-3.9}$	$0.3^{+3.6}_{-0.3}$	$0.9^{+6.9}_{-0.8}$
Mon R2 IRS2	$6.64^{+0.077}_{-0.14}$	$75.9^{+3.0}_{-22.9}$	$1.5^{+17.9}_{-1.3}$	$21.6^{+4.4}_{-3.1}$	$0.9^{+6.9}_{-0.9}$
Mon R2 IRS3 B	$12.9^{+1.9}_{-0.58}$	$53.0^{+31.1}_{-31.3}$	$2.6^{+39.6}_{-2.5}$	$41.9^{+5.2}_{-24.4}$	$2.5^{+36.7}_{-2.5}$
NGC 2264 IRS1	$1.68^{+0.27}_{-0.055}$	$42.9^{+28.0}_{-25.2}$	$2.8^{+41.4}_{-2.7}$	$51.8^{+17.7}_{-20.8}$	$2.4^{+20.0}_{-2.3}$
Orion BN	$9.19^{+0.032}_{-0.13}$	$64.9^{+5.2}_{-11.3}$	$27.3^{+7.3}_{-9.1}$	$7.0^{+1.6}_{-3.5}$	$0.8^{+9.1}_{-0.8}$
R Mon	$3.22^{+0.067}_{-0.065}$	$78.2^{+6.6}_{-19.2}$	$2.1^{+18.6}_{-2.0}$	$17.7^{+8.0}_{-7.0}$	$2.1^{+16.0}_{-1.9}$
S255 IRS3	$11.7^{+0.23}_{-0.52}$	$30.4^{+11.6}_{-11.6}$	$26.2^{+9.3}_{-13.9}$	$23.9^{+7.0}_{-10.5}$	$19.6^{+18.0}_{-10.2}$

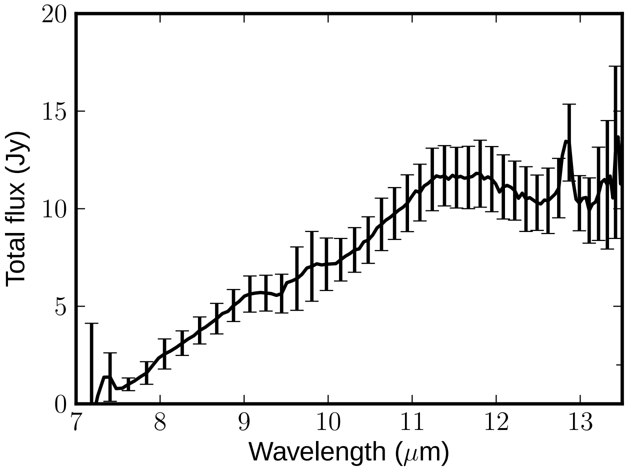

Figure 4.9: Total spectrum of GM24 measured with the 8.2 m UT telescopes on 2006-05-18. The error bars represent the uncertainty in the absolute flux calibration.

In total, for a source n correlated flux measurements, there are $2n + 4$ free parameters in this model ($2n$ parameters for the power-law continua, and 4 parameters describing the column densities of each dust type/size). We use a downhill-simplex χ^2-minimization routine to optimize all these parameters simultaneously. For an initial solution, we fit a continuum as described in Sec. 4.4.2, take an equal mix of the four grain types/sizes, and let the total optical depth at 10.2 μm be equal to unity. We derive uncertainties on the fit parameters using a Monte-Carlo approach, where we generate synthetic correlated flux values, normally spread about the observed values, with a standard deviation equal to the noise (i.e., random) error on the measurement as derived by EWS[4] and repeat the fit procedure 100 times; the optimum model parameters and their uncertainties are given by the mean and standard deviation, respectively, of the parameters in this ensemble. We show the best-fit models using this procedure as a solid blue line in Figs. 4.7 and 4.11–4.29, and list the total column densities of the absorbing material and the relative mass fraction of each dust component in Table 4.3.

4.4.3 Non-detections

We attempted to observe GM 24 two times with MIDI, using projected baselines of 25 and 46 m. However, despite successful acquisition and good weather conditions, no fringes were found, indicating the source is completely overresolved at these baselines. We show a spectrum of the total flux, measured with the 8.2 m UT telescopes, in Fig. 4.9. We note the distinct absence of any silicate absorption feature, despite the apparently large visual extinction of the near-infrared source IRS 3A ($A_V \gtrsim 50$ mag; Tapia et al., 2009), with which the mid-infrared source is probably associated. This source also represents the only detection of the [Ne II] nebular emission line at 12.8 μm in our sample.

---

[4] Note that the error bars shown in Figs. 4.7 and 4.11–4.29 represent the combination of this random error, plus the uncertainty on the absolute calibration. The random error, which characterizes the wavelength-to-wavelength scatter in the correlated flux of an individual spectrum, is about an order of magnitude smaller than the calibration error.

4.5 Analysis and discussion

4.5.1 *N*-band geometry

The results of the geometric modeling described in Sec. 4.4.1 show a range of linear sizes and inclinations. In general, the mid-infrared intensity distributions of the sources are asymmetric: when our *uv* coverage is sufficient to fit a two dimensional model, we find inclinations ranging from 30° to 80° (corresponding to axial ratios of about 1.15 to 6), indicating the presence of non-spherical structures on scales of tens of milliarcseconds.

For ten of the targets observed in our sample, independent information about disks and/or outflows is available in the literature, which can provide insights into the physical nature of the asymmetries present in the MIDI data. In Figs. 4.5 and 4.6, we show, where available, orientations collected from the literature (see Table 4.1 for values and references) for circumstellar disks (dotted lines) and/or outflows (dashed lines).

In general, we see a tendency for the compact, mid-infrared emission to trace disk structures, albeit with exceptions. As extreme cases, the compact, mid-infrared emission of AFGL 2136 is both elongated along the direction of the circumstellar disk and perpendicular to the outflow, while the situation in the case of M8E-IR seems to be opposite: the MIDI visibilities seem to trace an outflow component (no disk detection for this object has been reported in the literature). For five sources with known disks and/or outflow components, and where we fit a two-dimensional geometric model (HIP 90617, IRAS 13481-6124, R CrA, R Mon and V921 Sco), there seems to be a trend for alignment parallel to the disk/perpendicular to the outflow. In the case of Mon R2 IRS3A, the mid-infrared emission is roughly perpendicular to the polarization disk reported by Yao et al. (1997).

4.5.2 Mid-IR size vs luminosity

At near-infrared wavelengths, using a model consisting of a thin ring representing the inner radius of a circumstellar disk, Monnier and Millan-Gabet (2002) showed a tight correlation between luminosity and ring radius for YSOs with luminosities in the range $\sim 10^0$–10^5 $\mathrm{L}_\odot$. This correlation arises both because the dust sublimation radius varies with $\sqrt{L_*}$ (e.g. Monnier and Millan-Gabet, 2002), and because the near-infrared emission from grains near the dust evaporation temperature (~ 1500 K) is confined to a small region of the disk. This relation seems to break down at higher luminosities ($L \gtrsim 10^4$ $\mathrm{L}_\odot$), which may indicate the presence of optically-thick circumstellar gas interior to the dust evaporation radius (Monnier et al., 2005).

The relation between size and luminosity has been examined at mid-infrared wavelengths, as well. Using the FWHM of a Gaussian fit to the mid-infrared visibilities, Monnier et al. (2009) and Grellmann et al. (2011) found that although the mid-infrared size of YSOs is correlated with luminosity, there is considerably more scatter in the relation than is seen at near-infrared wavelengths. Indeed, this is to be expected; as noted in both these works, at mid-infrared wavelengths the notion of "size" becomes more complex than a simple ring radius: the mid-infrared intensity distribution is complicated by a combination of geometrical effects (e.g. flaring, shadowing), temperature/wavelength effects (the extent of the near-infrared emission is limited by the Wien cut-off at the dust sublimation temperature) and the fact that the mid-infrared radiation is expected to arise from a variety of structures (e.g. disk wall, disk surface, envelope).

We show the FWHM size we derive from the one-dimensional Gaussian geometric model vs luminosity as black crosses in Fig. 4.10, together with the sizes and luminosities compiled by Grellmann et al. (2011) as gray crosses. In our own sample, in order to restrict ourselves to sources where we do not completely overresolve the extended structure with the interferometer, we limit the selection to those sources for which we measure $V \gtrsim 0.5$ at the shortest baselines.

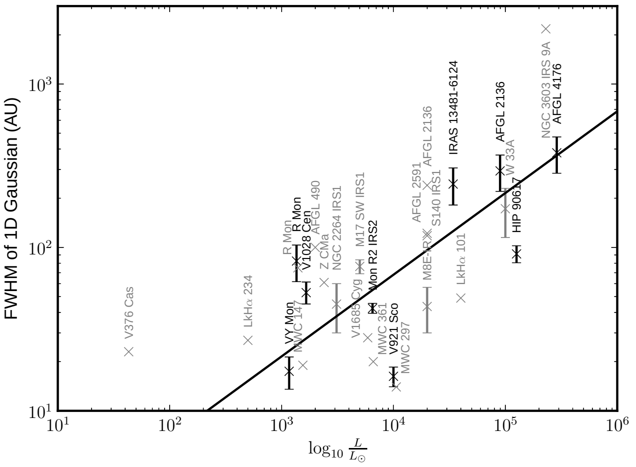

Figure 4.10: Linear size vs luminosity. The black crosses show the sizes derived in this work from the one-dimensional Gaussian models for selected sources (see Sec. 4.5.2), while the gray crosses show the results compiled by Grellmann et al. (2011). The solid line shows a fit to the black points for FWHM $\propto \sqrt{L}$.

Besides the uncertainty on the derived angular size, in the derivation of the linear size we also account for the uncertainty in the distance to each source, which we estimate to be 25% if no value is available in Table 4.1. As both Monnier et al. (2009) and Grellmann et al. (2011) found, we see considerable scatter in the mid-IR size vs luminosity relation. A scaling relation of FWHM $\propto \sqrt{L}$, shown as a black line in Fig. 4.10, is *consistent* with the mid-infrared sizes, but is by no means as well-defined as at near-infrared wavelengths.

4.5.3 Absorption spectra

In general, we find that the power-law emission/foreground absorption model described in Sec. 4.4.2 for the 13 sources in Table 4.3 adequately reproduces the observed correlated flux spectra in almost all cases (the fits for the sources from Table 4.3 are shown as blue lines in Figs. 4.7 and 4.11–4.29). As the column density and composition of the absorbing material is constrained to be the same for all baselines, this means that the absorption (due to silicates) is both uniform over the spatial scales probed by MIDI, and physically detached from those scales. Furthermore, the underlying emission also seems to be well-approximated by a power law.

There are, however, some cases where this simple model is unable to reproduce the observed correlated flux levels. For example, in AFGL 4176 (Fig. 4.12) the fits at short baselines are quite good, and become progressively worse at long baselines. At the longest spatial scales, the imprint of the spatial structure on the correlated flux levels becomes apparent (Boley et al., 2012), meaning the assumption of the underlying emission having a power-law spectrum is incorrect. Such spatial effects may also be present in G305.20+0.21 (Fig. 4.13) and Mon R2 IRS3A (Fig. 4.21).

Besides effects from the source geometry, the true spectrum behind the foreground absorption screen may, in the general case, contain spectral features (from, for example, silicates, crystalline grain species, etc.). Such features may become more prominent at longer baselines due to the emission arising from a circumstellar disk (e.g van Boekel et al., 2004). However, accounting for emission features in the spectra of deeply-embedded sources is a complicated process, and beyond the scope of the present work.

4.5.4 Notes on selected sources

AFGL 2136

AFGL 2136 IRS 1 is from the classic list of BN–type objects (Henning et al., 1984). It is the illuminating IR source of the so-called Juggler reflection nebula (Kastner et al., 1992). Menten and van der Tak (2004) found faint centimeter emission (their component RS4) closely associated with AFGL 2136. The nature of this emission, which is optically thick up to frequencies of $\sim$ 43 GHz, is not clarified yet, although an ionized jet is the most probable explanation. As mentioned in Sec. 4.5.1, the MIDI visibilities for AFGL 2136 show significant elongation parallel to a circumstellar disk, which was revealed in near-infrared polarimetric images by Minchin et al. (1991), and perpendicular to the molecular outflow found by Kastner et al. (1994). The FWHM size of the two-dimensional Gaussian in our geometric model is 43 mas (86 AU at 2 kpc), and the correlated flux levels (Fig. 4.11) are well reproduced by the foreground-absorption model described in Sec. 4.4.2.

AFGL 4176

AFGL 4176 is a southern high-luminosity MYSO (Henning et al., 1984; Persi et al., 1986).

The position angle and elongation derived from the 2D1D model here are consistent with the more complicated disk-model presented by Boley et al. (2012). The correlated flux (Fig. 4.12) is reproduced well by our absorption model at shorter baselines, with the fits becoming progressively worse towards longer baselines, which we find consistent with the expectation that emission at these angular scales is dominated by hot dust (Boley et al., 2012). A more extensive discussion to this source is provided in Chapter 6 of this thesis.

G305.20+0.21

The survey papers by Walsh et al. (1999, 2001) established the presence of a bright compact infrared source within the star-forming complex G305. There is an H II region some $10''$ to the southwest of it (Walsh et al., 2007), but the IR source itself is not associated with centimeter free-free emission (Phillips et al., 1998; Walsh et al., 2007). The extrapolated IRAS luminosity is $\gtrsim 10^5$ $L_\odot$ (Walsh et al., 2001), which together with the cm non-detection supports our view that this object is a massive YSO in a pre-UCH II-region stage. Further interest is triggered by the presence of a group of aligned class-II methanol masers coincident with this IR object (component G305.202+0.207 in the work by Phillips et al., 1998). Soon after the finding of a number of such sources (including G305), it was speculated that such aligned masers might trace edge-on circumstellar disks (Norris et al., 1998). This hypothesis, however, is not supported by many subsequent studies (e.g. De Buizer, 2003; De Buizer et al., 2012).

The geometric fits for this object indicate a large (200 AU at 4.8 kpc) structure, elongated along a position angle of 27°. The correlated flux levels (Fig. 4.13) show features which cannot be reproduced by our absorption model.

IRAS 13481-6124

Though it was identified as a MYSO in the 1980s (Persson and Campbell, 1987), and was found to feature an ionized wind (Beck et al., 1991), there were not many more observational studies available for this southern object until recently. The discoveries of both a disk and a jet/outflow system, however, have been recently reported around this MYSO (Kraus et al., 2010; Stecklum et al., 2010).

Despite the good *uv* coverage of the MIDI observations, the error bars on the parameters derived for 2D1D the geometric model are large (position angle $\sim 119 \pm 40°$, inclination angle $\sim 29 \pm 12°$). From near-infrared interferometric measurements, Kraus et al. (2010) inferred a position angle of the disk of 114°. The correlated flux levels (Fig. 4.15) are well reproduced by our absorption model at all baselines. A more extensive discussion to this source is provided in Chapter 5 of this thesis.

IRAS 17216-3801

After its initial identification as a MYSO by Persson and Campbell (1987), this interesting source was been somewhat neglected. This may have been caused by its location on the southern sky, and more than 1° away from the Galactic plane. It is very bright in the *K* band, which enabled early speckle observations by Leinert et al. (1997, 2001). However, these revealed just a faint (scattering) halo, but no more complex, spatially-resolved structures, and no binarity. The object bears some resemblance to IRAS 13481-6124 in terms of IR appearance and luminosity, but the presence of outflow or jet activity has not yet been investigated.

The geometrical fitting utilizing an overresolved component plus a 2D Gaussian shows that this Gaussian needs to be quite large in linear scale (FWHM ∼ 200 AU) in order to fit the data.

M8E-IR

The study by Simon et al. (1984) was the first work to disentangle the M8 East region into an UCH II region with no near-infrared counterpart[5] and a strong infrared source, subsequently called M8E-IR, which is around 7″ away. Simon et al. (1984) emphasized the similarities between M8E-IR and the BN object in Orion. M8E-IR was later confirmed not to be associated with free-free emission from ionized gas at wavelengths of 2 and 6 cm (cf. Molinari et al., 1998, and their source region Mol 37). Simon et al. (1985) speculated on the existence of a small circumstellar disk around M8E-IR based on thermal infrared lunar occultation data. Their indications for a small elongated structure came mainly from their 3.8 μm data, while their 10 μm data are in agreement with a more symmetric intensity distribution.

Our geometric fits of this object show that the compact mid-IR emission is elongated along the CO outflow reported by Mitchell et al. (1991). This is consistent with the work of Linz et al. (2009), who, using the same MIDI observations included in the present work, combined with radiative transfer modeling of the SED, concluded that the role of a circumstellar disk in this system is probably negligible.

M 17 SW IRS 1

This object is in the list of BN-type objects by Henning et al. (1984). It is also known as the Kleinmann-Wright (KW) object (Kleinmann and Wright, 1973), and is situated in the dusty south-western part of the M 17 star-forming complex. Porter et al. (1998) analyzed the *H*- and *K*-band spectra of this object, and concluded that they resemble the spectrum coming from a concealed Herbig Be star. Chini et al. (2004) revealed multiplicity within a few thousand AU in the near-infrared. However, the actual KW object is the dominating YSO in that core region, and is estimated to have a luminosity equivalent to that of an early B-type star. Follert et al. (2010) originally published the MIDI data included here, and used them to select appropriate

---

[5] Infrared emission from the UCH II region was revealed much later, and only in the mid-infrared at 24.5 μm (Linz et al., 2009; de Wit et al., 2009).

models from the Robitaille et al. (2007) model grid of YSOs. Our geometrical analysis agrees with their assessment that a strongly-inclined configuration ($\theta \gtrsim 60°$) is necessary to explain the observations.

M 17 UC 1

This object is a deeply-embedded young massive star in the M 17 complex. It is known to be associated with a hyper-compact H II region (Felli et al., 1980, 1984) with an electron density of greater than 10^5 cm^{-3}). Additionally, broad radio recombination lines have been found (Johnson et al., 1998). One of the interpretations for such line widths, which are in excess of the usual Doppler broadening, is the infall of material onto, and/or the rotation of, an accretion disk (e.g. Sewilo et al., 2004). In the infrared, Chini et al. (2000) found that UC 1 is weak at 1–2.2 μm wavelengths. However, there is another IR source $\sim$ 9000 AU away (IRS 5S), which is a stronger source in the near-infrared (but similarly bright in the N-band) which might form a bound high-mass system together with UC 1.

This object was not in our original target list, but was observed as a backup target during a different MIDI program on our request. Therefore, we have only a single visibility measurement. Hence, we can just derive a one-dimensional Gaussian size. Nevertheless, these data show that it is at least possible to obtain fringes for hyper-compact H II regions. The mid-infrared emission is not overresolved as a whole, as might be the tendency for more evolved ultra-compact H II regions (see our example of GM 24).

Mon R2 IRS 2

Mon R2 is a massive star forming region, with an UCH II region lying just of the center of a molecular core. There are several well-known compact infrared sources around this region, among them Mon R2 IRS 2. IRS 2 is situated in the geometrical center of a ring-like near-infrared structure, and has been shown to be the main source of illumination (Aspin and Walther, 1990). Furthermore, a large-scale bipolar CO outflow exists in the region (e.g. Giannakopoulou et al., 1997), but its association with IRS 2 is not established (e.g., Jaffe et al., 2003). IRS 2 has a strong infrared excess, but is not a source of free-free emission. It is unresolved in K-band speckle observations with UKIRT (Alvarez et al., 2004).

The derived mid-infrared emission is quite compact, similar to G305.20+0.21, which has a comparable amount of MIDI data. Hence, this might be an imprint of the lower luminosity of Mon R2 IRS 2.

4.6 Summary and conclusions

In this work, we presented the results of an eight-year program to observe massive young stellar objects with the two-telescope mid-infrared interferometric instrument MIDI on the Very Large Telescope Interferometer of the European Southern Observatory on Cerro Paranal, Chile. We measured spectrally-resolved, long-baseline interferometric visibilities in the 8–13 μm wavelength range for 20 massive YSOs, with projected baselines ranging from 5 to 130 m. Where available, we combined these data with previously-published measurements of the sources in our sample, both from MIDI and the Keck segment tilting experiment of Monnier et al. (2009).

Using simple geometric models of the visibilities at a wavelength of 10.6 μm, we derived emission scales and showed significant asymmetries in the majority of the objects. Although there is a general trend of increasing mid-infrared size with luminosity, we see a much looser correlation than has been reported for YSOs at near-infrared wavelengths. A comparison with literature information about disks and/or outflows shows that, in general, neither one of these components is solely responsible for the compact N-band emission. Consequently, caution should be used when attributing mid-infrared emission to a particular physical structure for objects which may have both an outflow and a disk. For some of the objects in our sample, the long-baseline MIDI measurements represent the first detection of any asymmetries; these results can thus be used in planning future observations to directly detect disk and/or outflow components in these sources.

For sources which show a deep silicate absorption feature, we fit a simple model to the correlated flux, consisting of a smooth (power-law) spectrum, extincted by a foreground screen of material with a column density and dust composition (a mix of large and small grains of magnesium-iron silicates, fit for each source) independent of projected baseline or position angle. In almost all cases, this model adequately reproduces the observed correlated fluxes, implying that the absorbing material is both largely uniform, and detached from the spatial scales probed by MIDI. Furthermore, many of the objects require a substantial fraction of large grains to fit the observed correlated flux, implying a significant amount of grain growth in the absorbing foreground material.

Acknowledgements. We thank J. Monnier for providing the reduced Keck data, J.-U. Pott for observing the object M17 UC1 upon our request, G. Meeus for providing the R CrA data, and J. Bouwman for useful discussions regarding the dust opacities.

References

Alvarez, C., Hoare, M., Glindemann, A., and Richichi, A.: 2004, Near-IR speckle imaging of massive young stellar objects. *Astronomy and Astrophysics* **427**, 505–518

Argon, A. L., Reid, M. J., and Menten, K. M.: 2000, Interstellar Hydroxyl Masers in the Galaxy. I. The VLA Survey. *Astrophysical Journal Supplement Series* **129**, 159–227

Aspin, C. and Walther, D. M.: 1990, Infrared imaging polarimetry of Monoceros R2 IRS. *Astronomy and Astrophysics* **235**, 387–394

Baxter, E. J., Covey, K. R., Muench, A. A., et al.: 2009, The Distance to NGC 2264. *Astronomical Journal* **138**, 963–974

Beck, S. C., Fischer, J., and Smith, H. A.: 1991, Infrared recombination lines of hydrogen from young objects in the southern Galactic plane. *Astrophysical Journal* **383**, 336–343

Boley, P. A., Linz, H., van Boekel, R., et al.: 2012, On the massive young stellar object AFGL 4176. High-spatial-resolution multi-wavelength observations and modeling. *Astronomy and Astrophysics* **547**, A88

Borges Fernandes, M., Kraus, M., Lorenz Martins, S., and de Araújo, F. X.: 2007, On the evolutionary stage of the unclassified B[e] star CD-42deg11721. *Monthly Notices of the Royal Astronomical Society* **377**, 1343–1362

Brugel, E. W., Mundt, R., and Buehrke, T.: 1984, Jets from young stars - The case of R Monocerotis. *Astrophysical Journal Letters* **287**, L73–L75

Casey, S. C. and Harper, D. A.: 1990, VY Monocerotis and the IC 446 region - Far-infrared and submillimeter images of a massive young stellar object and its environment. *Astrophysical Journal* **362**, 663–673

Chini, R., Hoffmeister, V. H., Kämpgen, K., et al.: 2004, The nature of the KW object. *Astronomy and Astrophysics* **427**, 849–853

Chini, R., Nielbock, M., and Beck, R.: 2000, The birth of massive twins in M 17. *Astronomy and Astrophysics* **357**, L33–L36

Cohen, M., Harvey, P. M., Wilking, B. A., and Schwartz, R. D.: 1984, Far-infrared studies of Herbig-Haro objects and their exciting stars. *Astrophysical Journal* **278**, 671–678

Cohen, R. J., Masheder, M. R. W., and Caswell, J. L.: 1995, Excited OH 4.7-GHz masers associated with IRAS far-infrared sources - II. *Monthly Notices of the Royal Astronomical Society* **274**, 808–820

Correia, S., Köhler, R., Meeus, G., and Zinnecker, H.: 2008, First Evidence for a Spatially Resolved Disk Structure around the Herbig Ae Star R CrA, in *The Power of Optical/IR Interferometry: Recent Scientific Results and 2nd Generation*, A. Richichi, F. Delplancke, F. Paresce, and A. Chelli (eds.), p. 175

De Buizer, J. M.: 2003, Testing the circumstellar disc hypothesis: a search for H_2 outflow signatures from massive young stellar objects with linearly distributed methanol masers. *Monthly Notices of the Royal Astronomical Society* **341**, 277–298

De Buizer, J. M., Morris, M. R., Becklin, E. E., et al.: 2012, First Science Observations with SOFIA/FORCAST: 6-37 μm Imaging of Orion BN/KL. *Astrophysical Journal Letters* **749**, L23

De Buizer, J. M., Redman, R. O., Longmore, S. N., Caswell, J., and Feldman, P. A.: 2009, SiO outflow signatures toward massive young stellar objects with linearly distributed methanol masers. *Astronomy and Astrophysics* **493**, 127–143

de Wit, W. J., Hoare, M. G., Fujiyoshi, T., et al.: 2009, Resolved 24.5 micron emission from massive young stellar objects. *Astronomy and Astrophysics* **494**, 157–178

de Wit, W. J., Hoare, M. G., Oudmaijer, R. D., et al.: 2011, Mid-infrared interferometry towards the massive young stellar object CRL 2136: inside the dust rim. *Astronomy and Astrophysics* **526**, L5

Dorschner, J., Begemann, B., Henning, T., Jaeger, C., and Mutschke, H.: 1995, Steps toward interstellar silicate mineralogy. II. Study of Mg-Fe-silicate glasses of variable composition.. *Astronomy and Astrophysics* **300**, 503

Felli, M., Churchwell, E., and Massi, M.: 1984, A high-resolution study of M17 at 1.3, 2, 6, and 21 CM. *Astronomy and Astrophysics* **136**, 53–64

Felli, M., Johnston, K. J., and Churchwell, E.: 1980, An unusual radio point source in M17. *Astrophysical Journal Letters* **242**, L157–L161

Follert, R., Linz, H., Stecklum, B., et al.: 2010, Mid-infrared interferometry of massive young stellar objects. II. Evidence for a circumstellar disk surrounding the Kleinmann-Wright object. *Astronomy and Astrophysics* **522**, A17

Fontani, F., Beltrán, M. T., Brand, J., et al.: 2005, Search for massive protostellar candidates in the southern hemisphere. I. Association with dense gas. *Astronomy and Astrophysics* **432**, 921–935

Giannakopoulou, J., Mitchell, G. F., Hasegawa, T. I., Matthews, H. E., and Maillard, J.-P.: 1997, The Star-forming Core of Monoceros R2. *Astrophysical Journal* **487**, 346

Grellmann, R., Ratzka, T., Kraus, S., et al.: 2011, Mid-infrared interferometry of the massive young stellar object NGC 2264 IRS 1. *Astronomy and Astrophysics* **532**, A109

Henning, T., Burkert, A., Launhardt, R., Leinert, C., and Stecklum, B.: 1998, Infrared imaging and millimetre continuum mapping of Herbig Ae/Be and FU Orionis stars. *Astronomy and Astrophysics* **336**, 565–586

Henning, T., Chini, R., and Pfau, W.: 1992, Submm/mm observations of the Monoceros R2 cloud core. *Astronomy and Astrophysics* **263**, 285–291

Henning, T., Friedemann, C., Gürtler, J., and Dorschner, J.: 1984, A catalogue of extremely young, massive and compact infrared objects. *Astronomische Nachrichten* **305**, 67–78

Henning, T., Pfau, W., and Altenhoff, W. J.: 1990, Infrared and radio emission from very young and massive stellar objects. *Astronomy and Astrophysics* **227**, 542–552

Herbst, W. and Racine, R.: 1976, R-associations. V. Monoceros R2.. *Astronomical Journal* **81**, 840–844

Hindson, L., Thompson, M. A., Urquhart, J. S., Clark, J. S., and Davies, B.: 2010, The G305 star-forming complex: wide-area molecular mapping of NH_3 and H_2O masers. *Monthly Notices of the Royal Astronomical Society* **408**, 1438–1451

Hoffmeister, V. H., Chini, R., Scheyda, C. M., et al.: 2008, The Stellar Population of M17. *Astrophysical Journal* **686**, 310–324

Jaffe, D. T., Zhu, Q., Lacy, J. H., and Richter, M.: 2003, Kinematics of Ultracompact H II Regions Revealed: High Spatial and Spectral Resolution Mapping of the 12.8 Micron [Ne II] Line in Monoceros R2. *Astrophysical Journal* **596**, 1053–1063

Jäger, C., Dorschner, J., Mutschke, H., Posch, T., and Henning, T.: 2003, Steps toward interstellar silicate mineralogy. VII. Spectral properties and crystallization behaviour of magnesium silicates produced by the sol-gel method. *Astronomy and Astrophysics* **408**, 193–204

Jiang, Z., Tamura, M., Fukagawa, M., et al.: 2005, A circumstellar disk associated with a massive protostellar object. *Nature* **437**, 112–115

Johnson, C. O., Depree, C. G., and Goss, W. M.: 1998, A High-Resolution VLA Study of M17-UC1. *Astrophysical Journal* **500**, 302

Juhász, A., Bouwman, J., Henning, T., et al.: 2010, Dust Evolution in Protoplanetary Disks Around Herbig Ae/Be Stars — the Spitzer View. *Astrophysical Journal* **721**, 431–455

Kastner, J. H., Weintraub, D. A., and Aspin, C.: 1992, The Juggler - A three-lobed near-infrared reflection nebula toward CRL 2136 = OH 17.6 + 0.2. *Astrophysical Journal* **389**, 357–368

Kastner, J. H., Weintraub, D. A., Snell, R. L., et al.: 1994, The massive molecular outflow from CRL 2136 IRS 1. *Astrophysical Journal* **425**, 695–706

Kleinmann, D. E. and Wright, E. L.: 1973, A New Infrared Source in M17. *Astrophysical Journal Letters* **185**, L131

Kraus, S., Calvet, N., Hartmann, L., et al.: 2012, On the Nature of the Herbig B[e] Star Binary System V921 Scorpii: Geometry and Kinematics of the Circumprimary Disk on Sub-AU Scales. *Astrophysical Journal* **752**, 11

Kraus, S., Hofmann, K.-H., Malbet, F., et al.: 2009, Revealing the sub-AU asymmetries of the inner dust rim in the disk around the Herbig Ae star R Coronae Austrinae. *Astronomy and Astrophysics* **508**, 787–803

Kraus, S., Hofmann, K.-H., Menten, K. M., et al.: 2010, A hot compact dust disk around a massive young stellar object. *Nature* **466**, 339–342

Leinert, C., Graser, U., Waters, L. B. F. M., et al.: 2003, Ten-micron instrument MIDI: getting ready for observations on the VLTI, in *Society of Photo-Optical Instrumentation Engineers (SPIE) Conference Series*, W. A. Traub (ed.), Vol. 4838 of *Society of Photo-Optical Instrumentation Engineers (SPIE) Conference Series*, pp 893–904

Leinert, C., Haas, M., Ábrahám, P., and Richichi, A.: 2001, Halos around Herbig Ae/Be stars - more common than for the less massive T Tauri stars. *Astronomy and Astrophysics* **375**, 927–936

Leinert, C., Richichi, A., and Haas, M.: 1997, Binaries among Herbig Ae/Be stars.. *Astronomy and Astrophysics* **318**, 472–484

Leinert, C., van Boekel, R., Waters, L. B. F. M., et al.: 2004, Mid-infrared sizes of circumstellar disks around Herbig Ae/Be stars measured with MIDI on the VLTI. *Astronomy and Astrophysics* **423**, 537–548

Linz, H., Follert, R., Boley, P. A., et al.: 2011, MIDI interferometry of massive YSOs: Updates on the MPIA programme. *arXiv 1111.0821*

Linz, H., Henning, T., Feldt, M., et al.: 2009, Mid-infrared interferometry of massive young stellar objects. I. VLTI and Subaru observations of the enigmatic object M8E-IR. *Astronomy and Astrophysics* **505**, 655–661

Longmore, S. N., Burton, M. G., Minier, V., and Walsh, A. J.: 2006, Mid-infrared source multiplicity within hot molecular cores traced by methanol masers. *Monthly Notices of the Royal Astronomical Society* **369**, 1196–1200

Menten, K. M., Reid, M. J., Forbrich, J., and Brunthaler, A.: 2007, The distance to the Orion Nebula. *Astronomy and Astrophysics* **474**, 515–520

Menten, K. M. and van der Tak, F. F. S.: 2004, Very compact radio emission from high-mass protostars. I. CRL 2136: Continuum and water maser observations. *Astronomy and Astrophysics* **414**, 289–298

Minchin, N. R., Hough, J. H., Burton, M. G., and Yamashita, T.: 1991, Near-infrared imaging polarimetry of bipolar nebulae. IV - GL 490, GL 2789 and GL 2136. *Monthly Notices of the Royal Astronomical Society* **251**, 522–528

Miroshnichenko, A. S., Levato, H., Bjorkman, K. S., et al.: 2004, Properties of galactic B[e] supergiants. III. MWC 300. *Astronomy and Astrophysics* **417**, 731–743

Mitchell, G. F., Maillard, J.-P., and Hasegawa, T. I.: 1991, Episodic outflows from high-mass protostars. *Astrophysical Journal* **371**, 342–356

Molinari, S., Brand, J., Cesaroni, R., Palla, F., and Palumbo, G. G. C.: 1998, A search for precursors of ultracompact H II regions in a sample of luminous IRAS sources. II. VLA observations. *Astronomy and Astrophysics* **336**, 339–351

Monnier, J. D. and Millan-Gabet, R.: 2002, On the Interferometric Sizes of Young Stellar Objects. *Astrophysical Journal* **579**, 694–698

Monnier, J. D., Millan-Gabet, R., Billmeier, R., et al.: 2005, The Near-Infrared Size-Luminosity Relations for Herbig Ae/Be Disks. *Astrophysical Journal* **624**, 832–840

Monnier, J. D., Tuthill, P. G., Ireland, M., et al.: 2009, Mid-Infrared Size Survey of Young Stellar Objects: Description of Keck Segment-Tilting Experiment and Basic Results. *Astrophysical Journal* **700**, 491–505

Norris, R. P., Byleveld, S. E., Diamond, P. J., et al.: 1998, Methanol Masers as Tracers of Circumstellar Disks. *Astrophysical Journal* **508**, 275–285

Olofsson, J., Augereau, J.-C., van Dishoeck, E. F., et al.: 2010, C2D Spitzer-IRS spectra of disks around T Tauri stars. V. Spectral decomposition. *Astronomy and Astrophysics* **520**, A39

Ortiz, J. L., Sugerman, B. E. K., de La Cueva, I., et al.: 2010, Observation of light echoes around very young stars. *Astronomy and Astrophysics* **519**, A7

Persi, P., Ferrari-Toniolo, M., and Spinoglio, L.: 1986, Infrared studies of southern AFGL sources. II - GL4176 and GL4182: two sources in star forming regions. *Astronomy and Astrophysics* **157**, 29–34

Persson, S. E. and Campbell, B.: 1987, Identification of new young stellar objects associated with IRAS point sources. I - The southern Galactic plane. *Astronomical Journal* **94**, 416–428

Phillips, C. J., Norris, R. P., Ellingsen, S. P., and McCulloch, P. M.: 1998, Methanol masers and their environment at high resolution. *Monthly Notices of the Royal Astronomical Society* **300**, 1131–1157

Porter, J. M., Drew, J. E., and Lumsden, S. L.: 1998, Broad band infrared spectroscopy of massive young stellar objects. *Astronomy and Astrophysics* **332**, 999–1016

Prisinzano, L., Damiani, F., Micela, G., and Sciortino, S.: 2005, The star formation region NGC 6530: Distance, ages and initial mass function. *Astronomy and Astrophysics* **430**, 941–957

Reid, M. J., Menten, K. M., Zheng, X. W., et al.: 2009, Trigonometric Parallaxes of Massive Star-Forming Regions. VI. Galactic Structure, Fundamental Parameters, and Noncircular Motions. *Astrophysical Journal* **700**, 137–148

Robitaille, T. P., Whitney, B. A., Indebetouw, R., and Wood, K.: 2007, Interpreting Spectral Energy Distributions from Young Stellar Objects. II. Fitting Observed SEDs Using a Large Grid of Precomputed Models. *Astrophysical Journal Supplement Series* **169**, 328–352

Rygl, K. L. J., Brunthaler, A., Reid, M. J., et al.: 2010, Trigonometric parallaxes of 6.7 GHz methanol masers. *Astronomy and Astrophysics* **511**, A2

Schreyer, K., Stecklum, B., Linz, H., and Henning, T.: 2003, NGC 2264 IRS 1: The Central Engine and Its Cavity. *Astrophysical Journal* **599**, 335–341

Sewilo, M., Churchwell, E., Kurtz, S., Goss, W. M., and Hofner, P.: 2004, Broad Radio Recombination Lines from Hypercompact H II Regions. *Astrophysical Journal* **605**, 285–299

Simon, M., Cassar, L., Felli, M., et al.: 1984, Star formation in the M8E region. *Astrophysical Journal* **278**, 170–175

Simon, M., Peterson, D. M., Longmore, A. J., Storey, J. W. V., and Tokunaga, A. T.: 1985, Lunar occultation observations of M8E-IR. *Astrophysical Journal* **298**, 328–339

Stecklum, B., Caratti o Garatti, A., Linz, H., et al.: 2010, IRAS 13481-6124 - A Young High-Mass Star Driving a Parsec-scale Outflow, in *Online Proceedings of the Great Barriers in High-Mass Star Formation Conference*, A. Walsh (ed.), Vol. 1 of *Online Proceedings of the Great Barriers in High-Mass Star Formation Conference*, p. E15

Tamura, M., Gatley, I., Joyce, R. R., et al.: 1991, Infrared polarization images of star-forming regions. I - The ubiquity of bipolar structure. *Astrophysical Journal* **378**, 611–627

Tapia, M., Rodríguez, L. F., Persi, P., Roth, M., and Gómez, M.: 2009, The Intermediate-Mass Embedded Cluster GM 24 Revisited: New Infrared and Radio Observations. *Astronomical Journal* **137**, 4127–4139 van Boekel, R., Min, M., Leinert, C., et al.: 2004, The building blocks of planets within the 'terrestrial' region of protoplanetary disks. *Nature* **432**, 479–482

Verhoeff, A. P., Waters, L. B. F. M., van den Ancker, M. E., et al.: 2012, A mid-IR study of the circumstellar environment of Herbig Be stars. *Astronomy and Astrophysics* **538**, A101

Walsh, A. J., Bertoldi, F., Burton, M. G., and Nikola, T.: 2001, Mid-infrared observations of methanol maser sites and ultracompact H ii regions: signposts of high-mass star formation. *Monthly Notices of the Royal Astronomical Society* **326**, 36–56

Walsh, A. J., Burton, M. G., Hyland, A. R., and Robinson, G.: 1999, Studies of ultracompact HII regions - III. Near-infrared survey of selected regions. *Monthly Notices of the Royal Astronomical Society* **309**, 905–922

Walsh, A. J., Chapman, J. F., Burton, M. G., Wardle, M., and Millar, T. J.: 2007, Australia Telescope Compact Array 1.2-cm observations of the massive star-forming region G305.2+0.2. *Monthly Notices of the Royal Astronomical Society* **380**, 1703–1714

Wang, Y., Weigelt, G., Kreplin, A., et al.: 2012, AMBER/VLTI observations of the B[e] star MWC 300. *arXiv 1208.5882*

Yao, Y., Hirata, N., Ishii, M., et al.: 1997, Near-Infrared Polarimetric Study of Monoceros R2 IRS. *Astrophysical Journal* **490**, 281

4.A Supplementary material

Table 4.4: Observation log

Source	Date/time (UTC)	Telescopes	Proj. baseline (m)	Position angle (deg.)	Avg. visibility
AFGL 2136†	2005-06-24 03:49	UT3-UT4	61.3	107.0	0.03
	2005-06-26 03:02	UT1-UT2	53.5	14.0	0.01
	2006-05-18 08:44	UT2-UT3	46.4	45.9	0.04
	2008-06-23 08:04	UT2-UT3	42.6	47.4	0.03
AFGL 4176	2005-03-02 08:08	UT3-UT4	61.6	112.1	0.02
	2005-06-24 04:54	UT3-UT4	61.8	169.3	0.02
	2005-06-25 22:50	UT1-UT2	49.3	19.3	0.07
	2005-06-26 02:05	UT1-UT2	41.9	49.8	0.08
	2005-06-26 03:27	UT1-UT2	36.3	62.4	0.04
	2005-06-27 03:31	UT2-UT3	30.3	85.6	0.08
	2006-02-22 05:46	E0-G0	16.0	41.9	0.30
	2006-04-18 08:01	D0-G0	26.5	121.4	0.06
	2006-04-24 07:30	E0-G0	13.4	119.4	0.31
	2007-02-11 06:24	E0-G0	16.0	40.5	0.23
	2007-02-12 06:18	G0-H0	31.9	40.0	0.13
	2007-03-15 07:08	G0-H0	31.2	77.7	0.11
	2007-03-16 09:13	G0-H0	28.3	106.8	0.07
	2007-04-18 04:55	E0-G0	15.6	77.8	0.20
	2007-05-24 01:51	E0-G0	15.8	68.7	0.27
	2007-06-19 02:35	G0-H0	28.9	101.0	0.06
	2007-07-03 01:31	E0-G0	14.6	98.9	0.28
	2011-05-09 02:15	B2-C1	9.8	21.7	0.47
	2011-05-09 02:49	B2-C1	9.6	27.0	0.46
	2011-05-09 03:14	B2-C1	9.5	31.0	0.49
	2011-05-09 03:29	B2-C1	9.4	33.4	0.52
	2011-05-09 04:54	B2-D0	25.9	46.4	0.18
	2011-05-09 05:27	B2-D0	24.7	51.6	0.16
	2011-05-09 08:28	B2-C1	5.3	80.9	0.61
	2011-05-10 02:23	B2-D0	29.3	23.5	0.20
	2011-05-10 03:46	B2-D0	27.7	36.7	0.19
	2012-02-01 09:04	A1-B2	10.7	103.5	0.51
	2012-02-24 05:20	D0-H0	63.8	37.3	0.06
	2012-02-24 05:30	D0-H0	63.8	39.8	0.06
	2012-02-24 09:29	D0-H0	59.9	92.0	0.05
	2012-03-26 09:05	I1-K0	32.4	38.6	0.11
	2012-03-26 09:41	I1-K0	30.8	43.1	0.10
	2012-03-27 05:21	I1-K0	38.0	9.1	0.10
	2012-03-27 05:26	I1-K0	37.9	9.7	0.09
	2012-03-27 05:34	I1-K0	37.8	10.9	0.09
	2012-03-27 07:09	I1-K0	36.2	23.8	0.10
	2012-03-29 04:08	I1-K0	38.2	179.9	0.09
	2012-04-18 06:39	D0-H0	57.8	101.7	0.03
	2012-04-18 06:49	D0-H0	57.2	104.0	0.03
G305.20+0.21†	2005-03-02 07:13	UT3-UT4	61.0	106.9	0.03
	2005-02-27 03:35	UT2-UT3	44.7	4.8	0.03
	2005-03-02 05:26	UT3-UT4	56.7	83.4	0.02
	2005-03-02 06:10	UT3-UT4	58.9	93.4	0.03
	2005-06-24 02:46	UT3-UT4	62.3	146.7	0.01
	2005-06-26 01:20	UT1-UT2	42.5	48.1	0.03
HIP 90617	2009-05-03 08:34	D0-G1	69.2	133.6	0.15

Source	Date/time (UTC)	Telescopes	Proj. baseline (m)	Position angle (deg.)	Avg. visibility
	2009-05-04 06:21	G1-H0	67.6	174.3	0.09
	2009-05-04 08:52	G1-H0	68.4	11.2	0.06
	2009-06-30 05:24	A0-K0	127.4	73.2	0.05
	2009-06-30 05:35	A0-K0	126.8	73.4	0.05
	2009-06-30 06:06	A0-K0	123.5	73.8	0.06
	2009-06-30 08:26	A0-K0	84.6	70.8	0.16
	2009-07-01 04:25	A0-G1	90.0	114.5	0.10
	2009-07-04 05:56	E0-H0	46.0	73.8	0.15
	2009-07-04 07:26	E0-H0	37.7	72.9	0.23
	2009-07-05 04:28	E0-G0	16.0	72.3	0.67
	2009-07-06 05:57	E0-H0	45.4	73.9	0.14
	2009-07-07 05:01	G0-H0	31.8	73.3	0.07
	2010-05-04 09:34	A0-K0	125.6	73.6	0.04
	2010-05-20 05:49	H0-I1	40.7	142.8	0.35
	2012-05-01 07:34	B2-D0	31.3	21.0	0.36
	2012-05-02 05:59	A1-B2	10.2	113.2	0.70
	2012-05-02 09:55	B2-D0	33.8	33.3	0.29
IRAS 13481-6124	2009-02-15 04:55	UT2-UT3	44.9	3.4	0.14
	2009-05-02 04:04	D0-H0	62.4	77.3	0.11
	2009-05-03 04:58	D0-G1	67.6	141.1	0.13
	2009-07-02 00:41	G1-K0	73.1	38.9	0.11
	2009-07-04 00:58	E0-H0	45.1	90.7	0.21
	2009-07-04 23:23	E0-G0	15.8	71.0	0.39
	2009-07-05 23:43	E0-H0	46.9	75.9	0.13
	2009-07-06 02:49	E0-H0	40.0	118.7	0.17
	2009-07-06 23:23	G0-H0	31.5	72.5	0.23
	2009-07-07 02:42	G0-H0	26.8	117.9	0.23
	2009-07-07 02:53	G0-H0	26.4	120.7	0.22
	2010-05-04 01:45	A0-K0	128.0	48.6	0.07
	2010-05-04 04:32	A0-K0	122.5	84.8	0.06
	2010-05-05 02:03	G1-K0	79.8	16.0	0.13
	2010-05-05 03:54	A0-G1	87.9	114.1	0.11
	2010-05-05 04:06	A0-G1	88.3	116.4	0.10
	2010-05-05 05:49	A0-G1	90.4	138.2	0.08
	2010-05-05 07:24	A0-G1	90.4	159.3	0.08
	2012-05-01 05:01	B2-C1	9.0	41.6	0.71
	2012-05-01 07:10	B2-D0	22.1	61.2	0.33
	2012-05-02 05:15	A1-B2	11.2	128.9	0.46
	2012-05-02 06:50	A1-C1	13.5	115.3	0.33
	2012-05-02 07:50	A1-D0	22.0	98.8	0.20
	2012-05-02 08:40	A1-B2	11.3	174.5	0.49
	2012-05-02 09:08	B2-D0	15.4	81.4	0.33
IRAS 17216-3801	2012-05-01 05:48	B2-C1	11.3	13.9	0.37
	2012-05-01 09:23	A1-B2	11.0	134.1	0.34
	2012-05-01 09:46	B2-C1	10.0	40.2	0.41
	2012-05-02 04:34	A1-B2	8.9	91.5	0.41
	2012-05-02 07:11	A1-C1	16.0	69.6	0.22
	2012-05-02 08:14	A1-D0	34.2	51.5	0.15
	2012-05-02 09:33	B2-D0	30.5	39.5	0.11
M17 SW IRS1	2005-06-24 08:23	UT3-UT4	43.9	140.7	0.09
	2005-06-26 04:25	UT1-UT2	55.8	24.3	0.03
	2006-05-18 09:59	UT2-UT3	43.5	48.4	0.30
	2006-08-10 01:27	D0-G0	31.7	69.6	0.45
	2006-08-13 00:22	E0-G0	15.1	64.7	0.69

Source	Date/time (UTC)	Telescopes	Proj. baseline (m)	Position angle (deg.)	Avg. visibility
M17 UC1[†]	2006-06-12 09:33	UT3-UT4	41.3	146.9	0.03
M8E-IR[†]	2004-06-05 08:06	UT1-UT3	96.8	42.7	0.09
	2004-06-05 09:53	UT1-UT3	82.8	44.6	0.08
	2004-08-01 01:50	UT2-UT3	46.6	38.4	0.26
	2005-03-02 08:58	UT3-UT4	46.8	94.1	0.17
	2005-06-24 07:36	UT3-UT4	51.6	137.8	0.24
	2005-06-26 00:26	UT1-UT2	55.7	173.4	0.15
Mon R2 IRS2	2009-02-15 00:48	UT2-UT3	44.6	39.9	0.19
	2009-11-14 04:11	E0-G0	10.8	55.8	0.78
	2009-11-15 04:06	E0-G0	10.7	55.4	0.84
	2009-11-15 05:16	G0-H0	26.9	64.9	0.19
	2009-11-15 06:39	G0-H0	31.1	70.6	0.20
Mon R2 IRS3 A	2005-02-27 02:26	UT2-UT3	46.2	46.3	0.04
	2006-03-13 01:19	UT3-UT4	52.9	117.0	0.02
	2009-10-02 08:04	G0-H0	26.6	64.4	0.11
	2009-11-15 04:36	E0-G0	12.0	60.3	0.24
	2009-11-15 06:59	G0-H0	31.6	71.5	0.09
Mon R2 IRS3 B	2005-02-27 02:49	UT2-UT3	45.6	46.2	0.16
	2006-03-13 02:20	UT3-UT4	44.1	125.0	0.17
NGC 2264 IRS1[†]	2009-02-15 01:12	UT2-UT3	40.2	43.9	0.17
Orion BN	2005-02-27 00:29	UT2-UT3	46.2	44.1	0.07
	2006-09-14 08:36	E0-G0	13.0	64.3	0.29
	2006-10-20 06:00	D0-G0	24.8	62.7	0.25
	2006-12-15 01:44	E0-G0	11.0	57.8	0.28
	2006-12-15 06:41	E0-G0	14.8	73.6	0.35
	2007-02-09 03:04	G0-H0	29.4	73.6	0.25
R CrA	2004-07-09 09:10	UT2-UT3	27.4	63.5	0.48
	2004-07-28 02:04	UT2-UT3	46.6	30.5	0.20
	2005-06-23 07:33	UT1-UT4	115.3	76.1	0.26
	2005-06-25 07:29	UT1-UT4	114.6	76.6	0.09
	2005-06-25 07:39	UT1-UT4	112.5	77.8	0.10
	2005-06-26 05:57	UT1-UT4	127.5	65.3	0.10
	2005-06-28 04:40	UT3-UT4	61.2	105.0	0.22
	2005-06-28 07:40	UT3-UT4	58.8	134.5	0.24
	2005-07-21 01:29	UT3-UT4	53.3	90.8	0.32
	2005-07-21 02:26	UT3-UT4	58.7	98.9	0.22
	2005-07-21 04:35	UT3-UT4	62.3	117.6	0.33
	2005-09-18 02:10	UT1-UT4	111.2	78.5	0.18
	2009-05-03 09:33	D0-G1	71.4	138.5	0.20
	2009-05-04 07:06	G1-H0	70.1	175.9	0.18
	2009-05-04 09:33	G1-H0	69.5	12.0	0.17
	2009-07-01 06:55	A0-G1	88.3	133.1	0.15
	2009-07-04 08:36	E0-H0	32.3	106.1	0.54
	2009-07-05 01:21	E0-G0	14.0	32.5	0.67
	2009-07-05 05:21	E0-G0	15.8	76.0	0.37
	2009-07-06 04:43	E0-H0	47.9	70.9	0.34
	2009-07-06 07:38	E0-H0	37.8	96.8	0.36
	2009-07-07 00:56	G0-H0	27.5	28.4	0.17
	2009-07-07 01:10	G0-H0	27.9	31.8	0.16
R Mon	2010-01-13 04:29	D0-G1	61.9	130.9	0.26

Source	Date/time (UTC)	Telescopes	Proj. baseline (m)	Position angle (deg.)	Avg. visibility
	2010-01-14 05:05	D0-H0	63.3	71.1	0.17
	2010-01-16 02:24	E0-G0	14.1	75.1	0.56
	2010-01-16 05:19	E0-H0	46.7	69.9	0.22
	2010-01-19 04:43	G1-K0	85.3	34.7	0.13
	2010-01-21 02:40	A0-K0	120.6	74.8	0.06
	2010-01-21 06:02	A0-G1	56.8	116.9	0.22
S255 IRS3	2010-01-15 03:31	E0-G0	15.8	74.8	0.28
	2010-01-16 03:46	E0-H0	47.8	73.5	0.07
	2010-01-17 02:54	G0-H0	30.8	76.7	0.10
	2010-01-17 03:05	G0-H0	31.1	76.0	0.10
	2010-01-17 04:40	E0-H0	47.5	68.9	0.08
V1028 Cen	2009-05-02 02:41	D0-H0	63.8	68.8	0.28
	2009-05-02 07:09	D0-H0	43.8	124.3	0.22
	2009-07-03 23:28	E0-H0	46.7	78.8	0.43
	2009-07-05 00:18	E0-G0	14.9	88.6	0.72
	2009-07-06 01:12	E0-H0	41.0	100.0	0.33
	2009-07-07 00:08	G0-H0	29.8	88.2	0.48
	2010-05-20 06:28	H0-I1	40.0	9.3	0.15
	2010-05-21 04:08	E0-H0	41.4	98.7	0.63
	2012-05-01 06:18	B2-C1	8.4	50.1	0.70
	2012-05-02 06:15	A1-B2	11.0	152.1	0.69
V921 Sco	2009-05-02 08:33	D0-H0	59.0	87.2	0.58
	2009-05-03 07:49	D0-G1	71.2	141.0	0.42
	2009-05-04 04:03	G1-H0	67.7	169.0	0.38
	2009-05-04 08:08	G1-H0	66.8	16.2	0.44
	2009-06-30 00:01	A0-K0	118.7	36.4	0.25
	2009-06-30 00:36	A0-K0	121.9	44.2	0.29
	2009-06-30 06:51	A0-K0	88.5	112.4	0.25
	2009-07-01 03:20	A0-G1	90.2	117.5	0.31
	2009-07-01 04:46	A0-G1	89.6	132.6	0.25
	2009-07-02 01:11	G1-K0	89.3	12.9	0.31
	2009-07-04 02:08	E0-H0	48.0	64.6	0.81
	2009-07-04 06:34	E0-H0	33.3	112.1	0.66
	2009-07-04 06:49	E0-H0	31.8	115.9	0.79
	2009-07-06 02:03	E0-H0	48.0	65.2	0.73
	2009-07-06 06:50	E0-H0	30.9	118.2	0.72
	2009-07-07 02:16	G0-H0	32.0	68.0	1.03
	2009-07-07 05:18	G0-H0	26.3	98.5	1.03
	2009-07-07 07:03	G0-H0	19.4	123.2	0.81
	2010-05-04 03:08	A0-K0	115.4	27.4	0.15
	2010-05-04 05:13	A0-K0	125.8	54.5	0.19
	2010-05-04 08:23	A0-K0	118.5	86.7	0.31
	2010-05-04 10:04	A0-K0	97.1	105.2	0.29
	2010-05-05 06:34	A0-G1	89.1	112.7	0.26
	2010-05-05 08:35	A0-G1	89.5	133.3	0.32
	2010-05-05 09:22	A0-G1	87.7	142.7	0.33
	2010-05-05 10:08	A0-G1	85.7	152.6	0.30
	2010-05-20 05:11	H0-I1	38.5	143.9	0.61
	2010-05-20 07:01	H0-I1	40.2	158.1	0.56
VY Mon	2010-01-13 03:23	D0-G1	67.2	128.4	0.33
	2010-01-14 03:45	D0-H0	63.2	74.0	0.39
	2010-01-15 04:19	E0-G0	16.0	72.5	0.82
	2010-01-16 04:37	E0-H0	47.8	71.5	0.43
	2010-01-17 03:43	G0-H0	31.8	73.7	0.65

Source	Date/time (UTC)	Telescopes	Proj. baseline (m)	Position angle (deg.)	Avg. visibility
	2010-01-19 02:56	G1-K0	75.1	28.7	0.17
	2010-01-19 05:51	G1-K0	89.2	35.8	0.13
	2010-01-22 03:58	A0-K0	127.9	72.2	0.16
Sources without fringe detections:					
GGD 27	2004-06-02 04:00	UT2-UT3	43.9	21.6	—
GM 24	2006-05-18 03:39	UT2-UT3	46.3	36.2	—
	2006-05-26 08:34	D0-G0	25.2	76.5	—
IRAS 16164-5046	2009-05-02 06:16	D0-H0	63.5	251.7	—
	2009-05-03 05:33	D0-G1	65.4	303.8	—
	2009-07-05 03:16	G0-H0	30.3	265.4	—
Orion SC3	2005-02-27 01:38	UT2-UT3	46.5	46.1	—

Notes. † Cannot be observed with the ATs due to performance limitations of the STRAP/AO guiding system (cf. Linz et al., 2011).

Table 4.5: Parameters of geometric fits to 10.6 μm visibilities

Source	1D Gaussian	1D Gaussian OR		2D Gaussian OR				2D Gaussian + 1D Gaussian				
	FWHM (mas)	$V(0)$	FWHM (mas)	$V(0)$	FWHM (mas)	ϕ (deg)	θ (deg)	F_{2D}/F_{1D}	FWHM$_{2D}$ (mas)	FWHM$_{1D}$ (mas)	ϕ (deg)	θ (deg)
AFGL 2136	$147.^{+2.0}_{-2.0}$	$0.942^{+0.013}_{-0.013}$	$140.^{+2.7}_{-2.8}$	$0.946^{+0.012}_{-0.014}$	$148.^{+3.8}_{-4.1}$	$51.6^{+15.}_{-11.}$	$28.4^{+3.3}_{-6.5}$	$0.700^{+0.087}_{-0.081}$	$42.8^{+2.8}_{-1.2}$	$243.^{+18.}_{-15.}$	$33.6^{+12.}_{-15.}$	$46.2^{+8.4}_{-7.1}$
AFGL 4176	$71.1^{+1.8}_{-1.2}$	$0.399^{+0.039}_{-0.047}$	$49.3^{+2.1}_{-2.8}$	$0.426^{+0.031}_{-0.033}$	$57.9^{+2.0}_{-1.6}$	$108.^{+2.9}_{-3.0}$	$52.1^{+2.1}_{-1.9}$	$0.101^{+0.018}_{-0.010}$	$23.5^{+3.2}_{-1.7}$	$103.^{+4.1}_{-3.4}$	$116.^{+6.8}_{-6.0}$	$60.4^{+7.4}_{-6.6}$
G305.20+0.21	$48.8^{+1.3}_{-0.86}$	$0.0402^{+0.023}_{-0.0077}$	$17.6^{+4.2}_{-5.7}$	$0.0409^{+0.080}_{-0.0062}$	$35.3^{+2.5}_{-9.9}$	$23.6^{+13.}_{-22.}$	$47.2^{+9.2}_{-7.2}$					
HIP 90617	$50.7^{+2.5}_{-1.9}$	$1.00^{+0.011}_{-0.010}$	$50.8^{+2.8}_{-1.9}$	$0.989^{+0.011}_{-0.010}$	$52.3^{+4.0}_{-2.2}$	$85.9^{+4.1}_{-16.}$	$62.9^{+4.6}_{-2.6}$	$0.141^{+0.031}_{-0.023}$	$12.6^{+2.4}_{-2.3}$	$60.5^{+3.0}_{-2.4}$	$26.8^{+22.}_{-16.}$	$66.8^{+9.5}_{-14.}$
IRAS 13481-6124	$67.5^{+3.6}_{-3.8}$	$0.269^{+0.034}_{-0.025}$	$15.4^{+2.6}_{-1.9}$	$0.290^{+0.031}_{-0.035}$	$19.5^{+3.0}_{-3.4}$	$105.^{+26.}_{-41.}$	$45.1^{+7.2}_{-10.}$	$0.232^{+0.038}_{-0.023}$	$11.5^{+2.3}_{-1.5}$	$99.6^{+8.7}_{-5.4}$	$119.^{+47.}_{-38.}$	$28.6^{+11.}_{-12.}$
IRAS 17216-3801	$99.8^{+8.2}_{-6.8}$	$0.373^{+0.074}_{-0.049}$	$39.7^{+5.4}_{-5.9}$	$0.424^{+0.14}_{-0.068}$	$65.7^{+45.}_{-15.}$	$138.^{+24.}_{-29.}$	$61.7^{+9.1}_{-13.}$					
M17 SW IRS1	$39.0^{+1.2}_{-0.86}$	$0.980^{+0.18}_{-0.20}$	$38.9^{+1.6}_{-1.7}$	$0.701^{+0.18}_{-0.16}$	$43.3^{+14.}_{-2.6}$	$170.^{+9.0}_{-16.}$	$67.1^{+12.}_{-14.}$					
M17 UC1	$52.0^{+2.5}_{-1.7}$											
M8E-IR	$29.8^{+1.2}_{-1.0}$	$0.251^{+0.061}_{-0.042}$	$13.8^{+2.3}_{-2.2}$	$0.347^{+0.14}_{-0.075}$	$22.2^{+3.9}_{-6.2}$	$124.^{+26.}_{-23.}$	$45.9^{+7.7}_{-11.}$					
Mon R2 IRS2	$51.1^{+2.1}_{-1.6}$	$0.773^{+0.17}_{-0.19}$	$45.8^{+3.7}_{-6.3}$									
Mon R2 IRS3 A	$115.^{+7.6}_{-8.1}$	$0.250^{+0.043}_{-0.033}$	$36.1^{+1.9}_{-1.8}$	$0.282^{+0.052}_{-0.053}$	$40.8^{+3.1}_{-3.0}$	$81.7^{+31.}_{-27.}$	$45.2^{+18.}_{-15.}$					
Mon R2 IRS3 B	$34.7^{+1.5}_{-1.1}$											
NGC 2264 IRS1	$38.3^{+2.4}_{-1.9}$											
Orion BN	$103.^{+5.5}_{-4.4}$	$0.351^{+0.028}_{-0.031}$	$31.4^{+1.4}_{-1.3}$									
R CrA	$82.4^{+3.1}_{-3.9}$	$0.889^{+0.021}_{-0.0092}$	$52.6^{+7.5}_{-4.3}$	$0.856^{+0.010}_{-0.0089}$	$49.6^{+2.7}_{-2.5}$	$31.3^{+1.5}_{-1.3}$	$69.5^{+1.7}_{-1.9}$	$0.395^{+0.041}_{-0.031}$	$12.6^{+1.3}_{-1.4}$	$109.^{+4.2}_{-3.6}$	$12.2^{+9.3}_{-9.8}$	$53.2^{+9.0}_{-9.2}$
R Mon	$103.^{+3.7}_{-3.6}$	$0.980^{+0.017}_{-0.014}$	$99.9^{+4.6}_{-4.8}$	$0.981^{+0.015}_{-0.016}$	$103.^{+6.4}_{-5.2}$	$160.^{+54.}_{-30.}$	$18.0^{+6.6}_{-8.8}$	$0.438^{+0.22}_{-0.081}$	$14.0^{+3.1}_{-1.7}$	$132.^{+17.}_{-7.2}$	$52.0^{+42.}_{-28.}$	$48.3^{+17.}_{-13.}$
S255 IRS3	$63.5^{+9.2}_{-2.9}$	$0.222^{+0.072}_{-0.047}$	$27.8^{+5.6}_{-4.7}$									
V1028 Cen	$31.9^{+2.6}_{-1.7}$	$0.650^{+0.15}_{-0.18}$	$24.6^{+3.9}_{-7.8}$	$0.708^{+0.12}_{-0.10}$	$37.1^{+5.6}_{-4.8}$	$166.^{+9.6}_{-11.}$	$62.0^{+6.8}_{-8.3}$	$1.00^{+1.1}_{-0.26}$	$34.7^{+8.5}_{-5.8}$	$74.8^{+85.}_{-19.}$	$173.^{+8.1}_{-12.}$	$67.6^{+8.5}_{-9.2}$
V921 Sco	$14.1^{+0.65}_{-0.58}$	$0.779^{+0.10}_{-0.092}$	$12.3^{+1.1}_{-1.1}$	$0.848^{+0.091}_{-0.11}$	$15.0^{+1.4}_{-1.4}$	$159.^{+14.}_{-14.}$	$45.7^{+6.6}_{-11.}$					
VY Mon	$19.4^{+0.62}_{-0.45}$	$0.739^{+0.12}_{-0.14}$	$17.2^{+1.1}_{-2.3}$	0.623	19.0	0.437	59.5	$0.930^{+0.41}_{-0.28}$	$16.6^{+2.4}_{-1.9}$	$40.4^{+28.}_{-6.3}$	$187.^{+8.0}_{-13.}$	$63.6^{+9.0}_{-5.0}$

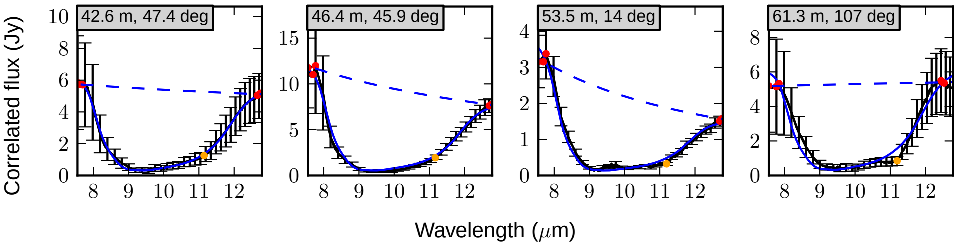

Figure 4.11: Measured correlated flux levels (solid black line and error bars) for AFGL 2136, in order of increasing projected baseline. The caption shows the projected baseline and position angle of the observation, as well as the slope p of the continuum fit (dashed blue line) to the red points. The solid blue line shows the best fit to the absorption spectrum (see Sec. 4.4.2).

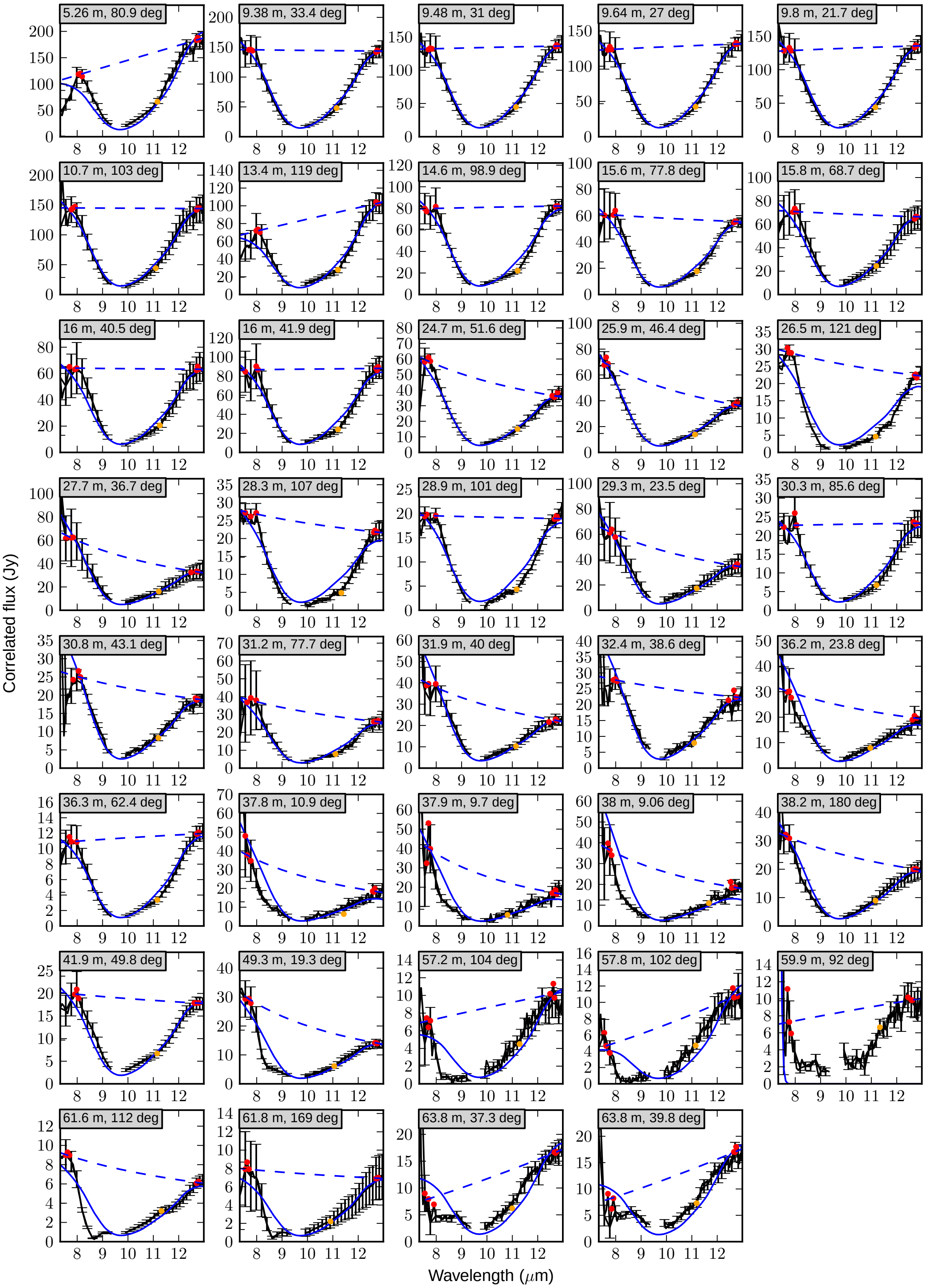

Figure 4.12: Measured correlated flux levels (solid black line and error bars) for AFGL 4176, in order of increasing projected baseline. The caption shows the projected baseline and position angle of the observation, as well as the slope p of the continuum fit (dashed blue line) to the red points. The solid blue line shows the best fit to the absorption spectrum (see Sec. 4.4.2).

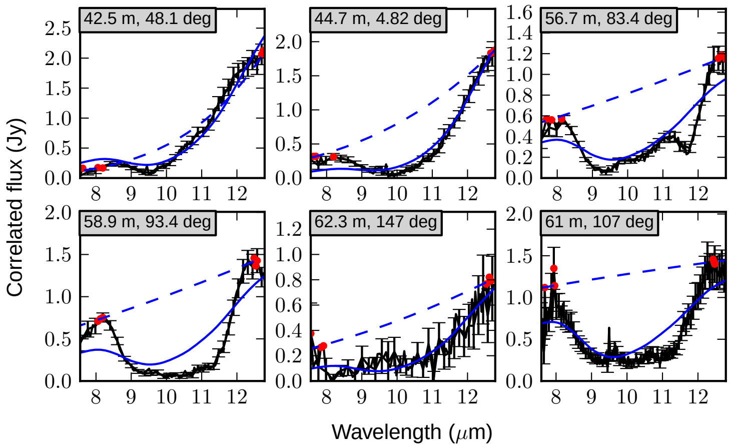

Figure 4.13: Measured correlated flux levels (solid black line and error bars) for G305.20+0.21, in order of increasing projected baseline. The caption shows the projected baseline and position angle of the observation, as well as the slope p of the continuum fit (dashed blue line) to the red points. The solid blue line shows the best fit to the absorption spectrum (see Sec. 4.4.2).

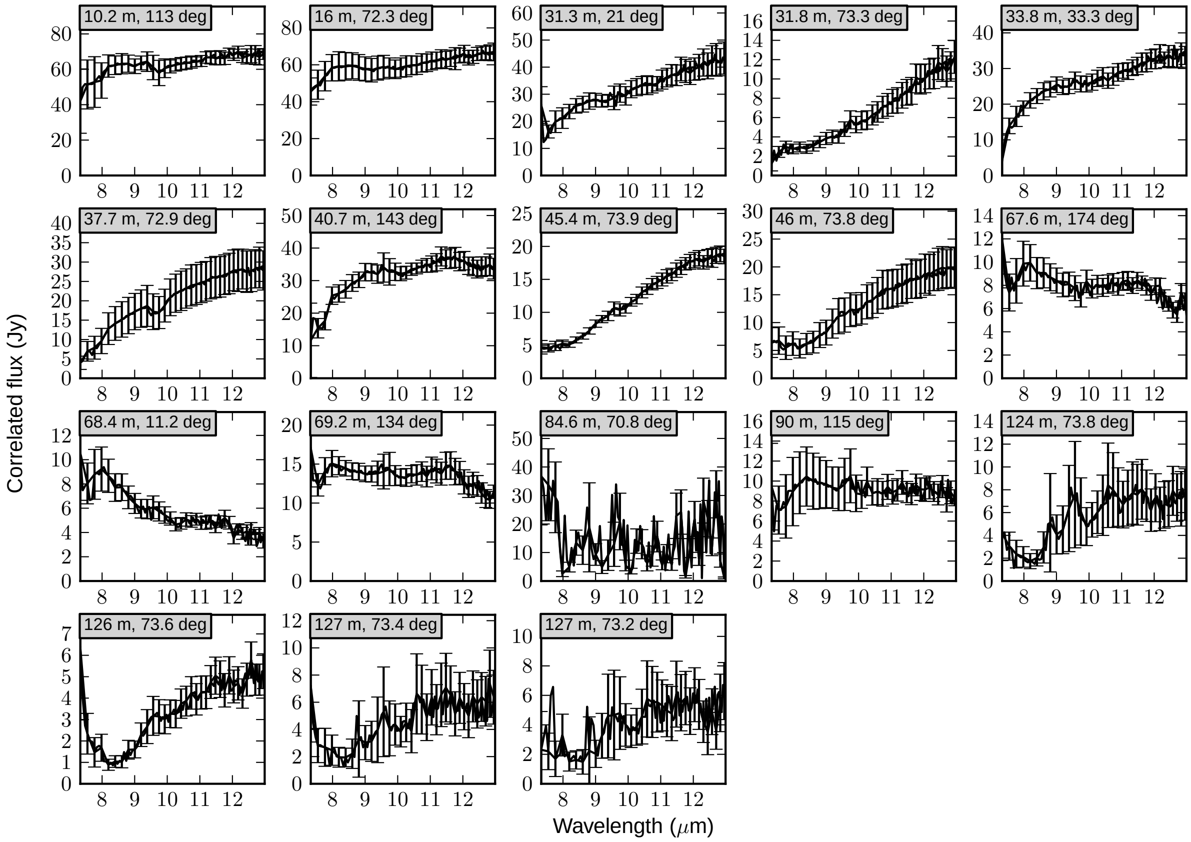

Figure 4.14: Measured correlated flux levels (solid black line and error bars) for HIP 90617, in order of increasing projected baseline. The caption shows the projected baseline and position angle of the observation.

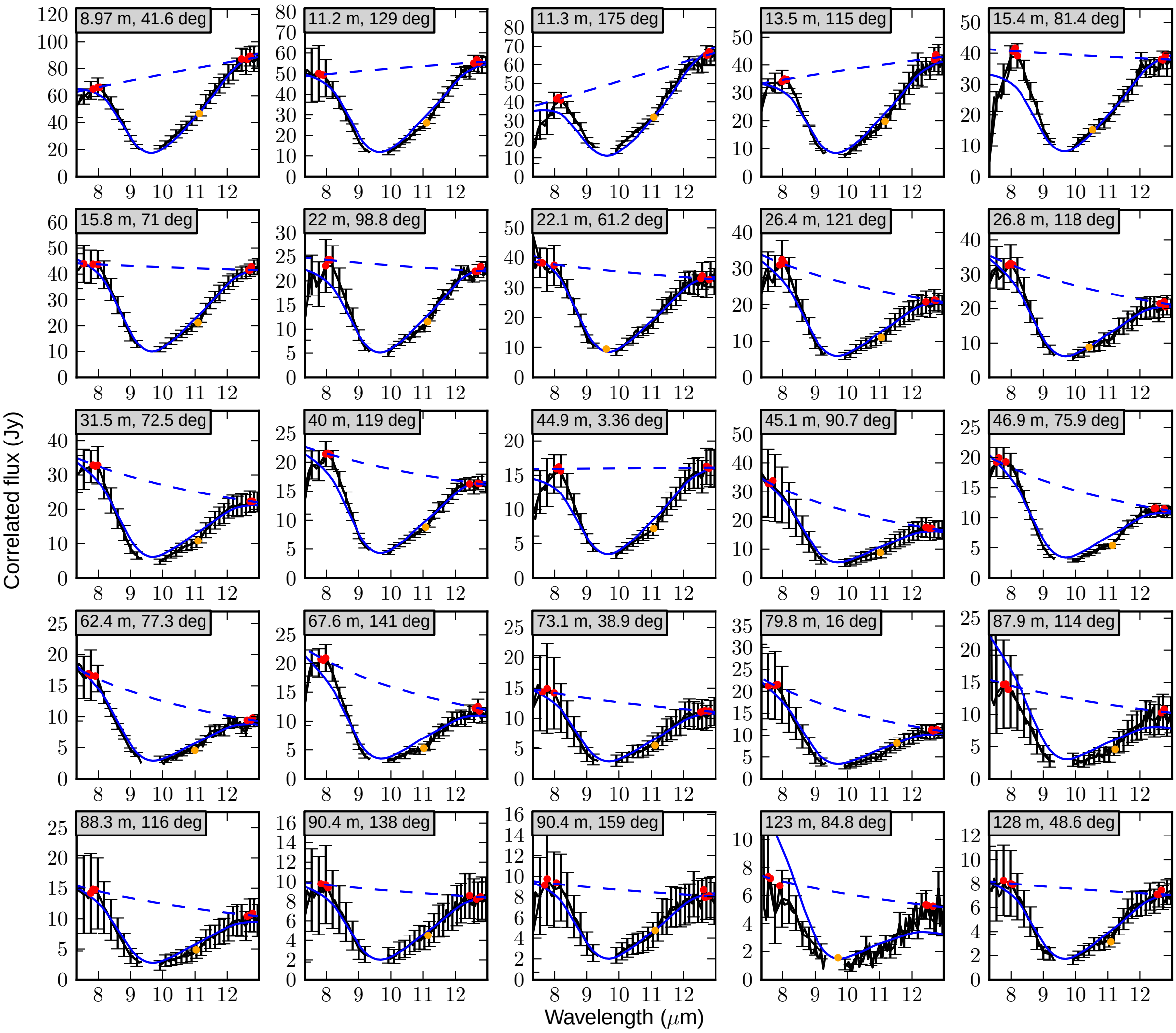

Figure 4.15: Measured correlated flux levels (solid black line and error bars) for IRAS 13481-6124, in order of increasing projected baseline. The caption shows the projected baseline and position angle of the observation, as well as the slope p of the continuum fit (dashed blue line) to the red points. The solid blue line shows the best fit to the absorption spectrum (see Sec. 4.4.2).

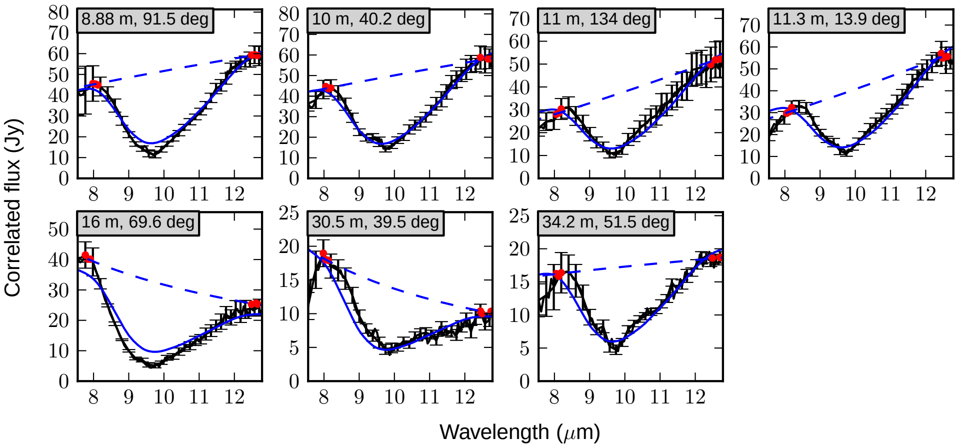

Figure 4.16: Measured correlated flux levels (solid black line and error bars) for IRAS 17216-3801, in order of increasing projected baseline. The caption shows the projected baseline and position angle of the observation, as well as the slope p of the continuum fit (dashed blue line) to the red points. The solid blue line shows the best fit to the absorption spectrum (see Sec. 4.4.2).

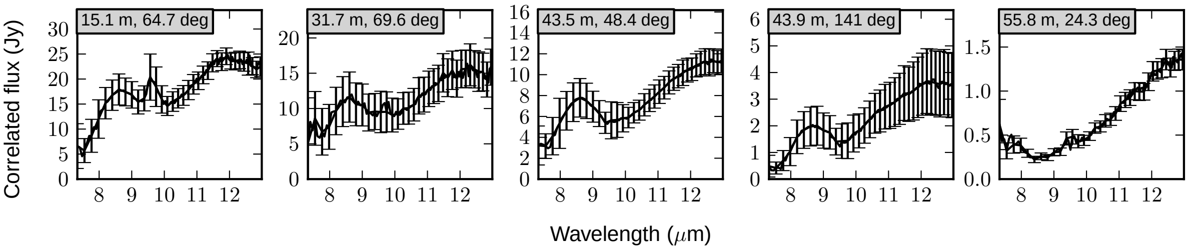

Figure 4.17: Measured correlated flux levels (solid black line and error bars) for M17 SW IRS1, in order of increasing projected baseline. The caption shows the projected baseline and position angle of the observation..

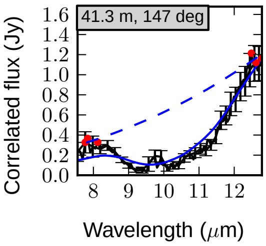

Figure 4.18: Measured correlated flux levels (solid black line and error bars) for M17 UC1, in order of increasing projected baseline. The caption shows the projected baseline and position angle of the observation, as well as the slope p of the continuum fit (dashed blue line) to the red points. The solid blue line shows the best fit to the absorption spectrum (see Sec. 4.4.2).

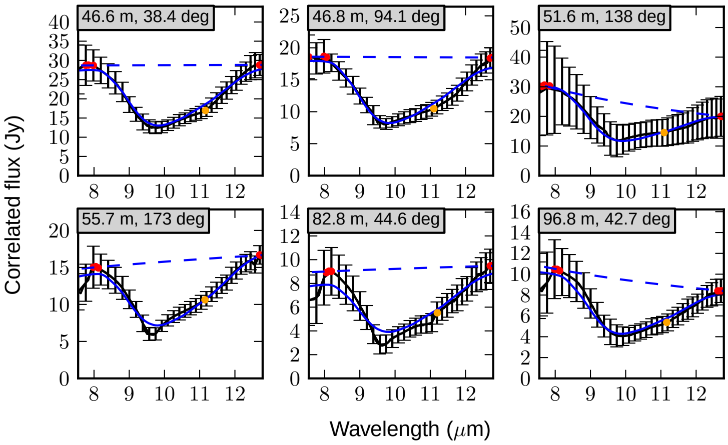

Figure 4.19: Measured correlated flux levels (solid black line and error bars) for M8E-IR, in order of increasing projected baseline. The caption shows the projected baseline and position angle of the observation, as well as the slope p of the continuum fit (dashed blue line) to the red points. The solid blue line shows the best fit to the absorption spectrum (see Sec. 4.4.2).

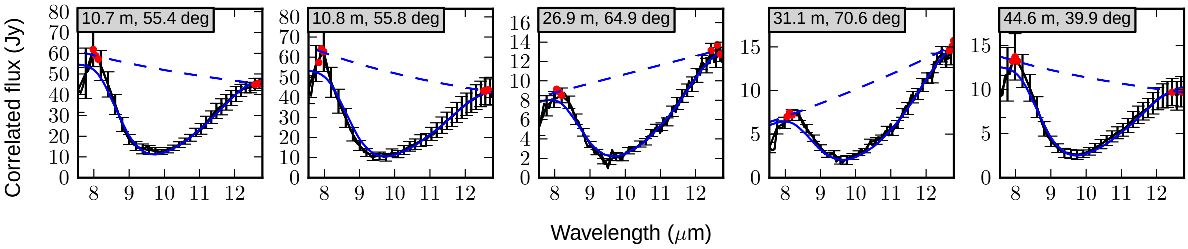

Figure 4.20: Measured correlated flux levels (solid black line and error bars) for Mon R2 IRS2, in order of increasing projected baseline. The caption shows the projected baseline and position angle of the observation, as well as the slope p of the continuum fit (dashed blue line) to the red points. The solid blue line shows the best fit to the absorption spectrum (see Sec. 4.4.2).

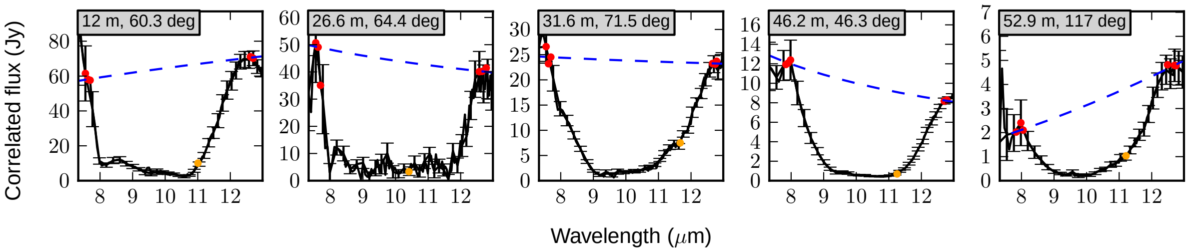

Figure 4.21: Measured correlated flux levels (solid black line and error bars) for Mon R2 IRS3 A, in order of increasing projected baseline. The caption shows the projected baseline and position angle of the observation, as well as the slope p of the continuum fit (dashed blue line) to the red points. The solid blue line shows the best fit to the absorption spectrum (see Sec. 4.4.2).

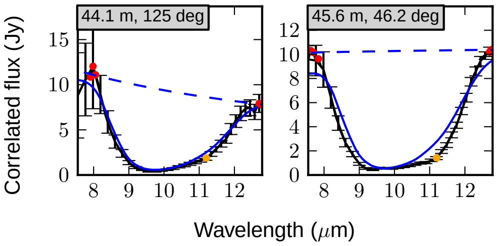

Figure 4.22: Measured correlated flux levels (solid black line and error bars) for Mon R2 IRS3 B, in order of increasing projected baseline. The caption shows the projected baseline and position angle of the observation, as well as the slope p of the continuum fit (dashed blue line) to the red points. The solid blue line shows the best fit to the absorption spectrum (see Sec. 4.4.2).

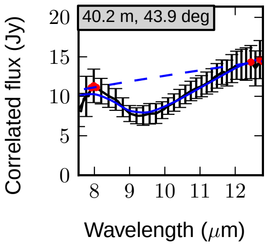

Figure 4.23: Measured correlated flux levels (solid black line and error bars) for NGC 2264 IRS1, in order of increasing projected baseline. The caption shows the projected baseline and position angle of the observation, as well as the slope p of the continuum fit (dashed blue line) to the red points. The solid blue line shows the best fit to the absorption spectrum (see Sec. 4.4.2).

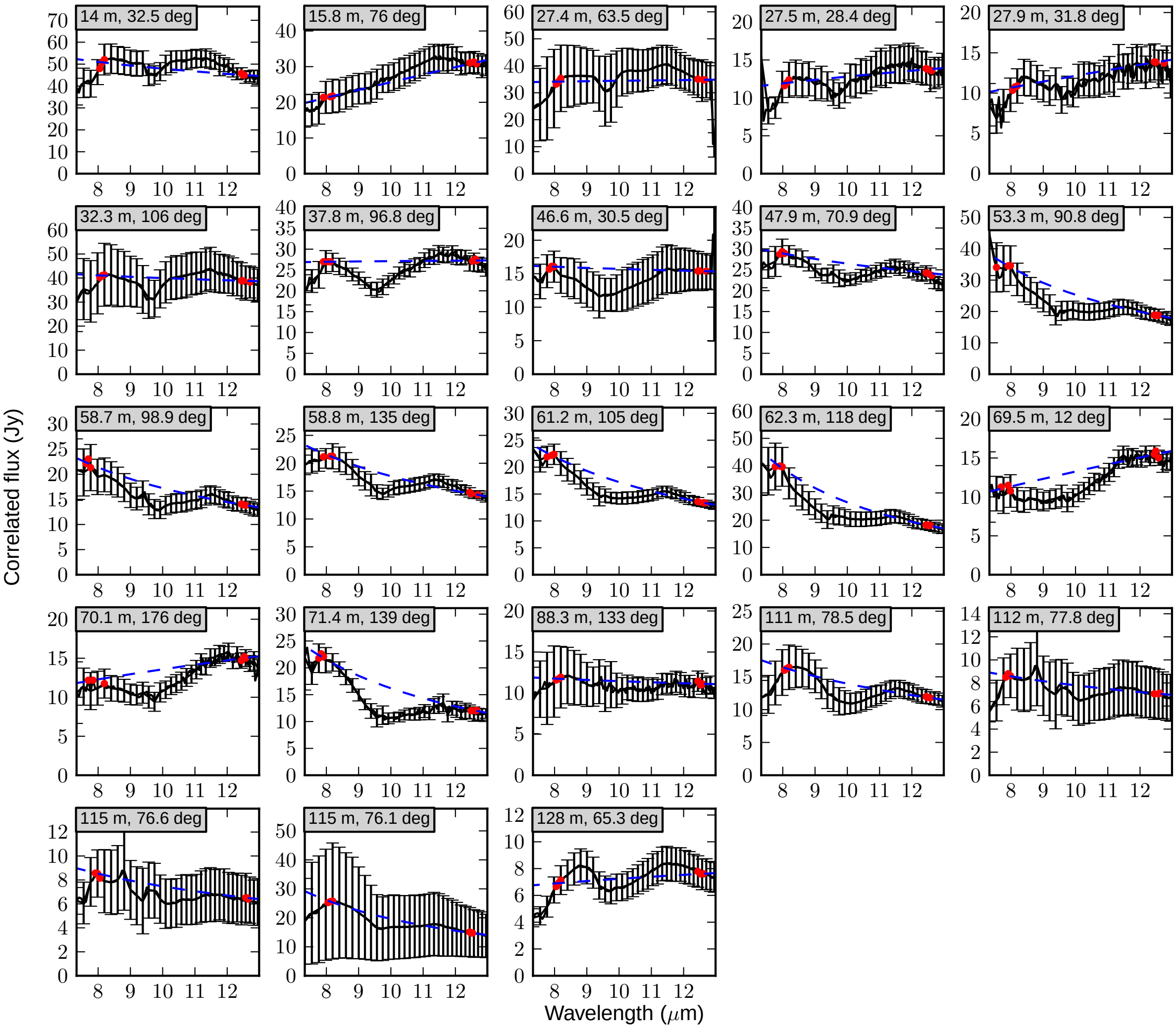

Figure 4.24: Measured correlated flux levels (solid black line and error bars) for R CrA, in order of increasing projected baseline. The caption shows the projected baseline and position angle of the observation.

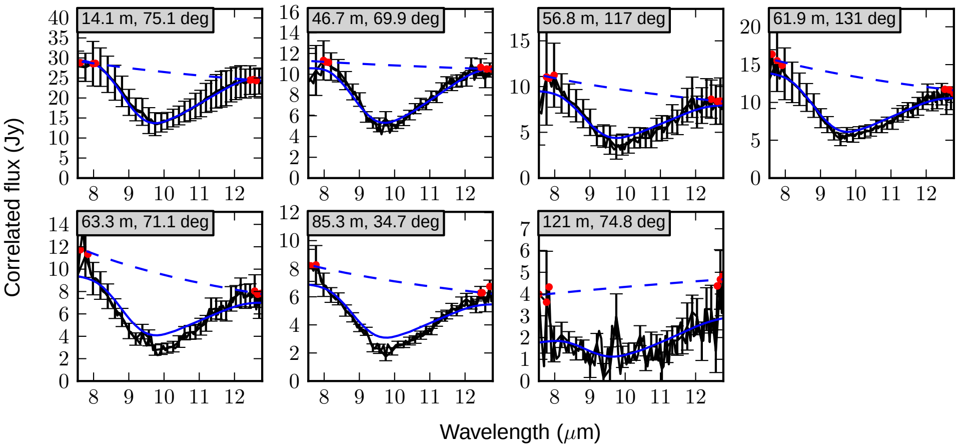

Figure 4.25: Measured correlated flux levels (solid black line and error bars) for R Mon, in order of increasing projected baseline. The caption shows the projected baseline and position angle of the observation, as well as the slope p of the continuum fit (dashed blue line) to the red points. The solid blue line shows the best fit to the absorption spectrum (see Sec. 4.4.2).

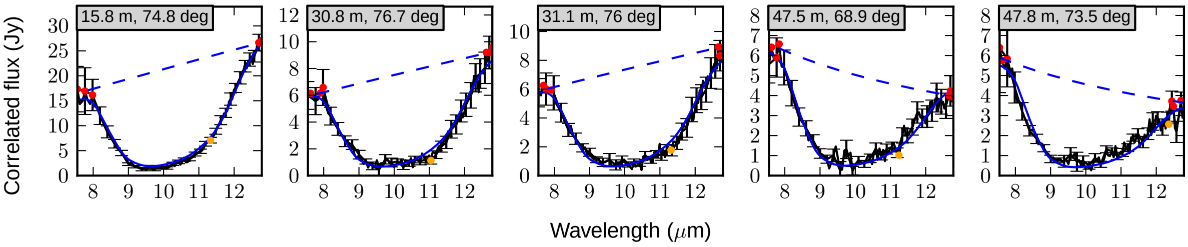

Figure 4.26: Measured correlated flux levels (solid black line and error bars) for S255 IRS3, in order of increasing projected baseline. The caption shows the projected baseline and position angle of the observation, as well as the slope p of the continuum fit (dashed blue line) to the red points. The solid blue line shows the best fit to the absorption spectrum (see Sec. 4.4.2).

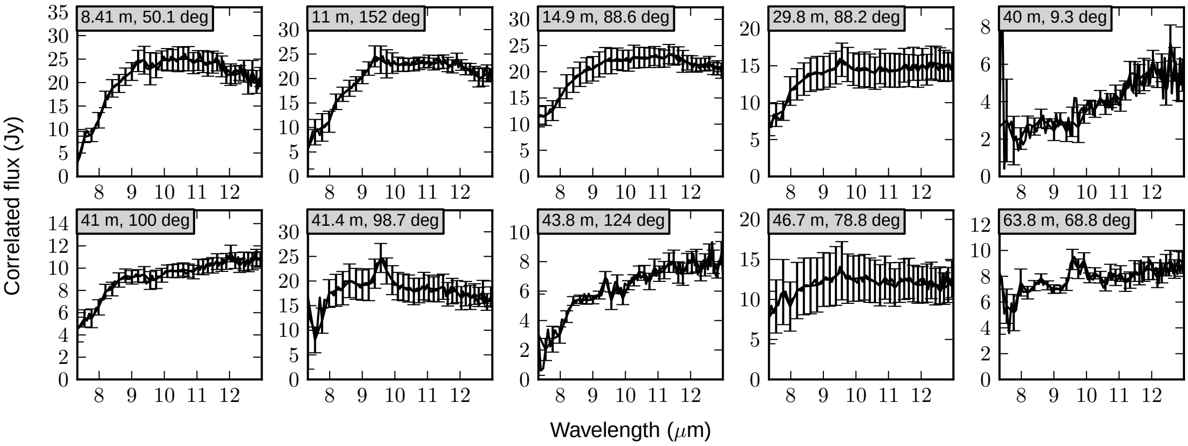

Figure 4.27: Measured correlated flux levels (solid black line and error bars) for V1028 Cen, in order of increasing projected baseline. The caption shows the projected baseline and position angle of the observation.

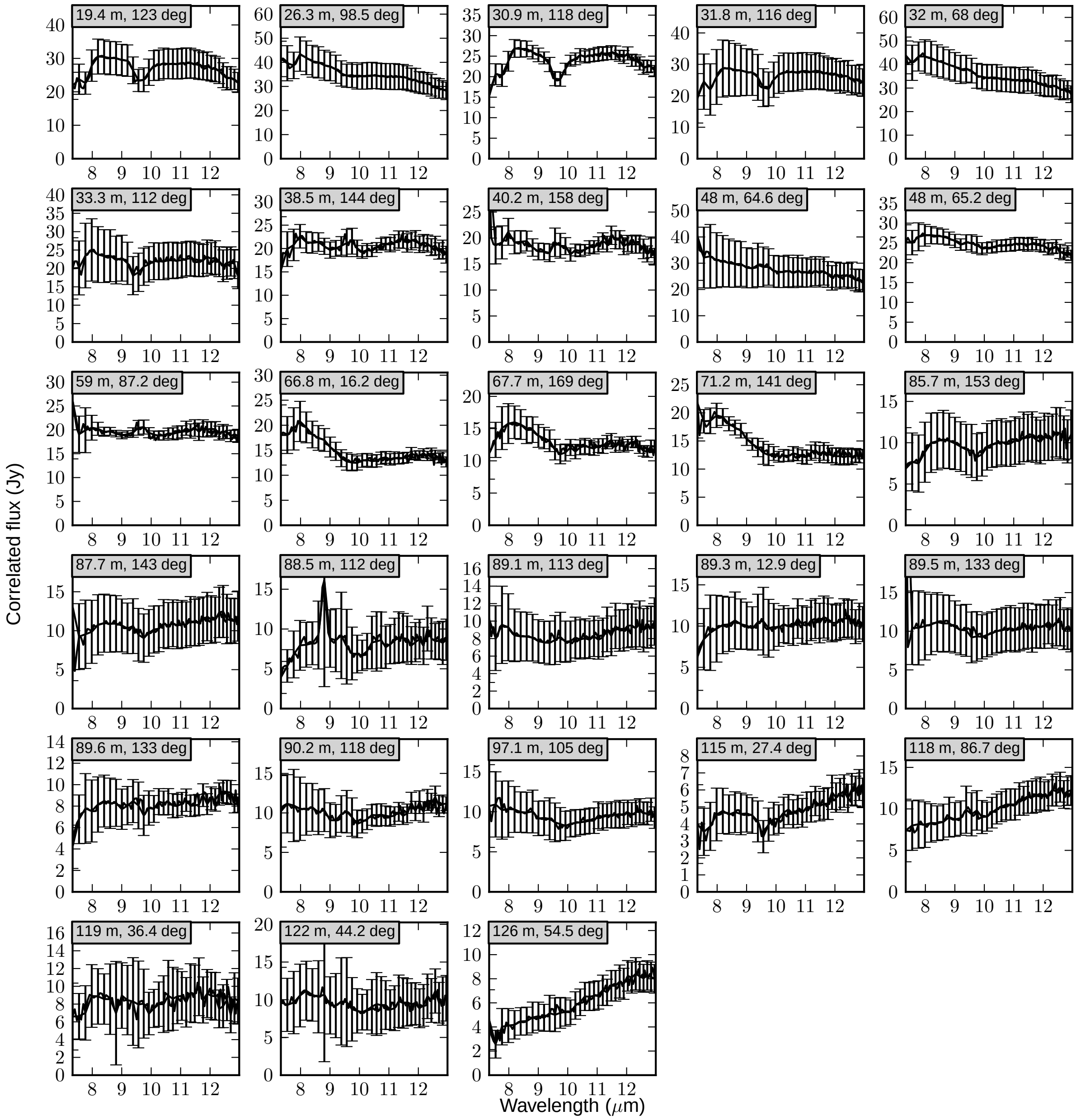

Figure 4.28: Measured correlated flux levels (solid black line and error bars) for V921 Sco, in order of increasing projected baseline. The caption shows the projected baseline and position angle of the observation.

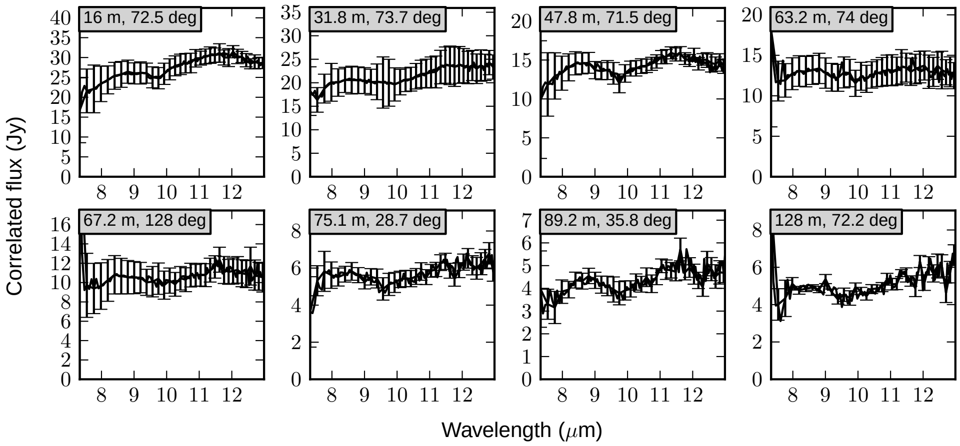

Figure 4.29: Measured correlated flux levels (solid black line and error bars) for VY Mon, in order of increasing projected baseline. The caption shows the projected baseline and position angle of the observation.

Chapter 5

An interferometric study of the massive young stellar object IRAS 13481-6124[*]

This chapter focuses on near- and mid-infrared interferometric observations of a single MYSO, IRAS 13481-6124. This object is notable for being the first truly massive star with a clear detection of a circumstellar disk (Kraus et al., 2010).

As in the previous chapter, we use relatively simple geometric model fits to the interferometric data to explore the source structure. However, thanks to the availability of extensive, multi-wavelength interferometric observations, we are able to extend this analysis to the K-band (2.2 μm) and through several narrow-band filters at mid-infrared wavelengths (8–13 μm).

We confirm that the mid-infrared interferometric observations of this MYSO are tracing the circumstellar disk detected at near-infrared wavelengths by Kraus et al. (2010). Furthermore, we derive a temperature profile for the disk of $T \propto R^{-1}$, which is much steeper than classical analytical disk models predict. To explain the steepness of this temperature profile, we speculate that the emission at both near- *and* mid-infrared wavelengths is dominated by the inner rim of the disk.

5.1 Introduction

The bright infrared source IRAS 13481-6124 was first identified as a YSO by Persson and Campbell (1987), and specifically as a massive YSO by Chan et al. (1996), based on the flux densities measured with the IRAS satellite. Kinematic distance estimates (which are typically only accurate to within about a factor of 2; Xu et al., 2006) to this object range from 3.1 to 3.8 kpc (e.g. Busfield et al., 2006; Urquhart et al., 2007), and no other distance measures are available; thus, as is often the case with such objects, the distance is poorly known. For the present study, we adopt a distance of 3.6 kpc, which Fontani et al. (2005) determined kinematically from observations of rotational transitions of CS and C^{17}O. Scaling the infrared luminosity of 1.8×10^5 L$_\odot$ determined by Beck et al. (1991) to this distance yields a luminosity of $\sim 7.7 \times 10^4$ L$_\odot$ for IRAS 13481-6124.

Observations of Hydrogen recombination lines at near-infrared wavelengths by Beck et al. (1991) showed the presence of an ionizing wind associated with IRAS 13481-6124. From the

---

[*] The material in this chapter is being prepared for publication in *Astronomy and Astrophysics* in 2013, by P. Boley, S. Kraus, R. van Boekel, W.-J. de Wit, H. Linz, T. Henning, S. Lacour, J. Monnier, B. Stecklum, P. Tuthill.

Brγ/Pfγ line ratio, these authors estimated a visual extinction of $A_V = 24$ mag, indicating the source is fairly deeply embedded. Interestingly, several searches for masers (e.g. Scalise et al., 1989; MacLeod et al., 1998), which are often found in regions of massive star formation, failed to reveal any maser emission associated with the source. Beltrán et al. (2006) mapped the continuum emission at 1.2 mm in the region, suggesting an envelope mass (gas + dust) of 1470 $\mathrm{M}_\odot$.

Mid-infrared spectropolarimetric observations by Wright et al. (2008) revealed the presence of a sharp absorption feature at 11.2 μm in the linear polarization spectrum. To date, this feature has only been observed in one other source (AFGL 2591; Aitken et al., 1988), and both Aitken et al. (1988) and Wright et al. (2008) interpret the feature as possibly arising due to the presence of crystalline olivine, which could form as a result of dust processing in the circumstellar environment. The apparent rarity of this feature, as noted by Wright et al. (2008), could indicate that IRAS 13481-6124 is currently in a very short-lived phase of the evolutionary sequence of massive star formation.

Interferometric measurements of the source at near-infrared wavelengths were performed by Kraus et al. (2010). The K-band image reconstructed from these interferometric observations shows an elongated structure, which is oriented perpendicular to an outflow component detected as a bow shock visible in Spitzer Space Telescope images from the GLIMPSE survey (Churchwell et al., 2009). Radiative transfer modeling of the spectral energy distribution (SED) and near-infrared interferometric data by Kraus et al. (2010) strongly indicate that the MYSO IRAS 13481-6124 hosts a circumstellar disk, and suggest a total luminosity of 4×10^4 $\mathrm{L}_\odot$ (i.e., about half the value derived from the IRAS measurements by Beck et al., 1991).

Most recently, K-band integral-field spectroscopic measurements by Stecklum et al. (2012) showed a photocenter shift of ~ 1 AU in the Brγ line along the same position angle as the bow shock reported by Kraus et al. (2010), which confirms the association of the parsec-scale outflow with the MYSO. Furthermore, these integral-field measurements also show evidence for (possibly non-Keplerian) rotation along the disk axis, providing yet another indication of a circumstellar disk in this system. To date, no other MYSO has shown such clear evidence for the presence of a disk.

In this chapter, we consider the K-band interferometric measurements presented by Kraus et al. (2010) together with new interferometric measurements taken in the N-band. We use geometric models of the near-/mid-infrared interferometric observations, and probe the source on spatial scales (given by $\sim \lambda/2B$, where λ is the wavelength, and B is the projected baseline of the interferometric observations) of about 10–1000 AU. We focus on the wavelength behavior of the fits, which we examine in the context of the temperature profile of the circumstellar disk.

5.2 Observations

5.2.1 Long-baseline interferometry with VLTI

Observations of IRAS 13481-6124 were conducted in the N band (8–13 μm) using the two-telescope mid-infrared interferometric instrument MIDI at the VLTI in 2009–2012. In this work, we make use of the 25 MIDI observations presented as part of the VLTI/MIDI MYSO Survey (Chapter 4). We also present an additional 15 MIDI measurements of the source, which were obtained as part of program 086.C-0543 (PI S. Kraus), and one measurement obtained as part of program 384.C-0625 (PI W.-J. de Wit). We summarize the entire MIDI data set of 41 visibility measurements for this source in Table 5.1, and show the locations of the measurements in uv space as black points in the right panel of Fig. 5.1. These data were processed in an identical fashion as the observations taken as part of the VLTI/MIDI MYSO Survey, and we refer to

Table 5.1: MIDI observations of IRAS 13481-6124

Date/time (UTC)	Telescopes	Proj. baseline (m)	Position angle (deg.)	Avg. visibility
2009-02-15 04:55†	UT2-UT3	44.9	3.4	0.14
2009-05-02 04:04†	D0-H0	62.4	77.3	0.11
2009-05-03 04:58†	D0-G1	67.6	141.1	0.13
2009-07-02 00:41†	G1-K0	73.1	38.9	0.11
2009-07-04 00:58†	E0-H0	45.1	90.7	0.21
2009-07-04 23:23†	E0-G0	15.8	71.0	0.39
2009-07-05 23:43†	E0-H0	46.9	75.9	0.13
2009-07-06 02:49†	E0-H0	40.0	118.7	0.17
2009-07-06 23:23†	G0-H0	31.5	72.5	0.23
2009-07-07 02:42†	G0-H0	26.8	117.9	0.23
2009-07-07 02:53†	G0-H0	26.4	120.7	0.22
2010-02-14 08:39	E0-G0	15.8	71.0	0.42
2010-05-04 01:45†	A0-K0	128.0	48.6	0.07
2010-05-04 04:32†	A0-K0	122.5	84.8	0.06
2010-05-05 02:03†	G1-K0	79.8	16.0	0.13
2010-05-05 03:54†	A0-G1	87.9	114.1	0.11
2010-05-05 04:06†	A0-G1	88.3	116.4	0.10
2010-05-05 05:49†	A0-G1	90.4	138.2	0.08
2010-05-05 07:24†	A0-G1	90.4	159.3	0.08
2011-03-11 03:55	G1-I1	44.8	9.4	0.20
2011-03-11 04:06	G1-I1	44.7	11.5	0.20
2011-03-11 05:28	G1-H0	57.8	174.7	0.15
2011-03-11 07:49	D0-I1	82.3	104.8	0.09
2011-03-11 08:28	H0-I1	36.3	155.2	0.21
2011-03-13 05:51	G1-K0	79.3	19.0	0.13
2011-03-31 04:52	D0-I1	79.9	83.2	0.09
2011-03-31 06:16	D0-I1	82.1	101.5	0.08
2011-05-03 05:44	G1-I1	36.4	66.9	0.22
2012-02-24 06:42	D0-I1	78.5	76.6	0.12
2012-03-29 02:53	A1-I1	102.4	41.3	0.14
2012-03-29 03:03	A1-I1	102.8	43.6	0.12
2012-04-01 07:00	A1-I1	104.5	100.1	0.09
2012-04-01 09:02	G1-K0	59.7	60.2	0.18
2012-04-01 09:11	G1-K0	58.6	61.6	0.18
2012-05-01 05:01†	B2-C1	9.0	41.6	0.71
2012-05-01 07:10†	B2-D0	22.1	61.2	0.33
2012-05-02 05:15†	A1-B2	11.2	128.9	0.46
2012-05-02 06:50†	A1-C1	13.5	115.3	0.33
2012-05-02 07:50†	A1-D0	22.0	98.8	0.20
2012-05-02 08:40†	A1-B2	11.3	174.5	0.49
2012-05-02 09:08†	B2-D0	15.4	81.4	0.33

Notes. Observations marked with a † symbol were presented as part of the VLTI/MIDI MYSO Survey (Chapter 4).

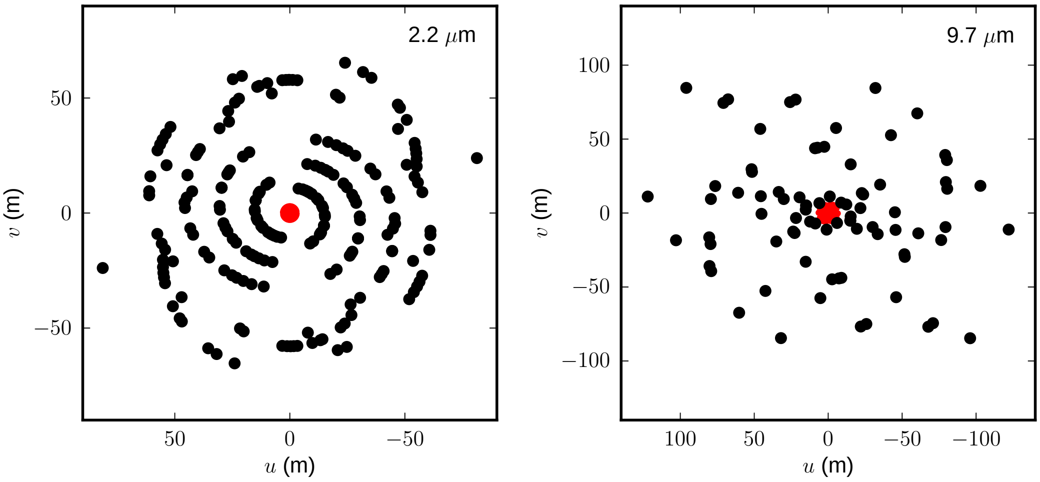

Figure 5.1: uv coverage of the interferometric measurements. The left panel shows the coverage of the near-infrared measurements, while the right panel shows the coverage of the mid-infrared measurements. Black points show the long-baseline VLTI observations (AMBER and MIDI), while the speckle-interferometry and aperture-masking observations (NTT and GSO/T-ReCS) are shown in red.

Sec. 4.3.1 of this thesis for further details.

5.2.2 Aperture-masking interferometry with GSO

Observations of IRAS 13481-6124 were also performed using the aperture-masking technique with the Thermal-Region Camera Spectrograph (T-ReCS; De Buizer and Fisher, 2005) at the Gemini South Observatory (GSO). This single-telescope technique works by blocking the aperture with a mask with small holes in it, thus transforming the single large aperture into a series of smaller ones. The resulting interference patterns represent the coherence function, thus their Fourier transform is equal to the visibility. For more details on this technique, we refer to PhD thesis of Monnier (1999) and the textbook by Labeyrie et al. (2006); as an example of a recent application of the technique, we note the work by Vehoff et al. (2010), who used T-ReCS observations similar to those presented here to reconstruct a diffraction-limited image at a wavelength of 11.7 μm of the MYSO NGC 3603 IRS 9A.

The aperture-masking interferometry observations of IRAS 13481-6124 were performed at N-band wavelengths on May 7, 2007 (program ID GS-2007A-Q-38, PI J. Monnier). Two exposures of 131 s each were performed in the five narrow-band filters Si1, Si2, Si3, Si5 and Si6, which have widths of $\sim$ 0.7–1.2 μm and central wavelengths of 7.7, 8.7, 9.7, 11.7 and 12.4 μm, respectively. The aperture-masking observations presented here measure the visibility amplitude with projected baselines of 1.8–6.4 m; we show this coverage in the uv plane as red points in the right panel of Fig. 5.1.

5.2.3 Previously-published K-band observations

IRAS 13481-6124 was observed in the K band with the three-telescope interferometric instrument AMBER at the VLTI in 2008–2009 (program IDs 081.C-0272, 083.C-0236, PI G. Weigelt; 083.C-0621, PI S. Kraus), and speckle-interferometry observations were made with the 3.6 m

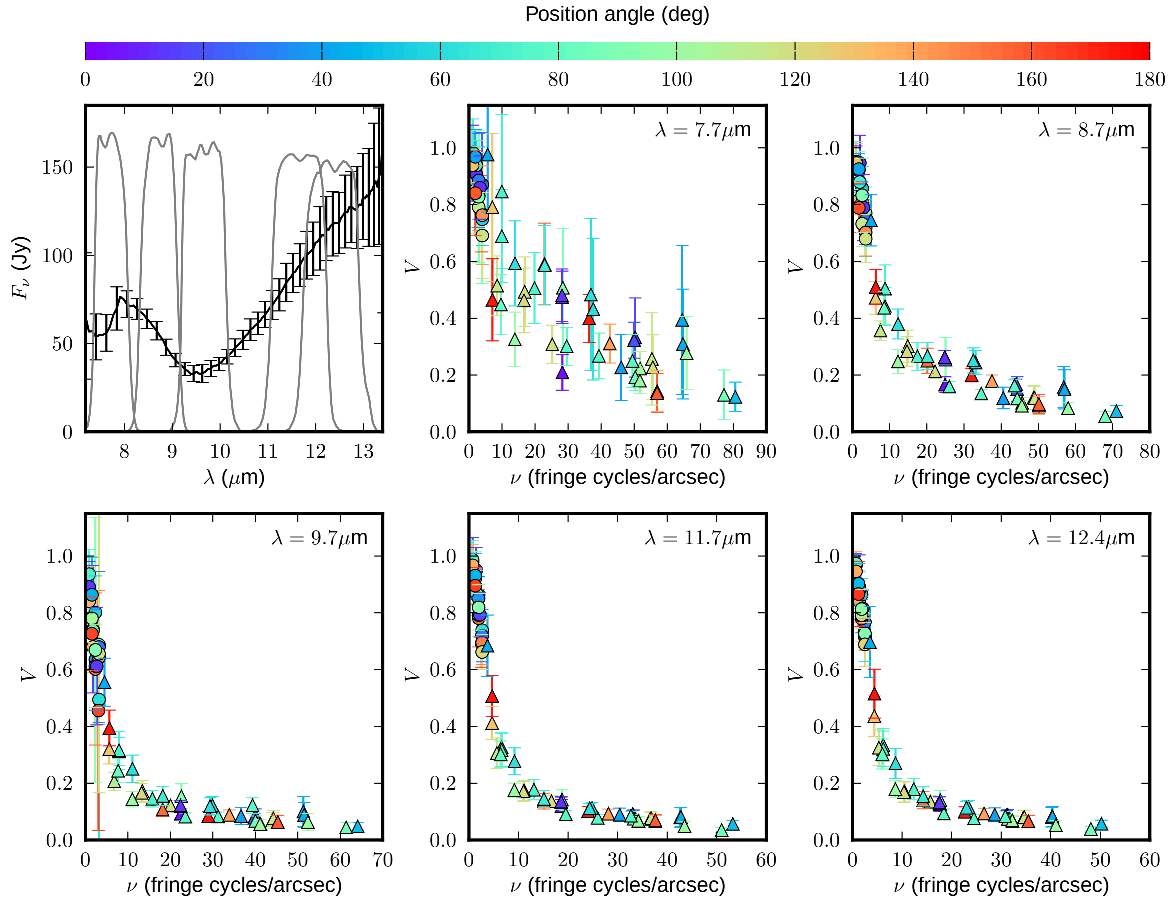

Figure 5.2: *Top left panel:* Total N-band spectrum observed with MIDI (black) and the transmission curves for the five filters used for the T-ReCS aperture-masking measurements. *Remaining panels:* The visibility amplitude V as a function of spatial frequency ν in each of the five filters. The T-ReCS measurements are shown as circles, while the MIDI measurements, averaged over each corresponding filter, are shown as triangles. The color of each data point shows the position angle (measured East of North).

ESO New Technology Telescope (NTT) on February 3, 2009 (program ID 082.C-0223, PI S. Kraus). These data were presented by Kraus et al. (2010), and we refer to that publication for further details about the observations and data reduction, however we reiterate the most relevant characteristics of the data here.

The projected baselines of the AMBER measurements range from 11 to 85 m, while the NTT bispeckle measurements provide projected baselines up to ~ 3 m. The AMBER data consist of spectrally-resolved visibility amplitudes and closure phases across the K band (1.95–2.55 μm) with a spectral resolution $\lambda/\Delta\lambda \approx 35$, while the NTT bispeckle data consist of just visibility amplitudes at the center of the K band (2.2 μm). We show the uv coverage in the left panel of Fig. 5.1, where the VLTI/AMBER measurements are shown in black, and the NTT bispeckle data are shown in red.

5.3 Results

The results of the MIDI and T-ReCS observations are shown in Fig. 5.2. In the top left panel, as a black line, we show the total N-band spectrum of the source, measured with MIDI on the 8.2 m UT telescopes. The transmission curves of the five filters used for the T-ReCS observations are overlaid in gray; the spectrally-resolved MIDI visibilities were multiplied by these normalized filter curves to create values which are directly comparable to the T-ReCS measurements. The remaining five panels of Fig. 5.2 show the visibility amplitude V as a function of spatial frequency $\nu = B/\lambda$ in each of the five filters, where the T-ReCS data are shown as circles, and the MIDI data are shown as triangles; the color of each data point shows the position angle (measured East of North) of the measurement.

First, we note that the transition from the visibilities measured with MIDI to those measured with T-ReCS is smooth and continuous. This confirms that the absolute calibration between these two very different techniques and instruments is consistent, and that the long-baseline observations are directly comparable to those obtained with the aperture-masking technique.

Second, the dependence of the visibility on baseline and wavelength shows that the infrared emission can be approximately described by two components. An extended component causes the visibility to drop quickly at short baselines (spatial frequencies $\lesssim$10 cycles/arcsec). A compact component then makes the visibility curve flatten off, and decrease more slowly towards longer baselines. The spatial frequency at which the visibility curve flattens is a measure of the size of the extended component, and the visibility amplitude at this point equals the fraction of the total flux that is contributed by the compact component, f_{compact}. In Fig. 5.3 one can see that f_{compact} is strongly wavelength-dependent, first decreasing from ~80% at 2.2 micron, to ~45% at 7.7 micron, ~25% at 8.7 micron, and ~15% at 9.7 micron, then remaining approximately constant between 9.7 and 12.4 micron.

This is strongly reminiscent of the behavior seen in models of Herbig Ae star disks (e.g van Boekel et al., 2005). The relative flux contribution of the compact, hot component steeply decreasing between ~7.5 and ~10 micron and then remaining approximately constant between ~10 and ~12.5 micron is due to combination of two effects: (1) towards longer wavelengths the contribution of cooler material, located further from the star, increases with wavelength; (2) the strong increase in dust opacity in the silicate feature leads to stronger emission from the disk surface layers. For a more detailed discussion, we refer to the work by van Boekel et al. (2005).

5.4 Analysis

As noted in Sec. 5.3, the observed visibilities of IRAS 13481-6124 show evidence for two distinct components. Kraus et al. (2010) examined the K-band AMBER/NTT visibilities in terms of several types of two-component geometric models, all of which included an extended, one-dimensional Gaussian halo as one component; the second (two-dimensional) component was either a uniform disk, a thin ring, a compact Gaussian, or a disk model with a parameterized temperature distribution.

As the Gaussian model provides good fits to the near-infrared data, has fewer parameters than the parameterized disk model, and is conceptually very simple, we choose to focus on this type of model to examine the entirety of the interferometric data. Specifically, we fit the "2D1D" model from Chapter 4 to each wavelength separately; this model consists of a two-dimensional Gaussian (width $\mathrm{FWHM}_{\mathrm{2D}}$, position angle ϕ and inclination angle θ) and a one-dimensional Gaussian (width $\mathrm{FWHM}_{\mathrm{1D}}$), both centered at the origin. The flux ratio between these two components is given by $F_{\mathrm{2D}}/F_{\mathrm{1D}}$. The best-fit parameters were derived with a grid search followed by a downhill-simplex minimization of χ^2; uncertainties in the best-fit values were derived using the same Monte-Carlo approach described in Sec. 4.4.1 of this thesis.

We tabulate the results of this fitting procedure for each wavelength in Table 5.2, and show the observed and model visibilities in Fig. 5.3. The two-dimensional parameters derived from the 2.2 μm data are essentially identical to those derived by Kraus et al. (2010) for the same data set. However, in contrast to the present work, the one-dimensional Gaussian component in their model was not a free parameter, and has a fixed width of 108 mas (compared with a width of 77 mas found here).

The additional *mid*-infrared interferometric observations presented in this chapter allow the geometry of IRAS 13481-6124 at this wavelengths to be constrained much better than was previously possible (Chapter 4). The orientation derived from the mid-infrared data matches that derived from the near-infrared observations to within ~ 10–20°, which Kraus et al. (2010) showed to be tracing a circumstellar disk. Thus, for this particular MYSO, the mid-infrared emission is clearly dominated by a disk component[1].

5.5 Discussion

The parameters of the model fits show a clear dependence on wavelength. We plot the derived values of the flux ratio of the two Gaussian components, their widths, and inclination angle in Fig. 5.4: the flux ratio $F_{\rm 2D}/F_{\rm 1D}$ decreases with wavelength, while the FWHM sizes of both Gaussians increase with wavelength. There is some indication that θ is decreasing with wavelength (indicating the level of asymmetry may be decreasing at longer wavelengths), albeit with relatively large error bars.

As it seems that the two-dimensional Gaussian component is tracing disk emission, it can be useful to consider the expected apparent "size" of a circumstellar disk as a function of wavelength. In both analytic approximations and more elaborate numerical models of circumstellar disks, the resulting disk temperature profile can often be parameterized as a power law depending on radius,

$$T(R) \propto R^{\alpha}, \tag{5.1}$$

where the value of α depends on the type of disk[2].

Furthermore, as a first approximation, the apparent size $R_c(\lambda)$ of the disk at a given wavelength can be defined as the radius at which the disk temperature, given by Eq. (5.1), is equal to a temperature $T_c(\lambda)$, the wavelength dependence of which is given by the Wien displacement law, i.e.:

$$T_c(\lambda) \propto \frac{1}{\lambda}. \tag{5.2}$$

Thus, by combining Eqs. (5.1) and (5.2), we can derive a relation for the expected wavelength dependence of the apparent size of a disk with a parameterized temperature profile:

$$R_c(\lambda) \propto \lambda^{-1/\alpha}. \tag{5.3}$$

The wavelength dependence of the size derived from our Gaussian fits is very well described by a linear function ($\alpha = -1$), shown as a dashed line in Fig. 5.4. This implies a disk temperature profile in IRAS 13481-6124 of $T \propto R^{-1}$, which is much steeper than can be explained by an optically-thin disk ($\alpha = -1/2$), or even a disk dominated by accretion luminosity ($\alpha = -3/4$).

---

[1] N.B., this is not always the case. See the discussion of individual sources in the VLTI/MIDI MYSO Survey in Sec. 4.5.4.

[2] For example, a value of $\alpha = -1/2$ corresponds to an optically thin disk. $\alpha = -3/4$ corresponds to either an optically thick, geometrically thin disk, or a disk dominated by accretion luminosity. An optically thick, flared disk has $\alpha = -3/7$. For more details, see *Accretion processes in star formation* by Hartmann (2009).

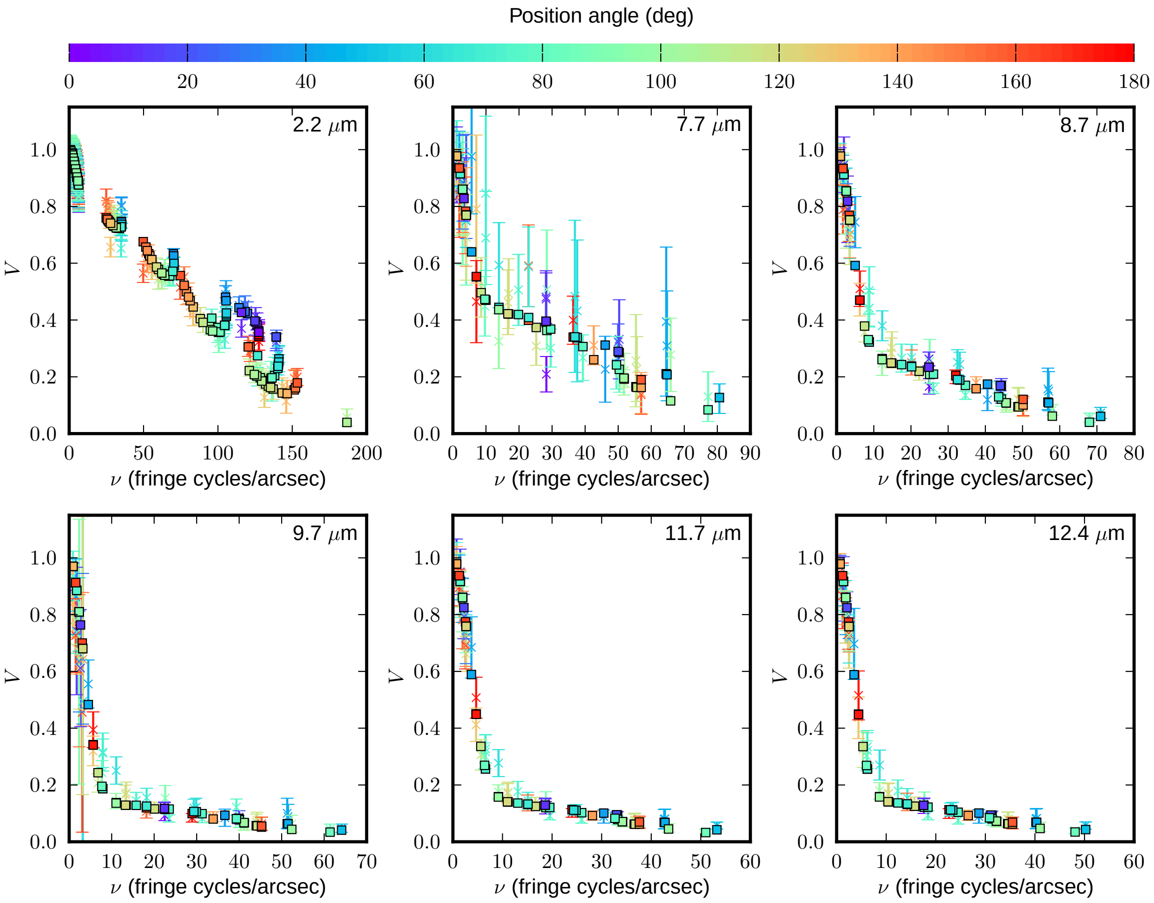

Figure 5.3: Geometric model fits to the visibilities at each wavelength. See Table 5.2 for the fit parameters. Crosses and error bars mark the observed visibility levels; squares mark the model values. As in Fig. 5.2, the color of each point indicates the position angle of the measurement.

Table 5.2: Geometric model fit parameters

Wavelength (μm)	F_{2D}/F_{1D}	FWHM$_{2D}$ (mas)	FWHM$_{1D}$ (mas)	ϕ (deg)	θ (deg)
2.2	3.75 ± 0.16	4.93 ± 0.062	76.8 ± 3.1	$112. \pm 1.7$	45.0 ± 1.2
7.7	0.864 ± 0.13	9.75 ± 0.99	$98.1 \pm 15.$	$120. \pm 22.$	42.7 ± 9.8
8.7	0.375 ± 0.029	11.2 ± 0.66	96.3 ± 5.8	$108. \pm 10.$	42.0 ± 6.1
9.7	0.162 ± 0.015	11.7 ± 1.3	$113. \pm 7.7$	$135. \pm 27.$	38.5 ± 9.5
11.7	0.175 ± 0.014	13.5 ± 1.0	$115. \pm 5.4$	$116. \pm 19.$	37.6 ± 8.2
12.4	0.176 ± 0.016	14.2 ± 1.2	$122. \pm 5.9$	$120. \pm 27.$	36.1 ± 8.9

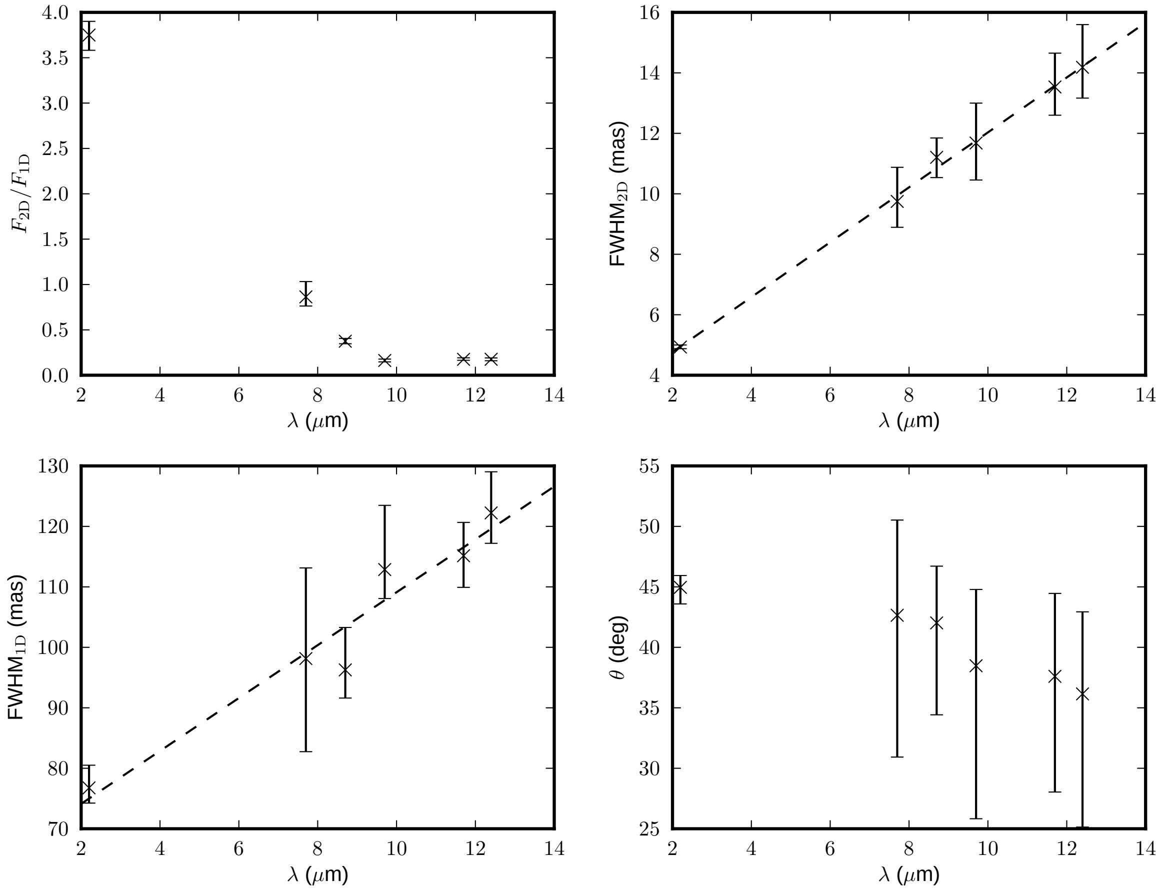

Figure 5.4: Best-fit values of the flux ratio F_{2D}/F_{1D}, the width of the two- and one-dimensional Gaussians FWHM$_{2D}$ and FWHM$_{1D}$, and the inclination angle θ as a function of wavelength. The dashed lines show linear fits to the Gaussian widths.

One possible explanation for this steeper-than-expected temperature profile is that the inner rim of the circumstellar disk, which may be "puffed up" (e.g. Dullemond et al., 2001), contributes strongly (or even dominantly) to the emission, even in the 8–13 μm range. Such a puffed-up inner rim is a natural result of direct irradiation of the inner edge of the disk by the central star, and it could be responsible for a substantial fraction of the emission and near- and mid-infrared wavelengths. To explore this possibility in the present context, we consider here the effective height of the inner rim (i.e., at the dust evaporation radius) of a circumstellar disk as a function of the mass of the central star.

We show a schematic of the system geometry in Fig. 5.5. The inner rim is located at a distance $R_{\rm rim}$ from the star, has a height $H_{\rm rim}$ and a temperature $T_{\rm rim}$ (assumed to be 1500 K, i.e. the evaporation temperature of silicate dust). For a passively-heated disk, Eqs. (12)–(14) from the work by Dullemond et al. (2001) allow the radius and height of the inner rim to be expressed as

$$R_{\rm rim} = \left(\frac{L_\star}{4\pi\sigma T_{\rm rim}^4}\right)^{1/2} \left(1 + \frac{H_{\rm rim}}{R_{\rm rim}}\right)^{1/2}, \tag{5.4}$$

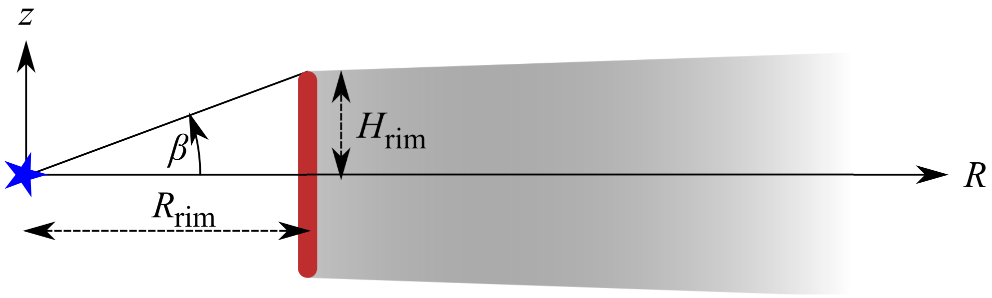

Figure 5.5: Schematic of the inner rim of a circumstellar disk. The inner rim (shown in red) occurs at a radius of $R_{\rm rim}$ from the central star (shown in blue), equal to the dust evaporation radius. The effective height of the inner rim is given by $H_{\rm rim}$, and the angle subtended by the rim (as viewed from the star) is 2β. Not to scale.

and

$$H_{\rm rim} = \chi_{\rm rim}\sqrt{\frac{kT_{\rm rim}R_{\rm rim}^3}{\mu m_p G M_\star}}, \tag{5.5}$$

where $L_\star$ and $M_\star$ are the luminosity and mass of the central star, $\chi_{\rm rim}$ is the ratio of the effective height to the pressure scale height of the rim, μ is the mean molecular weight (2.3 for a gas consisting H_2 and He, with mass abundances of 75% H and 25% He), and m_p is the proton mass. Eqs. (5.4) and (5.5) can be solved iteratively, until a solution for both the radius and height of the inner rim is found.

In order to examine the behavior of these quantities as a function of mass, we use the values of $\chi_{\rm rim}$ tabulated by Dullemond et al. (2001) for zero-age main-sequence stars, where we have linearly extrapolated their table for masses higher than 8 $M_\odot$ (corresponding to a B2/B3 star). Furthermore, for the sake of simplicity, we adopt a power-law relationship for the stellar mass and luminosity,

$$L_\star = L_\odot\left(\frac{M_\star}{M_\odot}\right)^4. \tag{5.6}$$

Finally, we quantify the role played by the inner rim in terms of the fractional coverage $F_{\rm rim}$ of the sphere around the star by the inner rim:

$$F_{\rm rim} = \frac{1}{4\pi}\int_0^{2\pi}\int_{-\beta}^{+\beta}\cos\theta\,{\rm d}\theta\,{\rm d}\phi = \sin\beta, \tag{5.7}$$

where the angle β is related to $H_{\rm rim}$ and $R_{\rm rim}$ by $\tan\beta = H_{\rm rim}/R_{\rm rim}$ (see Fig. 5.5). To first order (i.e., if we neglect the effects of scattering), $F_{\rm rim}$ is equivalent to the fraction of the total stellar energy output which will be directly absorbed by the rim.

We show $F_{\rm rim}$ as a function of stellar mass in Fig. 5.6, computed for masses of 2, 4, 8, 16 and 32 $M_\odot$. It can be seen that for a star with a mass of 8 $M_\odot$, the fractional coverage is already 30%. This means that the inner rim quickly becomes more important for higher-mass stars, and may play a critical role in the disk temperature profile: the large amount of stellar energy absorbed by the inner rim must be reradiated at longer (infrared) wavelengths, and most of this reradiation will occur at (or very near to) the inner rim itself. Furthermore, the inner rim may also be responsible for shielding ("shadowing") large parts of the disk from direct irradiation by the central star (this mechanism was used to explain the observed SEDs and small mid-infrared sizes of the Herbig Ae stars HD 101412 and HD 135344 B; Fedele et al., 2008), which could also tend to steepen the temperature profile.

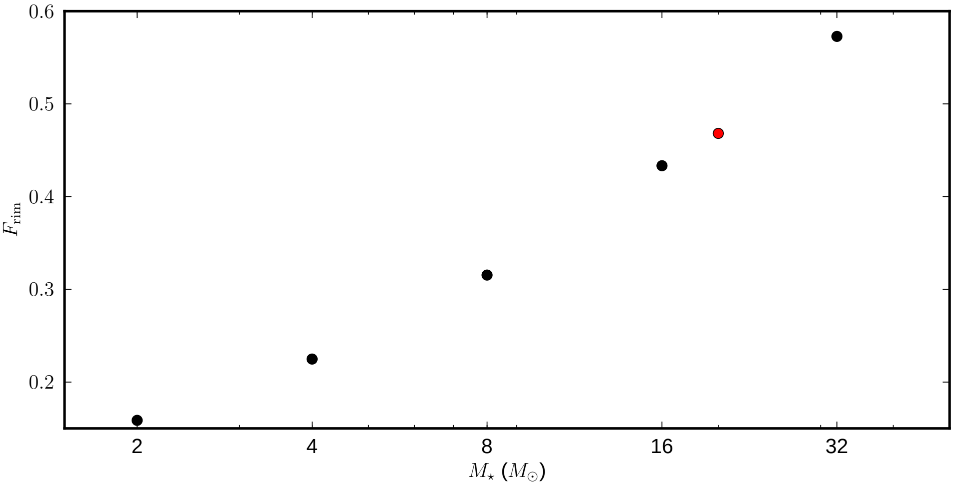

Figure 5.6: Fraction of the sphere around a star covered by the inner rim as a function of stellar mass.

As noted in the introduction, luminosity estimates for IRAS 13481-6124 are about 4–8×10^4 $L_\odot$. Depending on the mass-luminosity scaling relation used, this corresponds to a star with a mass of $\sim$ 15–20 $M_\odot$. For a $\sim$ 20 $M_\odot$ star (shown as a red point in Fig. 5.6), a full 47% of the sphere around the central star is covered by the inner rim, meaning nearly *half* of the entire energy output by the star is directly absorbed by the disk.

5.6 Summary and conclusions

In this work, we presented new high-resolution, mid-infrared interferometric observations of the massive young stellar object IRAS 13481-6124. These observations include long-baseline interferometric visibilities measured in the N band with the MIDI instrument on the Very Large Telescope Interferometer with projected baselines of up to 128 m, and also short-baseline ($\lesssim$ 6.4 m) interferometric visibilities obtained with the aperture-masking technique on the 8 m telescope of the Gemini South Observatory, taken with 5 narrow-band filters throughout the $\sim$ 7.5–13 μm range.

We analyzed the interferometric data available for this source at both near- and mid-infrared wavelengths using a geometric model consisting of an extended, one-dimensional Gaussian, and a compact, two-dimensional Gaussian. We found that the mid-infrared data also trace the circumstellar disk seen at near-infrared wavelengths by Kraus et al. (2010).

By analyzing the wavelength-behavior of these model fits, we were able to derive a temperature profile of the circumstellar disk of $T(R) \propto R^{-1}$. Such a profile is much steeper than predicted by theoretical models of circumstellar disks. We then analyzed the inner rim formalism presented by Dullemond et al. (2001) as a function of stellar mass, we find that the importance of the inner rim grows steeply with the mass of the central star, which suggests that the compact appearance of the disk (and hence, the steep temperature profile we derive) may be due to a puffed up inner rim in the circumstellar disk around this massive young star.

References

Aitken, D. K., Smith, C. H., James, S. D., Roche, P. F., and Hough, J. H.: 1988, Infrared spectropolarimetry of AFGL 2591 - Evidence for an annealed grain component. *Monthly Notices of the Royal Astronomical Society* **230**, 629–638

Beck, S. C., Fischer, J., and Smith, H. A.: 1991, Infrared recombination lines of hydrogen from young objects in the southern Galactic plane. *Astrophysical Journal* **383**, 336–343

Beltrán, M. T., Brand, J., Cesaroni, R., et al.: 2006, Search for massive protostar candidates in the southern hemisphere. II. Dust continuum emission. *Astronomy and Astrophysics* **447**, 221–233

Busfield, A. L., Purcell, C. R., Hoare, M. G., et al.: 2006, Resolving the kinematic distance ambiguity of southern massive young stellar object candidates. *Monthly Notices of the Royal Astronomical Society* **366**, 1096–1117

Chan, S. J., Henning, T., and Schreyer, K.: 1996, A catalogue of massive young stellar objects.. *Astronomy and Astrophysics Supplement Series* **115**, 285

Churchwell, E., Babler, B. L., Meade, M. R., et al.: 2009, The Spitzer/GLIMPSE Surveys: A New View of the Milky Way. *Publications of the Astronomical Society of the Pacific* **121**, 213–230

De Buizer, J. and Fisher, R.: 2005, T-ReCS and Michelle: The Mid-Infrared Spectroscopic Capabilities of the Gemini Observatory, in *High Resolution Infrared Spectroscopy in Astronomy*, H. U. Käufl, R. Siebenmorgen, and A. Moorwood (eds.), pp 84–87

Dullemond, C. P., Dominik, C., and Natta, A.: 2001, Passive Irradiated Circumstellar Disks with an Inner Hole. *Astrophysical Journal* **560**, 957–969

Fedele, D., van den Ancker, M. E., Acke, B., et al.: 2008, The structure of the protoplanetary disk surrounding three young intermediate mass stars. II. Spatially resolved dust and gas distribution. *Astronomy and Astrophysics* **491**, 809–820

Fontani, F., Beltrán, M. T., Brand, J., et al.: 2005, Search for massive protostellar candidates in the southern hemisphere. I. Association with dense gas. *Astronomy and Astrophysics* **432**, 921–935

Hartmann, L.: 2009, *Accretion Processes in Star Formation: Second Edition*, Cambridge University Press, Cambridge

Kraus, S., Hofmann, K.-H., Menten, K. M., et al.: 2010, A hot compact dust disk around a massive young stellar object. *Nature* **466**, 339–342

Labeyrie, A., Lipson, S. G., and Nisenson, P.: 2006, *An Introduction to Optical Stellar Interferometry*, Cambridge University Press, Cambridge

MacLeod, G. C., van der Walt, D. J., North, A., et al.: 1998, 6.7 GHz Methanol Masers Associated with IRAS-Selected Sources. *Astronomical Journal* **116**, 2936–2942

Monnier, J. D.: 1999, *Infrared interferometry and spectroscopy of circumstellar envelopes*, *Ph.D. thesis*, University of California, Berkeley

Persson, S. E. and Campbell, B.: 1987, Identification of new young stellar objects associated with IRAS point sources. I - The southern Galactic plane. *Astronomical Journal* **94**, 416–428

Scalise, Jr., E., Rodriguez, L. F., and Mendoza-Torres, E.: 1989, Water-vapor maser emission from bright, unassociated IRAS point sources. *Astronomy and Astrophysics* **221**, 105–109

Stecklum, B., Caratti o Garatti, A., and Linz, H.: 2012, Integral-Field Spectroscopy of the Young High-Mass Star IRAS 13481-6124, in *Circumstellar Dynamics at High Resolution*, A. C. Carciofi and T. Rivinius (eds.), Vol. 464 of *Astronomical Society of the Pacific Conference Series*, p. 369

Urquhart, J. S., Busfield, A. L., Hoare, M. G., et al.: 2007, The RMS survey. ^{13}CO observations of candidate massive YSOs in the southern Galactic plane. *Astronomy and Astrophysics* **474**, 891–901

van Boekel, R., Dullemond, C. P., and Dominik, C.: 2005, Flaring and self-shadowed disks around Herbig Ae stars: simulations for 10 μm interferometers. *Astronomy and Astrophysics* **441**, 563–571

Vehoff, S., Hummel, C. A., Monnier, J. D., et al.: 2010, Mid-infrared interferometry of the massive young stellar object NGC 3603 - IRS 9A. *Astronomy and Astrophysics* **520**, A78

Wright, C. M., Siebenmorgen, R., Stecklum, B., Sterzik, M., and Käufl, H.-U.: 2008, A mid-infrared polarization capability for the ELT, Vol. 7014 of *Society of Photo-Optical Instrumentation Engineers (SPIE) Conference Series*

Xu, Y., Reid, M. J., Zheng, X. W., and Menten, K. M.: 2006, The Distance to the Perseus Spiral Arm in the Milky Way. *Science* **311**, 54–57

Chapter 6

A multi-wavelength study of the massive young stellar object AFGL 4176*

In this chapter, I present spatially-resolved observations of one MYSO, AFGL 4176, together with survey and literature data, ranging from interferometric observations with VLTI/MIDI in the mid-infrared, to single-dish Herschel measurements in the far-infrared, and sub-millimeter data from APEX.

This spatially-resolved, multi-wavelength data set is considered in terms of both radiative transfer and geometric models. We find that the observations are well described by one-dimensional models overall, but there are also substantial deviations from spherical symmetry at scales of tens to hundreds of astronomical units, which are revealed by the mid-infrared interferometric measurements. We use a multiple-component, geometric modeling approach to explain the mid-infrared emission on scales of tens to hundreds of astronomical units, and find the MIDI measurements are well described by a model consisting of a one-dimensional Gaussian halo and an inclined ($\theta = 60^\circ$) circumstellar disk extending out to several hundred astronomical units along a position angle of 112°.

Finally, we compare our results both with previous models of this source, and with those of other MYSOs, and discuss the present situation with mid-infrared interferometric observations of massive stars.

6.1 Introduction

The class of objects known as massive young stellar objects (MYSOs) are thought to represent massive stars at the earliest phases of evolution. The inherently large distances (several kpc) and high extinctions ($A_V \gtrsim 20$ mag) to typical MYSOs complicate attempts to characterize these objects observationally, and many studies (e.g. Grave and Kumar, 2009) rely on fitting the spectral energy distribution (SED) to untangle the underlying physics involved in the formation of massive stars.

However, it has been shown that pure SED fitting, i.e. without making use of any spatial information, is a highly degenerate approach, at best (e.g. Thamm et al., 1994; Men'shchikov and Henning, 1997). Different physical scales and temperature regimes of the circumstellar material can be resolved using a variety of techniques at different wavelengths, ranging from weakly-

---

*The material in this chapter has been published by P. Boley, H. Linz, R. van Boekel, J. Bouwman, T. Henning and A. Sobolev in *Astronomy and Astrophysics*, **547**, A88, 2012.

resolved single-telescope measurements, spectroscopic (spectroastrometric) measurements, and interferometric measurements, both at near-/mid-infrared and (sub-)millimeter wavelengths. The temperatures and regions thus probed range from $\sim 10^3 - 10^4$ K gas within the dust sublimation radius using spectroastrometry of molecular gas lines (e.g. Wheelwright et al., 2010), $\sim 10^3$ K dust at the inner dust disk radius using near-infrared interferometry (e.g. Kraus et al., 2010), $\sim 10^2 - 10^3$ K dust farther out in the disk (and possibly into outflow cones) using mid-infrared interferometry (e.g. Linz et al., 2009), and the broad distribution of cold $\sim 10^1 - 10^2$ K dust using millimeter-wave interferometry (e.g. Beuther et al., 2007) and single-dish measurements (e.g. Beltrán et al., 2006).

In this chapter, we present observations and the results of multi-wavelength modeling of one particular massive young stellar object, AFGL 4176 (also known as IRAS 13395-6153, G308.9+0.1). This object was identified as a candidate MYSO based on the similarity of the far-infrared spectrum to that of the Becklin-Neugebauer (BN) object in Orion (Henning et al., 1984, 1990). The class of so-called BN-type objects are luminous ($\gtrsim 10^3$ $L_\odot$) sources, extremely red (usually with no optical counterpart), with a broad peak in emission (flat spectrum in νF_ν) between 50 and 200 μm and deep absorption due to silicates at 10 μm. They are generally interpreted as young (possibly still forming) massive stars, surrounded by a thick dust envelope, despite the unclear nature of the prototype object Orion BN (see the work by Tan (2004), for example).

At radio wavelengths, using the Molonglo Observatory Synthesis Telescope (MOST), Caswell et al. (1992) reported a small-diameter source ($\leq 0\overset{\prime}{.}2$) roughly coincident with the IR source AFGL 4176. The integrated flux densities are 0.31 Jy at 843 MHz and 0.40 Jy at 1415 MHz, confirming the emission is thermal bremsstrahlung radiation arising from an H II region. Using the Australian Telescope Compact Array (ATCA), Phillips et al. (1998) reported compact continuum emission at 8.6 GHz spanning about $10''$, with a collection of 6.7 GHz methanol masers on the northern edge. Later, Ellingsen et al. (2005) showed the 8.6 GHz continuum emission extends to about $1'$. Finally, the 1.2 mm dust continuum was mapped by Beltrán et al. (2006), and comprises a roughly circular, $\sim 40''$ clump at the same location with an estimated mass of 1120 $M_\odot$ at 5.3 kpc, and a fainter clump (estimated mass 177 $M_\odot$ at 5.3 kpc) about $1\overset{\prime}{.}5$ to the east.

In the near infrared, AFGL 4176 is a point source for seeing-limited observations. Using speckle interferometry, however, Leinert et al. (2001) found a faint extended halo in the K band, with a size of $1\overset{\prime\prime}{.}6 \pm 0\overset{\prime\prime}{.}4$. The positions from the Two Micron All Sky Survey (2MASS) and the methanol masers reported by Phillips et al. (1998) are within $0\overset{\prime\prime}{.}7$. De Buizer (2003) detected a large number of shocked H_2 emission blobs around AFGL 4176 by means of narrow-band NIR imaging. However, their spatial distribution does not reveal a preferred direction for a potential jet, and in general, the association of AFGL 4176 with a jet or outflow remains unclear. The source was also observed in the mid- through far- infrared by the space missions IRAS, MSX, ISO, Spitzer and Herschel. We note that the coordinates listed in the IRAS Point Source Catalog appear to be erroneous when compared with the MSX 12 μm and Spitzer 24 μm images, and adopt the 2MASS position of $\alpha = 13^{\mathrm{h}}43^{\mathrm{m}}01\overset{\mathrm{s}}{.}70$ $\delta = -62^\circ 08' 51\overset{\prime\prime}{.}23$ (J2000) as the location of the infrared source. The ISO spectrum shows deep silicate absorption features at 9.7 and 18 μm, as well as absorption due to water ice at 3 μm, CO_2 ice at 4.3 μm, and emission lines of [Ne II] at 12.8 μm; [S III] at 12.0, 18.7 and 33.5 μm; [O I] at 145.5 μm and possibly 63.2 μm; and [C II] at 157.7 μm.

The distance to AFGL 4176 remains poorly constrained. Using both the velocity curve of Brand and Blitz (1993) with updated parameters from Levine et al. (2008), and the velocity curve of Reid et al. (2009), we find that the combination of the source's LSR velocity of ~ -51 km s^{-1} (e.g. Fontani et al., 2005; De Buizer et al., 2009) and galactic coordinates are forbidden[1]. Consequently, a kinematic distance cannot be determined for AFGL 4176 using these rotation curves. Despite this, several authors (e.g. Beltrán et al., 2006; Fontani et al., 2005; Grave and Kumar, 2009) report kinematic distances of around 5 kpc. Saito et al. (2001) showed that the spread in velocities of $C^{18}O$ molecular clumps in the vicinity is high (~ 30 km s^{-1}), meaning that kinematic estimates of the distance to this object should be highly uncertain, even after improvement of the galactic structure parameters. To date, other means of the distance measurements (e.g. maser parallax measurements) have not been applied to AFGL 4176. Because of this uncertainty, we consider the observational data in terms of both "near" (3.5 kpc) and "far" (5.3 kpc) distances, corresponding to the edges of the large $C^{18}O$ complex as determined by Saito et al. (2001).

The present chapter is similar in scope to previous infrared interferometric studies of MYSOs by Linz et al. (2009); Follert et al. (2010); de Wit et al. (2010); Kraus et al. (2010). However, in this work on AFGL 4176, we go beyond traditional SED modeling techniques and use a far more comprehensive approach, including not only flux values, but also spatial information at mid-infrared, far-infrared, and sub-millimeter wavelengths directly into the fitting process. Such an approach helps to break the degeneracies inherent in modeling the SEDs of deeply-embedded sources, and provides structural information on scales ranging from tens of AU up to a parsec. We begin by presenting and discussing new observations of AFGL 4176, then go to one-dimensional radiative transfer modeling of the entire data set. Next, we use a geometric component analysis of the mid-infrared interferometric data to explore deviations from spherical symmetry, which we interpret as strong evidence for a circumstellar disk around this object. Finally, we compare the results of our study with those of previous studies of this object, as well as studies of other MYSOs.

6.2 Observations and data reduction

6.2.1 Mid-infrared interferometry

AFGL 4176 was observed with the two-telescope mid-infrared interferometer MIDI on the Very Large Telescope Interferometer (VLTI) of the European Southern Observatory on Cerro Paranal in Chile. Observations were conducted in 2005-2007 and 2011-2012 with both the 8.2 m Unit Telescopes (UTs) and the 1.8 m Auxiliary Telescopes (ATs) as part of guaranteed-time observations (proposal IDs 074.C-0389, 075.C-0755, 076.C-0757, 077.C-0440, 078.C-0712 and 084.C-1072). In total, 37 points in the *uv* plane were obtained for projected baselines ranging from 5 to 62 meters and a variety of position angles, with six of the measurements obtained with the UT telescopes, while the remaining 31 were obtained with the AT telescopes. This represents, by far, the largest collection of long-baseline mid-infrared interferometric observations presented for a MYSO to date. A summary of the observations is shown in Table 6.1, and the *uv* coverage is shown in Fig. 6.1. For clarity, the individual observations have been color-coded by projected baseline length: purple indicates measurements with the longest baselines (60-64 m); red (36-49 m) and green (25-32 m) show those with intermediate baselines; blue (13-16 m) and orange (5-11 m) mark the shortest baseline measurements.

We used the prism as the dispersive element, resulting in spectrally-resolved visibility amplitudes and differential phases with a resolution of $\lambda/\Delta\lambda = 35$ in the wavelength range $8-13$ μm. All observations were carried out in the HIGHSENS mode, meaning the correlated flux and the photometric measurements are done separately. For a detailed description of this observing

---

[1] We note that the tangential solution of these velocity curves at the coordinates of AFGL 4176 occurs for $V_{\rm LSR} \approx -49$ km s^{-1} and corresponds to about 5.3 kpc, which may explain the kinematic distances reported by other authors.

Table 6.1: Observation log

Date/time (UTC)	Telescopes	Proj. baseline (m)	Position angle (deg.)	Avg. visibility
2005-03-02 08:08	UT3-UT4	61.6	112.1	0.02
2005-06-24 04:54	UT3-UT4	61.8	169.3	0.02
2005-06-25 22:50	UT1-UT2	49.3	19.3	0.07
2005-06-26 02:05	UT1-UT2	41.9	49.8	0.08
2005-06-26 03:27	UT1-UT2	36.3	62.4	0.04
2005-06-27 03:31	UT2-UT3	30.3	85.6	0.08
2006-02-22 05:46	E0-G0	16.0	41.9	0.30
2006-04-18 08:01	D0-G0	26.5	121.4	0.06
2006-04-24 07:30	E0-G0	13.4	119.4	0.31
2007-02-11 06:24	E0-G0	16.0	40.5	0.23
2007-02-12 06:18	G0-H0	31.9	40.0	0.13
2007-03-15 07:08	G0-H0	31.2	77.7	0.11
2007-03-16 09:13	G0-H0	28.3	106.8	0.07
2007-04-18 04:55	E0-G0	15.6	77.8	0.20
2007-05-24 01:51	E0-G0	15.8	68.7	0.27
2007-06-19 02:35	G0-H0	28.9	101.0	0.06
2007-07-03 01:31	E0-G0	14.6	98.9	0.28
2011-05-09 02:15	B2-C1	9.8	21.7	0.47
2011-05-09 02:49	B2-C1	9.6	27.0	0.46
2011-05-09 03:14	B2-C1	9.5	31.0	0.49
2011-05-09 03:29	B2-C1	9.4	33.4	0.52
2011-05-09 04:54	B2-D0	25.9	46.4	0.18
2011-05-09 05:27	B2-D0	24.7	51.6	0.16
2011-05-09 08:28	B2-C1	5.3	80.9	0.61
2011-05-10 02:23	B2-D0	29.3	23.5	0.20
2011-05-10 03:46	B2-D0	27.7	36.7	0.19
2012-02-01 09:04	A1-B2	10.7	103.5	0.51
2012-02-24 05:20	D0-H0	63.8	37.3	0.06
2012-02-24 05:30	D0-H0	63.8	39.8	0.06
2012-02-24 09:29	D0-H0	59.9	92.0	0.05
2012-03-26 09:05	I1-K0	32.4	38.6	0.11
2012-03-26 09:41	I1-K0	30.8	43.1	0.10
2012-03-27 05:21	I1-K0	38.0	9.1	0.10
2012-03-27 05:26	I1-K0	37.9	9.7	0.09
2012-03-27 05:34	I1-K0	37.8	10.9	0.09
2012-03-27 07:09	I1-K0	36.2	23.8	0.10
2012-03-29 04:08	I1-K0	38.2	179.9	0.09

Notes. For clarity, observations are color-coded by projected baseline length, using the same color scheme as Fig. 6.1.

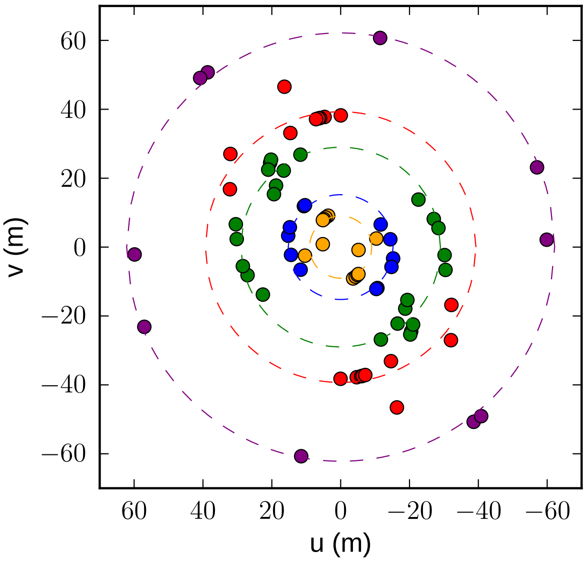

Figure 6.1: *uv* coverage of MIDI observations. North is up, east is left. The positions have been color-coded by projected baseline length, and the dashed lines indicate the mean projected baselines for each color (*orange* – 8.1 m; *blue* – 15.2 m; *green* – 28.5 m; *red* – 42.5 m; *purple* – 61.7 m).

procedure, see the work by Leinert et al. (2004). In general, every science measurement was preceded and/or followed by a calibration measurement of a bright single star of known diameter.

The raw data were reduced using the MIA+EWS package version 1.7.1. Masks were generated for each interferometric measurement from the corresponding photometric data. From the calibrator measurements taken throughout the night, we computed the mean sensitivity function, relating counts/s to Jy of correlated flux. The uncertainty in this sensitivity function was taken to be the standard deviation over all the calibrator measurements in the night, and is typically on the order of 10%.

Because the quality of the photometric data from the ATs is generally poor, we assume AFGL 4176 to be non-variable and use an average total spectrum from the UTs for computing the visibility amplitude from the correlated flux. Uncertainties in the final visibilities were calculated using standard error propagation formulae.

6.2.2 Far-infrared imaging

The AFGL 4176 region was covered by far-infrared observations taken by the Herschel Space Observatory (Pilbratt et al., 2010), within the framework of the Hi-GAL survey (Molinari et al., 2010). In this chapter, we present bolometer data at 70 and 160 μm, obtained with the PACS instrument (Poglitsch et al., 2010) on August 16, 2010. These data are scan maps with a scan rate of $60''$/s, which slightly degrades the spatial resolution compared to the theoretical diffraction limit. After onboard preprocessing, the data are transmitted with a downlink rate of 5 frames/s for the 70 μm filter, and 10 frames/s for the 160 μm filter. The final resulting spatial resolution for the 70 μm data is about $9\farcs2$, and $12\farcs6$ for the 160 μm data, although the true PSF is asymmetric. For a more detailed description of the observing procedure used in the Hi-GAL program, we refer to the description of the observing strategy by Molinari et al. (2010).

We extracted the level-0 data from the Herschel Science Archive of the relevant $2^\circ \times 2^\circ$ strip covering AFGL 4176 (OBSIDs 1342203085 and 1342203086). Despite the occurrence of very bright far-infrared sources in the Hi-GAL fields, these observations were performed with the normal high-gain settings for the PACS bolometers. The level-0 data were processed with the HIPE software (Ott, 2010) version 8.0.3178 up to the so-called level-1, where internal data units have been translated to Janskys, and outliers (i.e. glitches) in the data and saturated pixels have been removed or masked.

In addition to these standard procedures, we applied a task for eliminating the electronic cross-talk within the bolometers, which can cause the appearance of ghosts close to strong compact sources. Furthermore, we use a module recently developed by the instrument team which applies a non-linearity correction to the data. This is especially important for our purpose, since in the high-gain mode used for the Hi-GAL program, very bright sources will trigger a non-linear response in the bolometer behavior, resulting in an altered PSF and decreasing measured fluxes by $10 - 15\%$.

The removal of $1/f$ noise and effects resulting from temperature drifts within the bolometers, as well as the final mapping, was done using the version 7 of the Scanamorphos program (Roussel, 2012, submitted to PASP), for which we used the “galactic,” “noglitch” and “parallel” options. Final maps were produced with a pixel scale of $3\farcs2$ for both filters, which is the native plate scale for the 70 μm bolometers, and half the native plate scale for the 160 μm bolometers.

6.2.3 870 μm imaging

AFGL 4176 was also imaged at 870 μm as part of the APEX Telescope Large Area Survey of the Galaxy (ATLASGAL). We refer to the publication by Schuller et al. (2009) regarding the general outline of this sub-millimeter continuum survey, and the technical details of the observations and the data reduction. In the present work, we use a map from the re-reduction of the data in 2011, done by the F. Schuller, using refined methods for thermal drift removal within the bolometer reduction software BOA (Schuller et al., 2009). Furthermore, the treatment of strong sources within the iterative process of the data reduction has been improved. Finally, the data have been mapped onto a 6-arcsec grid, using version 2.18 of the mapping software SWarp (Bertin, 2010), which prevents the formation of spurious Moiré patterns still present in earlier ATLASGAL maps.

6.3 Results

We show an AO-corrected acquisition image of AFGL 4176 obtained with the 8.2 m telescope UT3 on Mar. 2, 2005 in the upper panel of Fig. 6.2. The image was obtained using the SiC filter, which has a central wavelength of 11.8 μm and a width of 2.32 μm. In the lower panel, we compare a cut through the acquisition image of AFGL 4176 with an analogous cut through the acquisition image of the unresolved calibrator star HD 102461, which was observed immediately after the science source. From the similarity of the spatial cut through the image of AFGL 4176 to that of the calibrator, we conclude that AFGL 4176 is at most marginally resolved in diffraction-limited 8 m-class telescope images at N-band wavelengths.

In Fig. 6.3, we show the average N-band spectrum of AFGL 4176 from the 8.2 m UT telescopes, used to derive the visibility amplitude from the correlated flux measurements. The visibility amplitudes as a function of wavelength are shown in Fig. 6.4, where the measurements have been ordered by projected baseline length, and are presented using the same color scheme

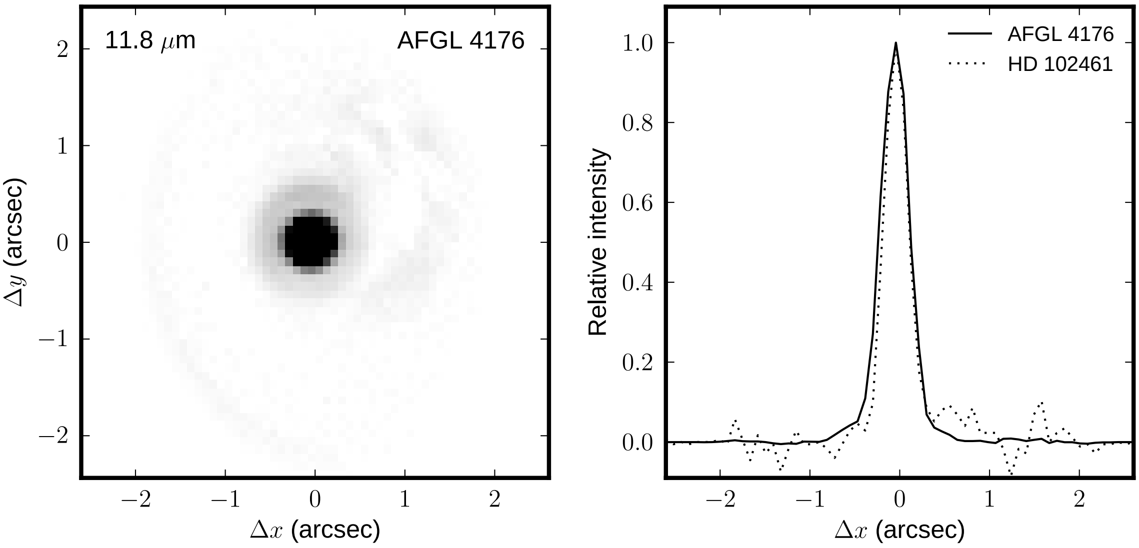

Figure 6.2: *Left:* Acquisition image of AFGL 4176 from MIDI obtained on the 8.2 m UT3 telescope using the SiC filter, which has a central wavelength of 11.8 μm and a width of 2.32 μm. *Right:* Comparison of a cut through the acquisition image of AFGL 4176, and an analogous image of the unresolved calibrator star HD 102461.

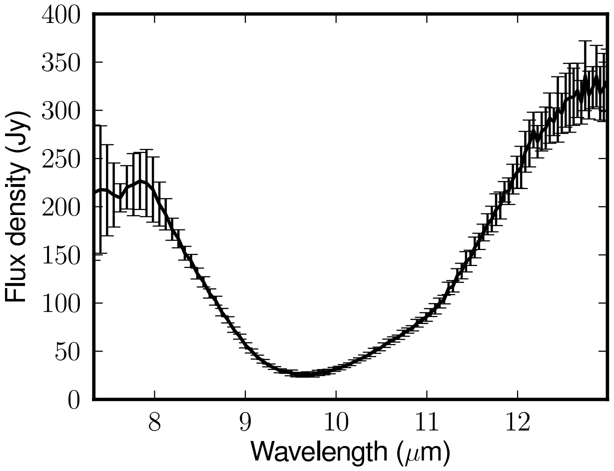

Figure 6.3: Average N-band spectrum measured with MIDI on the UTs.

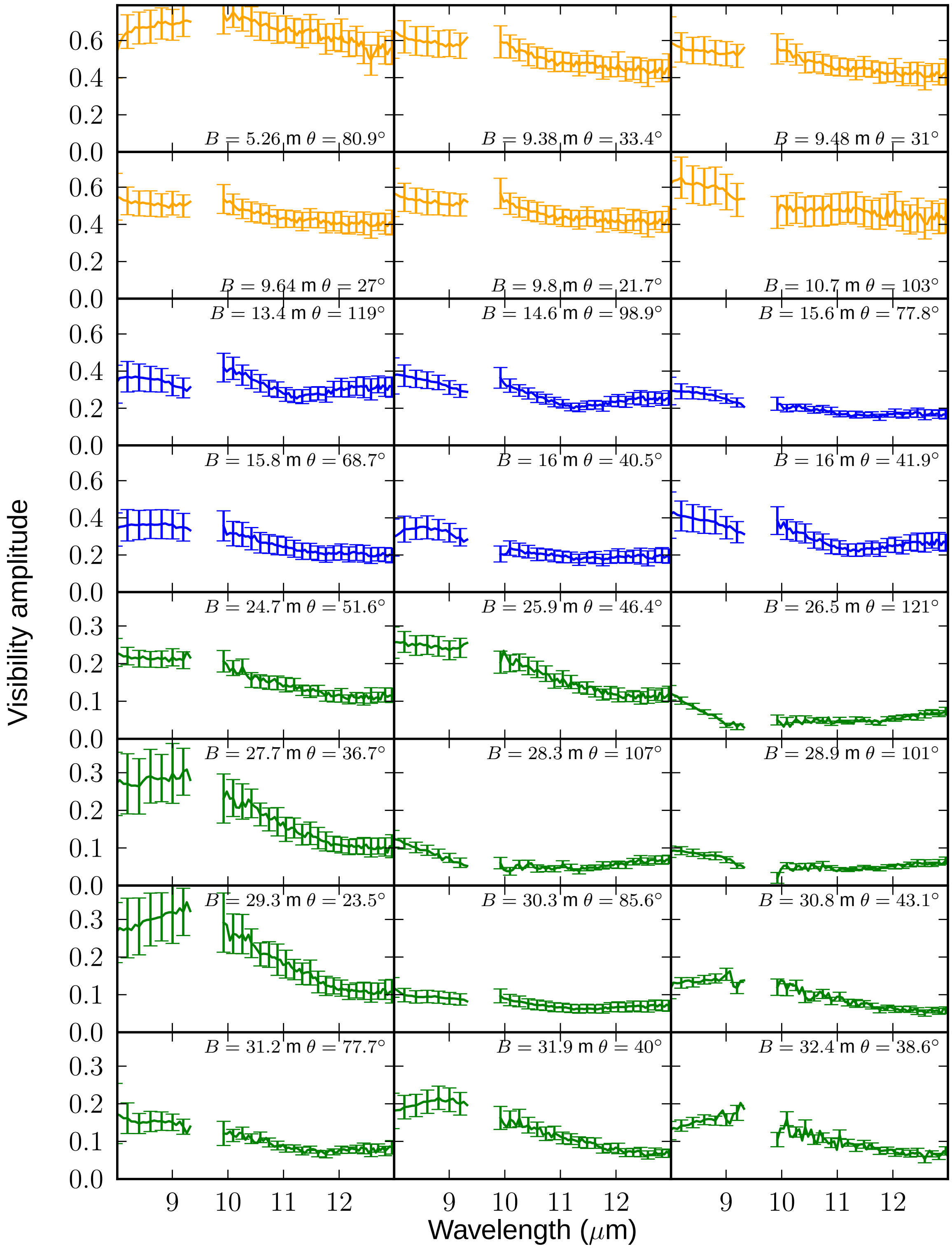

Figure 6.4: The complete set of visibility amplitudes measured with MIDI. The plots are sorted by projected baseline length, indicated as B in the inset text, together with the position angle θ. The color coding is the same as for Fig. 6.1.

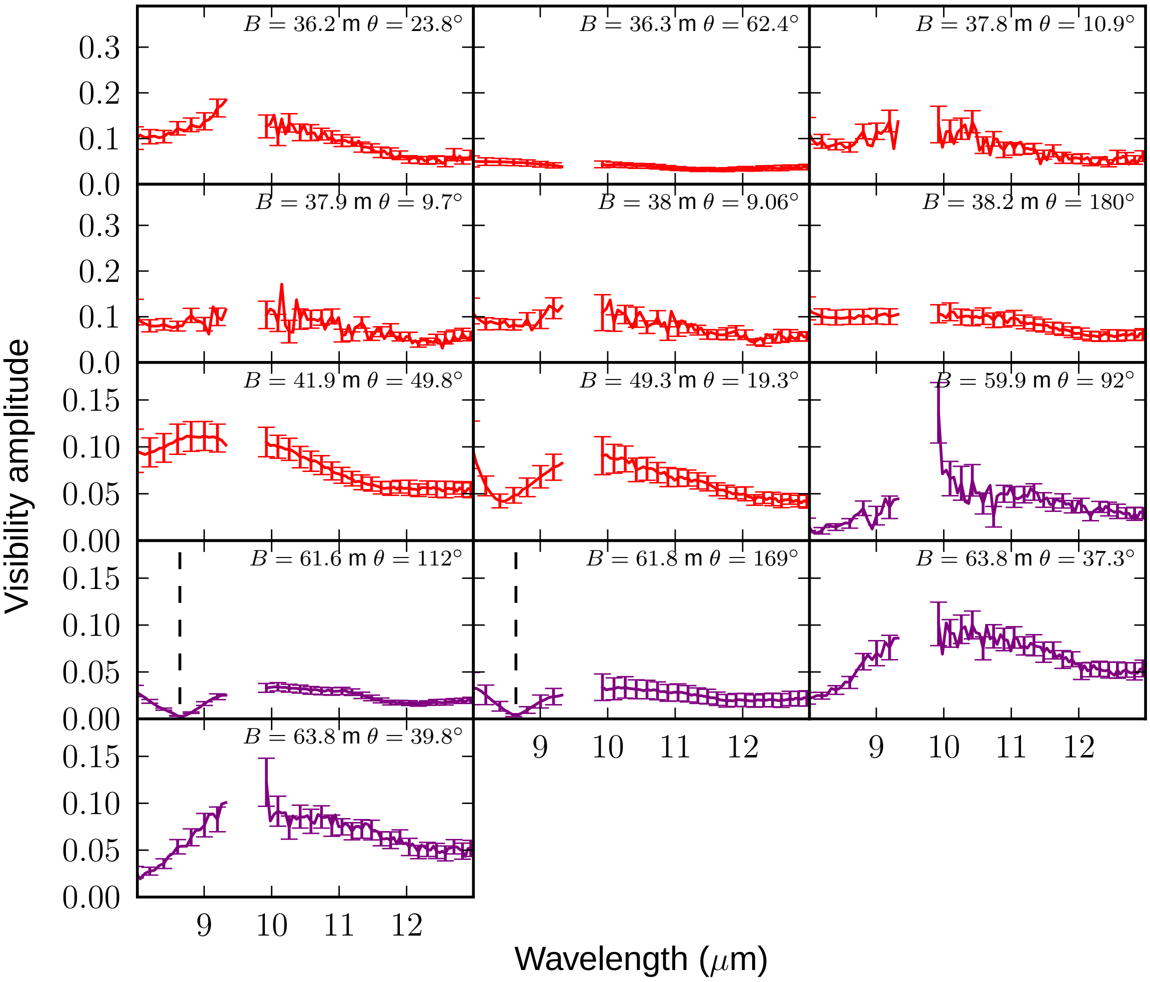

Figure 6.4: Continued.

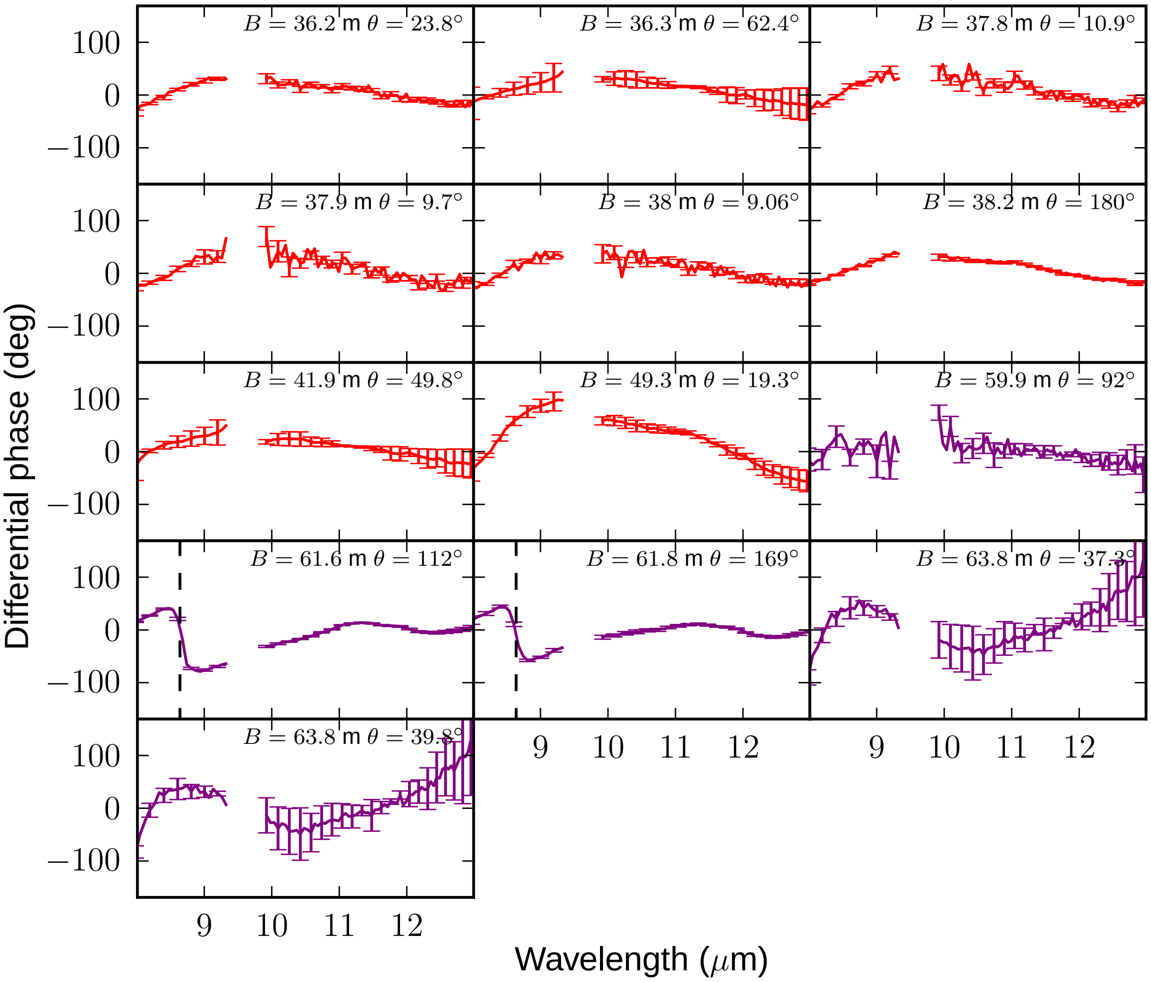

Figure 6.5: Differential phases measured with MIDI for *uv* points with projected baselines longer than 36 m. The vertical dashed line for the two measurements with $B = 61.6$ and 61.8 m shows the location of the phase flip, indicative of a zero crossing in the visibility amplitude.

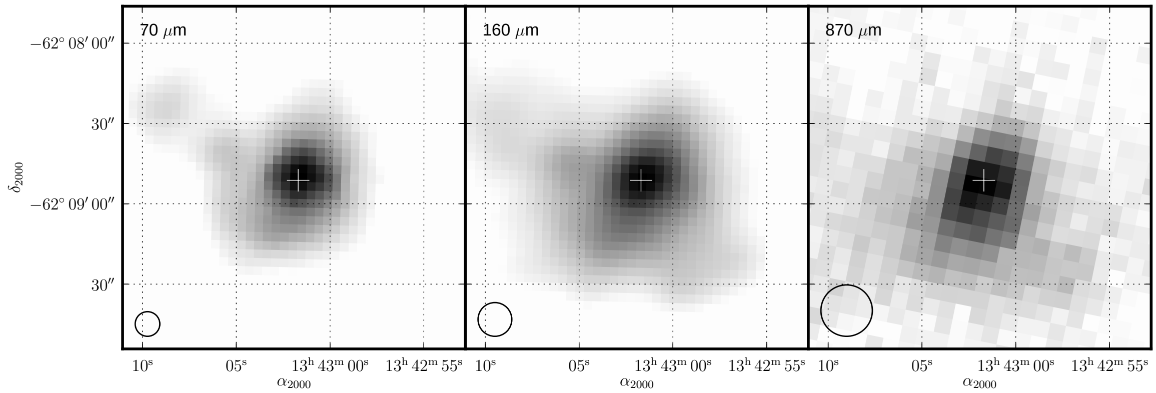

Figure 6.6: The 70 and 160 μm images obtained from the Hi-GAL survey with the Herschel Space Observatory, and the 870 μm image from the ATLASGAL survey with the APEX telescope. The circle in the lower left corner of each image indicates the beam size. The two Hi-GAL images are shown with logarithmic scaling of the intensity, while the ATLASGAL image is shown with linear scaling.

as in Fig. 6.1. Finally, in Fig. 6.5, we show the differential phases measured with MIDI for the measurements with $B > 36$ m (the differential phases at shorter baselines are not shown, as they are essentially zero).

We note the clear presence of a zero crossing in both the visibility amplitude and differential phase for the two measurements with $B = 61.6$ and 61.8 m, indicated with a vertical dashed line in Figs. 6.4 and 6.5. We previously interpreted this as evidence for circular symmetry at the smallest scales probed (Boley et al., 2011). In order to test this hypothesis, we targeted this spatial frequency for follow-up observations with the ATs at other position angles on Feb. 24, 2012 (the remaining "purple" measurements in Figs. 6.1, 6.4 and 6.5). However, while a non-zero differential phase is measured, a zero crossing is clearly *not* present in these follow-up observations, implying deviations from spherical symmetry at the smallest angular scales probed by MIDI.

In Fig. 6.6, we show the images at 70 and 160 μm (Hi-GAL) and 870 μm (ATLASGAL). The approximate beam size for each image is $9\overset{\prime\prime}{.}2$, $12\overset{\prime\prime}{.}6$ and $19\overset{\prime\prime}{.}2$, respectively, and is shown as a circle in the lower left-hand corner of each image. The position of the infrared source is indicated as a cross in each image. The position of the emission peak in the Hi-GAL data corresponds to that of the 2MASS source to within the pointing accuracy of the observations. In the ATLASGAL data, the emission peak lies $\sim 4''$ south of the IR position, although this is also within the rms pointing accuracy of the ATLASGAL observations.

At the Hi-GAL wavelengths, within a $36''$ aperture, we measure flux densities of 2382 Jy and 1383 Jy at 70 μm and 160 μm, respectively. While the absolute flux calibration on these data is accurate to within 5% (Herschel PACS Report PICC-ME-TN-037, Apr. 12, 2011), there is significant, non-uniform background emission in the region which is difficult to account for. Therefore, these values should be treated as upper limits, as it is not clear where the background begins to dominate and the extended emission associated with the source stops. The 870 μm emission is also quite extended; within a $19''$ aperture, which covers just the central emission peak, we measure an integrated flux density of 2.86 Jy, while in a larger $72''$ aperture, covering the extended emission, we measure an integrated flux density of 10.6 Jy.

In Table 6.2 we list the photometric data and effective aperture sizes from previous works and surveys which we consider in modeling our source. Unless noted otherwise, we compare

Table 6.2: Photometric data

Wavelength (μm)	Flux density (Jy)	Aperture ($''$)	Reference
1.25	$(2.664 \pm 0.139) \times 10^{-3}$	4	(1)
1.65	0.123 ± 0.004	4	(1)
2.20	1.760 ± 0.04	4	(1)
9.0	173.2 ± 1.33	11	(2)
12.0	250.70 ± 12.535	–	(3)
18.0	434.2 ± 13.3	11	(2)
25.0	601.60 ± 30.080	–	(3)
60.0	2701.00 ± 243.09	–	(3)
65.0	1506.0 ± 434.0	27	(2)
70.0	2382.2	36	(4)
90.0	849.1 ± 208.0	27	(2)
100.0	3566.00 ± 534.90	–	(3)
140.0	1437.0 ± 127.0	44	(2)
160.0	1939.0 ± 293.0	44	(2)
160.0	1383.4	36	(4)
870.0	2.86	19	(4)
870.0	10.6	72	(4)
1200.0	3.86	39	(5)

References. (1) 2MASS; (2) AKARI; (3) IRAS; (4) This work; (5) Beltrán et al. (2006)

our model data (see Sec. 6.4.1) to the observations by considering the flux contribution within a Gaussian aperture with the same FWHM as the observational data.

In Fig. 6.7, we show J-, H- and K_s-band images of AFGL 4176 and its immediate surroundings from the first data release of the ESO public survey VISTA Variables in the Vía Láctea (VVV; Saito et al., 2012). These images were obtained on the 4 m VISTA telescope on Cerro Paranal, and surpass 2MASS both in spatial resolution and sensitivity. The seeing for the J, H and K_s images presented here is $0\overset{''}{.}82$, $0\overset{''}{.}86$ and $0\overset{''}{.}94$, respectively. AFGL 4176 is present as a bright, compact source, and saturated in both the H and K_s images.

Finally, the region around AFGL 4176 was mapped in several molecular lines as part of the Millimeter Astronomy Legacy Team 90 GHz (MALT90) survey (Foster et al., 2011) with the Mopra 22 m telescope. Of the 16 spectral lines which were mapped as part of the survey, HCO+ was the brightest in AFGL 4176. The HCO+ line data, shown in Fig. 6.8, have a spectral resolution of ~ 0.11 km s^{-1}. This line is a tracer of dense molecular gas, and has been used as an outflow indicator (e.g. Hofner et al., 2001). However, in the case of AFGL 4176, the spectrum is very well approximated by a Gaussian (FWHM 3.5 km s^{-1}), and shows no signs indicating the presence of an outflow.

6.4 Analysis

6.4.1 One-dimensional radiative transfer modeling

As shown in Sec. 6.3, AFGL 4176 shows evidence for deviations from spherical symmetry only at the scales probed by our mid-infrared interferometric observations, which correspond to scales of roughly 20 to 200 mas. Furthermore, no outflow component has been revealed in searches by De Buizer (2003) and De Buizer et al. (2009), nor in the HCO+ data presented in this work (Fig. 6.8). Since there is no evidence for asymmetry or preferred geometry on scales larger than

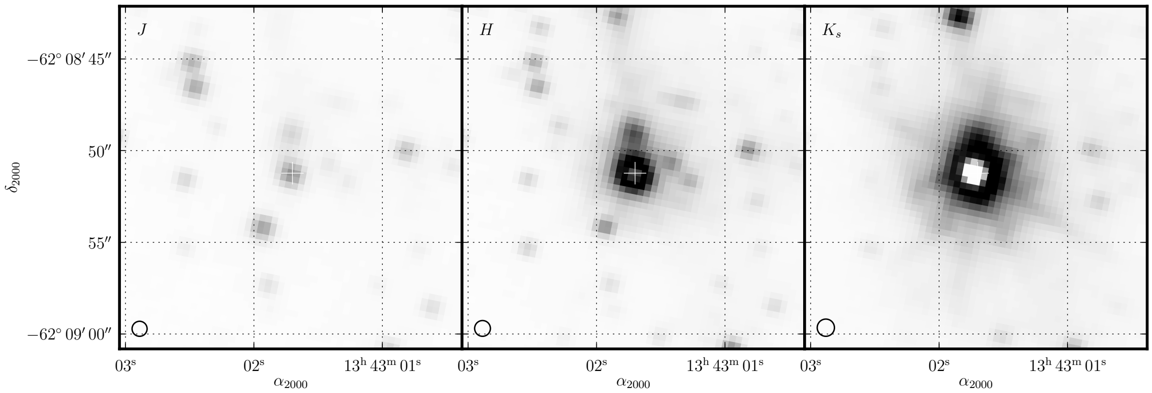

Figure 6.7: J-, H- and K_s-band images from the VVV survey. AFGL 4176, indicated with a white cross, is saturated in both the H and K_s images. The circle in the lower left corner of each image indicates the seeing, as measured from the guide star by the autoguider.

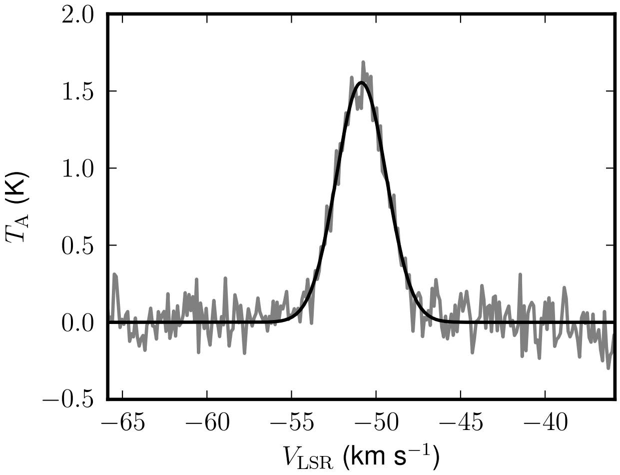

Figure 6.8: Spectrum of HCO+ from the MALT90 survey. The observations are shown with the gray line, while a Gaussian fit is shown with the black line.

a few hundred AU, we begin with one-dimensional models to explore the overall structure of this source.

We model AFGL 4176 using the one-dimensional radiative transfer code MoDust, which was developed by A. de Koter and J. Bouwman. MoDust uses the Feautrier method to solve the radiative transfer equation (Feautrier, 1964), and has been used previously by e.g. Malfait et al. (1999); Kemper et al. (2001); Bouwman et al. (2001). Using MoDust, the dust temperature structure is iteratively solved for a given density structure and dust properties. Different opacities can be given for different temperature regimes, thus making it possible to dynamically determine the distributions of different types of dust throughout the model.

Using this code, we produce radial intensity profiles of the source image on the sky at all wavelengths for which we have observations, i.e. from 1.25 μm to 1.2 mm. From these radial intensity profiles, we calculate aperture-corrected flux values for the SED, PSF-convolved images for comparison with the Hi-GAL and ATLASGAL data[2], and interferometric visibilities for comparison with the MIDI data. We do not attempt to match the near-IR VVV images, as AFGL 4176 is saturated in them. The relative goodness of fit of models was assessed by constructing a χ^2 estimate which includes roughly equal contribution from these three measures.

Constraints and uncertainties on fundamental parameters

As noted in the introduction, the distance to AFGL 4176 cannot be reliably determined at present. We therefore chose to investigate both near and far models, at distances of 3.5 and 5.3 kpc, respectively.

Under the assumption that the H II region seen in radio observations is powered by the AFGL 4176 source, the number of ionizing photons, and consequently a minimum inferred spectral type, can be determined. The radio flux measurements at 843 and 1415 MHz of Caswell et al. (1992) appear to be consistent with thermal bremsstrahlung radiation from an H II region. For a distance of 5.3 kpc, using the main-sequence luminosities for O stars from Martins et al. (2005) and the stellar atmosphere models of Kurucz (1979), we find a minimum spectral type of the central source of about O8. This corresponds to an effective temperature of about 33 000 K, which we adopt for the temperature of the central blackbody source in our models.

For the amount of foreground extinction, we adopt a simple prescription of 1 magnitude of visual extinction per kiloparsec, giving us $A_V = 3.5$ and 5.3 mag for the near and far models, respectively. This small amount of additional (i.e. interstellar) extinction was applied on top of our models, and has the effect of further lowering the near-IR flux levels and slightly deepening the 10 μm silicate feature.

Dust model

One of the foremost practical constraints on the choice of dust model is the need for opacities at short wavelengths ($\lambda \leq 0.1$ μm). Since the luminosity of this source is on the order of 10^5 $L_\odot$ and the amount of ionizing flux (inferred from the radio continuum observations) is equivalent to at least an O8 star star, the vast majority of the stellar radiation is emitted at UV and optical wavelengths.

A number of attractive dust models for conditions expected in protostellar cores, envelopes and protoplanetary disks have been developed (for example by Ossenkopf and Henning, 1994; Henning and Stognienko, 1996; Semenov et al., 2003). However, a common shortcoming of these models is the lack of opacity information at short (UV) wavelengths, due to convergence problems of the grain models (D. Semenov, private communication). On the other hand, the empirically derived opacities of Laor and Draine (1993) and subsequent works cover wavelengths from 100 Å through 1 mm, with the caveats that the real physical makeup of the dust is unknown, and that at far-IR and (sub)mm wavelengths, where extinction is effectively impossible to measure, the dust opacities are not well known.

We therefore adopt a multi-component, temperature-dependent dust model, guided by the presence of known spectral features in the observations, and limited by the available coverage and reliability of different opacity models at different wavelength regimes. The transition between different regimes, and therefore the presence of different species throughout the surrounding material, are governed by the temperature structure iteratively solved by MoDust.

---

[2] For the PACS array on Herschel, we took the PSFs from the PACS calibration web site (http://herschel.esac.esa.int/twiki/bin/view/Public/PacsCalibrationWeb). For the LABOCA bolometer array used on the APEX telescope, we take the PSF to be well-approximated by a Gaussian with FWHM = $19\farcs2$ (Siringo et al., 2009).

Table 6.3: One-dimensional radiative transfer model parameters

Model	D (kpc)	r_1 (AU)	r_2 (AU)	r_{23} (AU)	r_o (AU)	ρ_1 (g cm^{-3})	ρ_{23} (g cm^{-3})	p_1	p_2	p_3	$M_{\rm dust}$ (M$_\odot$)	$L_\star$ (10^5 L$_\odot$)
Near	3.5	40	65	70 000	125 000	1.71×10^{-18}	3.56×10^{-22}	1.8	1.05	0.5	4.70	1.44
Far	5.3	58	108	56 000	195 000	9.22×10^{-19}	4.71×10^{-22}	1.2	0.9	0.5	15.8	2.88
G91	4.0	—	100	2646	50 134	—	1.49×10^{-21}	—	2.0	0.0	1.32	1.57

Based on the presence of the 3.1 μm water ice absorption feature in the ISO SWS spectrum, we infer that at least some of the amorphous silicate grains are surrounded by ice mantles, formed in the cold material of the parent molecular cloud. To include this in our model, we use opacities from the coagulation model of Ossenkopf and Henning (1994). Following the suggestions in that paper, we interpolate between columns 1 and 2 of their Table 1 using the depth of the 3.1 μm ice feature. From the ISO SWS spectra, we measure $\tau_{3.1} = 0.4$, and use the resulting interpolated opacities for regions where $T_{\rm dust} < 130$ K.

For grains with $T_{\rm dust} > 130$ K, we use the "astronomical silicates" and graphite grains of Laor and Draine (1993) with the "MRN" distribution of grain sizes ($n(a) \propto a^{-3.5}$ for grains between 5 nm and 250 nm, where n is the number of grains, and a is the grain radius), which is generally appropriate for diffuse ISM conditions. We adopt a ratio of 60:40 for the silicate to graphite mass abundance in this temperature regime, although we note this is not directly constrained by observations. For the graphite grains, we adopt a destruction temperature of 950 K, which corresponds to the process of OH sputtering (Duschl et al., 1996). For the silicate grains, we do not enforce a destruction temperature; at the inner edge of our envelope models, the silicate grains typically reach a temperature of about 2000 K.

The dust model therefore consists of a region of "cold" ($T_{\rm dust} < 130$ K) amorphous silicate and carbon grains with ice mantles, as well as "warm" (130 K< $T_{\rm dust} < 950$ K for graphites, and 130 K< $T_{\rm dust}$ for silicates) amorphous grains similar to the "standard" diffuse ISM mix.

Density structure

For the density structure of the dust in our model, we adopt a piecewise power law consisting of concentric, spherical shells, with no gaps in between the shells. In order to simultaneously reproduce the observed visibility levels, far-IR/sub-mm spatial distributions and SED with this model, we find it necessary to include at least three shells, with a jump in density at the interface between the first (innermost) shell and the second shell. At the interface between the second and third shells, however, we were able to achieve acceptable fits without a density jump, thereby avoiding the need for an additional model parameter describing this. We therefore characterize the density of material in the outer shells by the density ρ_{23} at the contact point r_{23} of the second and third shells. The precise structure used, therefore, has in principle nine free parameters (r_1, r_2, r_{23}, r_o, ρ_1, ρ_{23}, p_1, p_2, p_3) and follows the form

$$\rho(r) = \begin{cases} \rho_1 \left(\frac{r_1}{r}\right)^{p_1} & r_1 < r \leq r_2 \\ \rho_{23} \left(\frac{r_{23}}{r}\right)^{p_2} & r_2 < r \leq r_{23} \\ \rho_{23} \left(\frac{r_{23}}{r}\right)^{p_3} & r_{23} < r \leq r_o \end{cases} \tag{6.1}$$

Results

We present two fits to the observational data using the three-shell model: one for the "near" distance of 3.5 kpc, and one for the "far" distance of 5.3 kpc. The parameters are summarized in the first two lines of Table 6.3; comparisons with the observations are shown in Figs. 6.9 and 6.10: the top panel shows the modeled flux levels from the photometric data from Table 6.2;

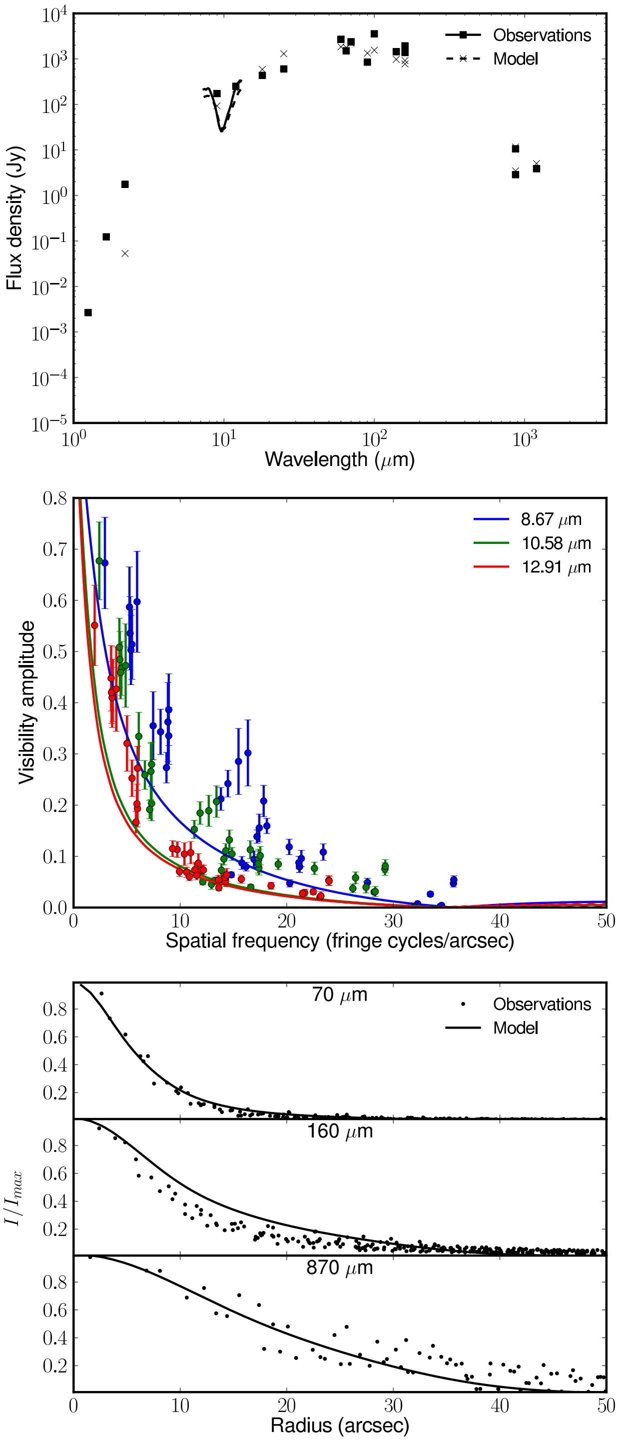

Figure 6.9: Model fits of the observational data for the near model. *Top:* The SED, where the aperture-corrected model flux levels are shown as crosses and the dotted line, and the observed flux values are shown as filled squares and the solid line. *Middle:* The modeled (lines) and observed (points) MIDI visibilities for three wavelengths. *Bottom:* The modeled (blue points) and observed (green points) radial intensity distributions from the Hi-GAL (70 and 160 μm) and ATLASGAL (870 μm) images.

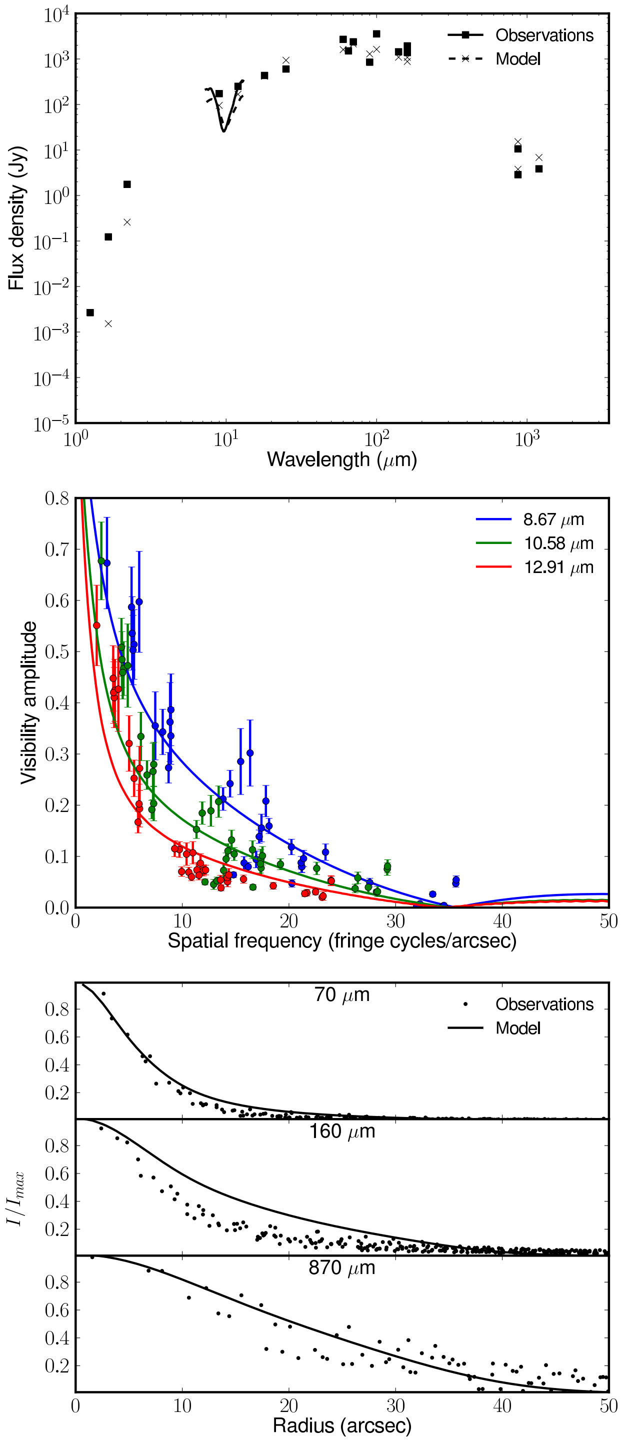

Figure 6.10: Model fits of the observational data for the far model. Figure notation is the same as for Fig. 6.9.

Table 6.4: Two-dimensional geometric fit parameters

Parameter	Best fit value
r_o	158 mas[1]
p	0.467
ϕ	112°
θ	59.7°
F_G/F_D	1.64
θ_G	143 mas[2]

Notes. [1] 552 AU at the near distance; 836 AU at the far distance. [2] 500 AU at the near distance; 757 AU at the far distance.

the center panel shows the modeled MIDI visibilities at three wavelengths; and the lower panel shows the radial distributions from Herschel (70 and 160 μm) and APEX (870 μm).

We defer a detailed discussion of the results to Sec. 6.5, but note the most prominent points of the model fits here. Both models reproduce the SED reasonably well at wavelengths longer than about 8 μm, but significantly underestimate the near-infrared flux levels. Both models also reproduce the *overall* visibility levels, as well as the spatial frequency of the zero crossing, however the far model provides a much better match, particularly at the two shorter wavelengths (red and green points in the middle panels of Figures 6.9 and 6.10). Finally, despite the good agreement of the radial profiles at wavelengths of 70 and 870 μm, both models overestimate the extent of emission at 160 μm, although the near model is in better agreement with the observed radial profile. The 160 μm filter might be contaminated by strong [C II] emission at 157 μm, detected in emission in the ISO LWS spectrum, which could alter the spatial profile of the brightness distribution seen in this broadband filter. However, since no spatially-resolved [C II] spectral map is available for AFGL 4176, this ad-hoc explanation is not beyond doubt.

6.4.2 Two-dimensional geometric modeling

While the one-dimensional approaches used above can provide useful insight, the deviations from spherical symmetry observed in the MIDI data should be explored. Such deviations can become especially clear in cases where multiple *uv* points have been measured with similar projected baselines (i.e., spatial frequencies), but differing position angles. Any significant variations in the visibility amplitude for a given spatial frequency will thus require deviations from a circularly-symmetric intensity distribution to be explained.

We see clear signs of such behavior for projected baselines longer than about 25 m, particularly for spatial frequencies larger than $\sim$ 10 fringe cycles/arcsec. For small variations in spatial frequency, we see visibility levels varying by over a factor of 5. Furthermore, there is a clear dependence on position angle: for measurements with $V < 0.2$, the visibility amplitude decreases with increasing position angle, while for measurements with $V > 0.2$, the visibility amplitude *decreases* with increasing position angle.

This behavior (visibility amplitude increasing with position angle for $V < 0.2$, and decreasing with position angle for $V > 0.2$) cannot be modeled with a simple elongated Gaussian. However, such a trend is possible in the case of a source distribution which has a well defined “edge” in its intensity distribution, causing a zero-crossing in the complex visibility with substantial power in the first side-lobe, for example a disk model.

To model this asymmetric behavior, we use a simple parameterized disk to match the dependence on position angle seen in our MIDI visibility measurements. We approximate the disk with a geometrically thin, optically thick blackbody emitter, with a temperature depending on

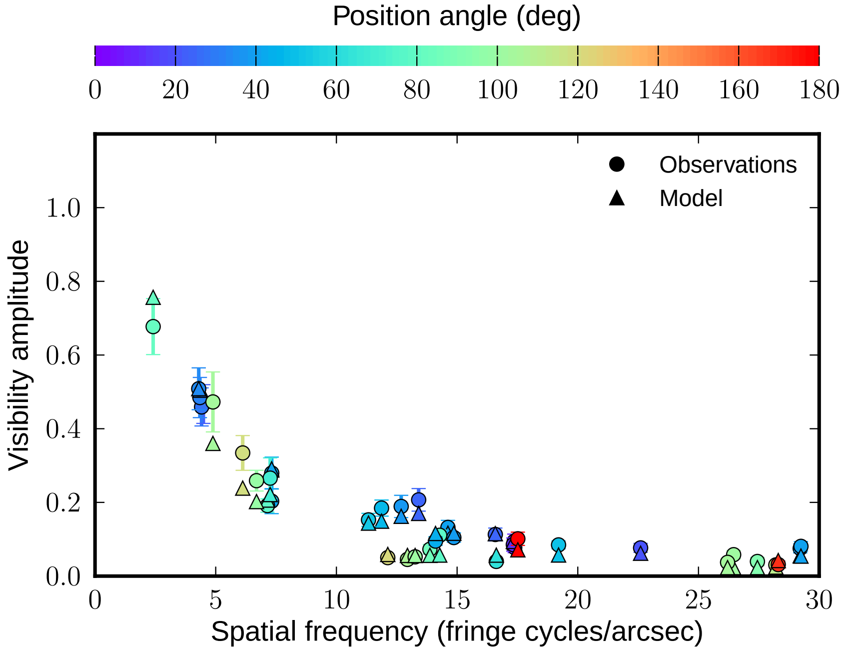

Figure 6.11: Geometric fit of a disk to the MIDI visibilities at 10.6 μm. The color coding indicates the position angle of the measurements; circles show the observed values of the visibility amplitude, while triangles show the model values at the corresponding coordinates in uv space.

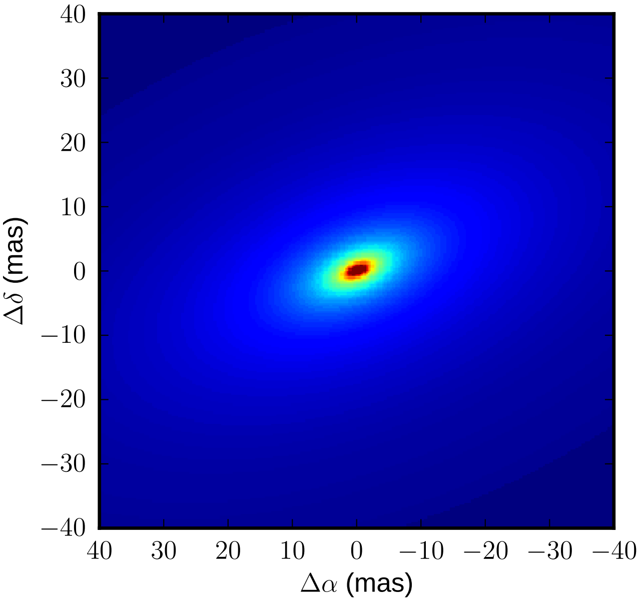

Figure 6.12: Image of the fit of the disk model to the mid-infrared visibilities at $\lambda = 10.6$ μm.

radius in the form of a power law in the form of

$$T(r) = T_f \left(\frac{r_f}{r}\right)^p \quad r_i < r \leq r_o, \tag{6.2}$$

where T_f is the temperature at a fix-point r_f, and r_i and r_o are the inner and outer disk radii, respectively. We adopt $T_f = 1500$ K, i.e. the approximate evaporation temperature of silicate dust, and let $r_f = \sqrt{L/4\pi\sigma T_f^4}$, i.e. the radius at which a blackbody of luminosity L will have a temperature of 1500 K. For the luminosity of our far model, $r_f = 37$ AU. We find that models in which the inner disk radius is at r_f provide poor fits to our MIDI data, and a substantially smaller inner radius is required. We adopt $r_i = 1$ AU, which is well below the spatial frequencies probed by our MIDI measurements. We thus implicitly assume the inner disk, consisting of gas, remains optically thick. This is in line with interferometric measurements of high-mass young stars, whose disk emission appears consistently more compact than expected for dusty, disk-only models (e.g. Monnier et al., 2005).

Finally, to account for the more symmetric behavior at shorter baselines, we include a one-dimensional component in the image intensity distribution in the form of a Gaussian centered on the disk. Thus, as fit parameters, we use the outer radius of the disk r_o, the disk inclination θ and position angle ϕ, the exponent p of the temperature power-law, the flux ratio F_G/F_D of the Gaussian component to the disk component, and the FWHM θ_G of the Gaussian component.

Results

The parameters that best fit the observed MIDI visibilities were derived from a brute-force grid search of parameter space, where we further refine the parameters of the best fit from the grid search by using the downhill simplex algorithm. We find that this disk model produces a very good fit to our data, and in Table 6.4, we summarize the parameters of our best-fit model to the MIDI visibilities at a wavelength of 10.6 μm. We show the resulting model visibilities as triangles in Fig. 6.11, and the model image in Fig. 6.12.

The observations are best described by a disk spanning up to several hundred AU, with the disk temperature decreasing gradually as a function of radius ($T \propto r^{-0.47}$). The disk is inclined ($\theta = 60°$), and the semi-major axis is oriented 112° east of north. Besides the disk component, a substantial halo is also present, with a FWHM size equal to about half the diameter of the disk, and a total flux at $\lambda = 10.6$ μm of 1.6 times the disk component.

6.5 Discussion

6.5.1 Comparison with previous models

In order to gauge the importance of including spatial information in the modeling process, we reconstructed the one-dimensional radiative transfer model for this object presented by Gürtler et al. (1991), using their dust composition and density structure together with the MoDust code used for our models. The model from Gürtler et al. (1991), which we refer to as G91, is a two-zone power-law model, and can be described using the density prescription from Eq. 6.1 if the parameters r_1, ρ_1 and p_1 are omitted. In Table 6.3, we show the parameters for the G91 model using this prescription.

In Fig. 6.13 we show the resulting SED, mid-infrared visibilities, and far-infrared/sub-mm radial intensity profiles. Note that Gürtler et al. (1991) fit only the SED to the extent it was known at the time, and that they did not have detailed spatial information (i.e. mid-IR interferometry and far-IR imaging) available. We indicate the measurements they had available by squares in Fig. 6.13, while the more recent Hi-GAL and ATLASGAL measurements, as well as the 1.2 mm measurement from Beltrán et al. (2006), are indicated by diamonds. Regarding the flux values available at the time of their study, we note in particular that their 1.3 mm measurement of 131 mJy was probably in error, as the position indicated in their Table 2 is more than $50''$ from the infrared source. More recently, for example, Beltrán et al. (2006) reported a 1.2 mm flux value of 3.86 Jy for the source, which seems to be in good agreement with the ATLASGAL flux level of 11.56 Jy at 870 μm which we present here.

In Fig. 6.14, we show the density laws used for both our near and far models, as well as the G91 model. To account for the different distances to the source used in each model (see Table 6.3), we express the dust density as a function of angular position on the sky. We also overlay the effective angular scales probed by our MIDI measurements, where have used the same color coding and grouping by projected baseline as in Fig. 6.1.

For the near and far models, we see that the inner shell with enhanced density is probed primarily by the longest baseline measurements, while shorter baselines probe successively larger scales, out to about $0\rlap{.}''1$. Because this inner region is completely absent in the G91 model, the mid-IR visibilities at longer baselines are vastly under-predicted by this model. This is despite the relatively good fit to the SED (with the exception of the sub-mm/mm regime), as well as the 70 and 160 μm radial profiles, which only emphasizes the importance of including spatial information at different scales into such radiative transfer models.

6.5.2 The disk around AFGL 4176

The mid-infrared interferometric observations presented in this chapter provide the first evidence for any signs of asymmetry in this deeply-embedded MYSO to date. Using a model consisting of a symmetric halo and an optically thick, geometrically thin disk, we find that a disk with an inclination angle of 60° and a position angle of the semi-major axis of 112° east of north provides an excellent fit to our MIDI data. The best-fit temperature profile of the disk is $T \propto r^{-0.47}$. At longer wavelengths, the deviation from spherical symmetry in our MIDI data is much less pronounced, which suggests that the emission from the disk is dominated by a more spherical halo component at these wavelengths.

Nevertheless, because of the wavelength range, mid-infrared observations probe primarily cooler material ($\sim 200 - 600$ K), expected to be well away from the hotter, inner circumstellar regions where signs of accretion onto the central star may be present. Furthermore, the inner radius of the disk around AFGL 4176, adopted in this work to be 1 AU, cannot be determined by our observations, as it remains unresolved by the MIDI data. In this context, near-infrared interferometric observations which probe these inner regions would make a superb compliment to the current data set.

On the other hand, the lack of detection of an outflow component, or any other larger-scale asymmetries, remains an open question. This may, for example, suggest that the object is still at a very early stage in the formation process, and that large-scale outflows have not had time to form. In any case, far-IR/sub-mm interferometric observations with ALMA may provide the key to bridging the symmetric structure on scales of tens to hundreds of thousands of AU to the asymmetries observed at tens to hundreds of AU.

6.5.3 Comparison with other MYSOs

To date, very few MYSOs have been studied on scales of tens to hundreds of AUs. Here we compare our results with similar studies of five other MYSOs. In Table 6.5 we list the luminosities, the depth of the 10 μm silicate absorption feature, whether or not any compact H II region is present, and whether or not any outflows have been detected, which can be useful for independently constraining disk geometry. As previously noted, however, in the case of

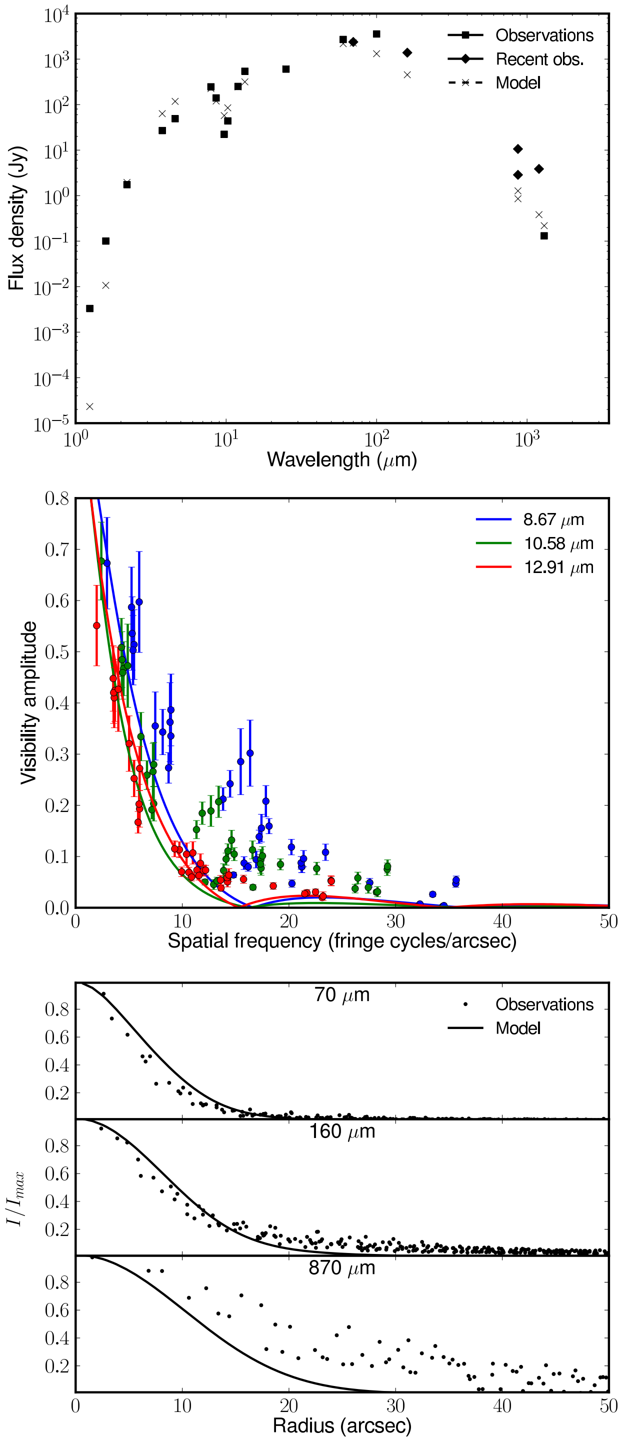

Figure 6.13: Fit to model by Gürtler et al. (1991). Figure notation is the same as for Fig. 6.9, but in the top panel of the SED we distinguish between flux values available today (filled diamonds) and those available at the time of the Gürtler et al. (1991) study (filled squares).

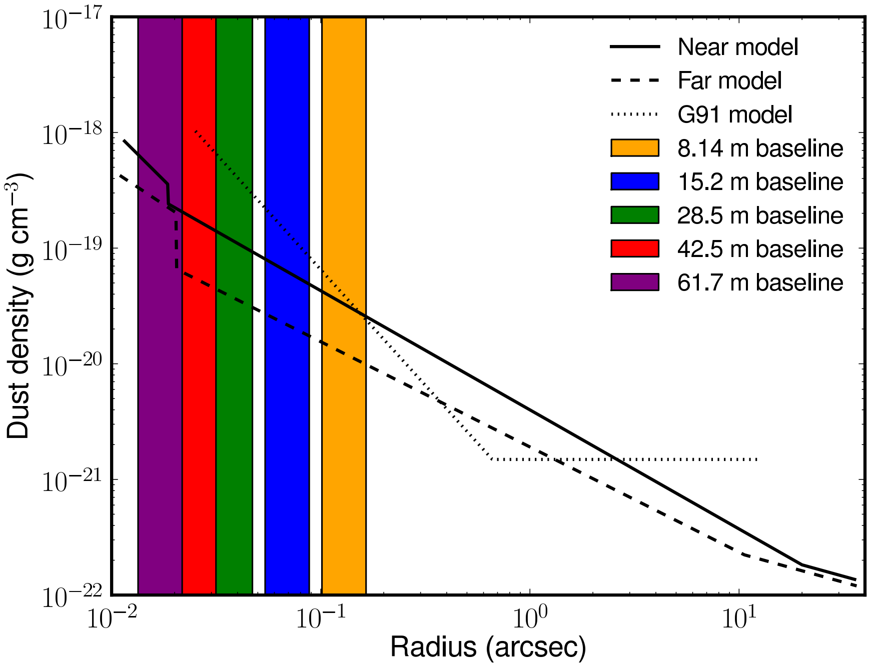

Figure 6.14: Density laws used for the three radiative transfer models, expressed as a function of angular distance on the sky to account for the difference in distance to the source each model. The colored rectangles show the spatial scales $\lambda/2B$ covered by the MIDI observations, and the color coding matches the average baselines for the groups indicated in Fig. 6.1.

Table 6.5: Summary of parameters for several MYSOs studied on scales of $\sim 10-100$ AU. All values approximate.

MYSO	D (kpc)	L ($L_\odot$)	A_V (mag)	H II region present?	Outflows present?	References
AFGL 4176	3.5 – 5.3	10^5	100	Yes	?	1, 2, 3
W33A	3.8	10^5	280	Yes	Yes	4
NGC 3603 IRS 9A	7	10^5	?	Yes	?	5
AFGL 2136	1.7	$2-3\times10^4$	100	Yes	Yes	6, 7
IRAS 13481-6124	3.2	3×10^4	40?	Yes	Yes	8
M8E-IR	1.5	7×10^3	30	No	Yes	9

References. (1) This work; (2) Phillips et al. (1998); (3) Ellingsen et al. (2005); (4) de Wit et al. (2010); (5) Vehoff et al. (2010); (6) de Wit et al. (2011); (7) Follert (2011); (8) Kraus et al. (2010); (9) Linz et al. (2009).

AFGL 4176, no outflow components have been detected (De Buizer, 2003; De Buizer et al., 2009). For a broader discussion of these and other sources, we refer to the work by Grellmann et al. (2011).

The sources W33A and NGC 3603 IRS 9A have similar luminosities to AFGL 4176, on the order of $10^5\ L_\odot$, and both have associated hyper-compact H II regions. However, IRS 9A seems to be much less embedded: besides having an optical component, the N-band spectrum shows no 10 μm silicate feature at all. At mid-infrared wavelengths, the source is very extended, and completely overresolved in MIDI observations probing $\sim$ 200 AU scales (Vehoff et al., 2010). W33A, on the other hand, could be even more embedded than AFGL 4176 ($A_V \gtrsim 200$ mag, de Wit et al., 2010), but the N-band visibility levels are poorly determined due to the low amount of (correlated) flux in the deep 10 μm silicate absorption feature. The source was modeled by de Wit et al. (2010), who concluded that most of the mid-infrared emission on scales of 10^2 AU is dominated by collimated outflow cones, without compelling evidence for significant emission from a dusty disk.

At an estimated luminosity of $\sim 5 \times 10^4\ \mathrm{L}_\odot$, the SED of AFGL 2136 closely resembles that of AFGL 4176, including a similar depth of the 10 μm silicate feature (Smith et al., 2000). Using visibility measurements obtained with MIDI, both de Wit et al. (2011) and Follert (2011) reported mid-IR emission scales of $\sim$ 200 AU, while Follert (2011) found an elongated structure at these scales, parallel to earlier predictions of disk orientation.

Despite having a lower luminosity, on the order of $3 \times 10^4\ L_\odot$, the SED of IRAS13481-6124 is somewhat similar to that of AFGL 4176, although the 10 μm silicate feature is much shallower in IRAS13481-6124. Kraus et al. (2010) discovered a molecular outflow, and used near-IR interferometric observations to resolve an elongated structure oriented perpendicular to the outflow direction. The extended outflow shocks detected at near-IR wavelengths at large distances from the source (Stecklum et al. 2010[3]), as well as the radiative transfer models presented by Kraus et al. (2010), suggest the disk is strongly inclined. However, the 20 $\mathrm{M}_\odot$ (gas + dust mass) disk at scales of 5-150 AU proposed by Kraus et al. (2010) is clearly a fundamentally different model than the structures we present here for AFGL 4176. For comparison, the dust mass enclosed in the near and far models for $r < 150$ AU is $8 \times 10^{-6}\ \mathrm{M}_\odot$ and $4 \times 10^{-5}\ \mathrm{M}_\odot$, respectively, although a direct comparison between studies using near- and mid-IR interferometric measurements is difficult.

Finally, the source with the lowest luminosity, M8E-IR, has an overall extinction of $A_V \approx$ 30 mag, as determined from the depth of the 10 μm silicate feature (Linz et al., 2009). Outflow signatures have been detected for this source (Mitchell et al., 1988). No cm continuum emission has been detected directly coinciding with the IR object. This lack of an ultra-compact H II region might be related to the hypothesis of a bloated, cooler central object, as suggested by Linz et al. (2009).

Given the small selection of sources for which this information is available, it is not possible to infer clear, empirical correlations between the properties listed in Table 6.5. Of the sources presented, none of them seem to be direct analogues of AFGL 4176, however W33A might be the closest match in terms of luminosity, SED and emission scales at mid-infrared wavelengths. Suggestions by de Wit et al. (2011) and Linz et al. (2011) indicate that mid-IR interferometric observations of at least some MYSOs may be heavily influenced by outflow components. On the other hand, the mid-IR visibilities presented by Follert (2011) apparently trace the disk structure of AFGL 2136. Taken together, it becomes clear that the mid-IR emission structure of MYSOs at scales of tens to hundreds of AUs can be complex, and caution should be exercised in interpreting data sets with limited *uv* coverage.

---

[3] http://www.jcu.edu.au/hmsf10/Presentations/Monday/Session3/Stecklum.pdf

6.6 Summary and conclusions

In this chapter, we reported on spatially resolved observations and modeling of the massive young stellar object AFGL 4176. We presented the largest amount of N-band visibilities for any MYSO to date, obtained with MIDI on the ESO/VLTI, together with maps of extended emission at 70 and 160 μm from the Hi-GAL survey on the Herschel Space Observatory and 870 μm imaging from the ATLASGAL survey with the APEX telescope.

With the exception of the mid-infrared interferometric measurements presented in this work, the observational data available for this deeply-embedded object do not provide indications of asymmetry or preferred geometry. In view of this, we used spherically symmetric radiative transfer models, consisting of an envelope with a density enhancement at its inner edge, to model the source. Using these one-dimensional models, we were able to satisfactorily reproduce, simultaneously, the SED and spatial structure at mid-IR through mm wavelengths.

However, the one-dimensional models by definition cannot reproduce the asymmetries present in the MIDI data. We therefore modeled these data separately, using a multiple-component geometric analysis. We interpret the MIDI observations in terms of a circumstellar disk around AFGL 4176. If this disk hypothesis is correct, it would make AFGL 4176 the most luminous (massive) young star to have a disk detected around it to date. However, beyond initial detection, much remains to be clarified regarding the nature and extent of the disk, making this object a top priority for additional interferometric imaging, at both near-IR and far-IR/sub-mm wavelengths.

Acknowledgements. I would like to thank the referee, Dr. Koji Murakawa, for insightful critique during the review process of the publication which this chapter is based on. I also thank Christoph Leinert, Svitlana Zhukovska, Dima Semenov and Keiichi Ohnaka for useful discussions, and Frederic Schuller, for generously making the reduced ATLASGAL observations available to us.

References

Beltrán, M. T., Brand, J., Cesaroni, R., et al.: 2006, Search for massive protostar candidates in the southern hemisphere. II. Dust continuum emission. *Astronomy and Astrophysics* **447**, 221–233

Bertin, E.: 2010, SWarp: Resampling and Co-adding FITS Images Together, in *Astrophysics Source Code Library, record ascl:1010.068*, p. 10068

Beuther, H., Leurini, S., Schilke, P., et al.: 2007, Interferometric multi-wavelength (sub)millimeter continuum study of the young high-mass protocluster IRAS 05358+3543. *Astronomy and Astrophysics* **466**, 1065–1076

Boley, P., van Boekel, R., Linz, H., et al.: 2011, Observations and modeling of the massive young star AFGL 4176: From large scales to small. *arXiv 1111.0807*

Boley, P. A., Linz, H., van Boekel, R., et al.: 2012, On the massive young stellar object AFGL 4176. High-spatial-resolution multi-wavelength observations and modeling. *Astronomy and Astrophysics* **547**, A88

Bouwman, J., Meeus, G., de Koter, A., et al.: 2001, Processing of silicate dust grains in Herbig Ae/Be systems. *Astronomy and Astrophysics* **375**, 950–962

Brand, J. and Blitz, L.: 1993, The Velocity Field of the Outer Galaxy. *Astronomy and Astrophysics* **275**, 67–+

Caswell, J. L., Kesteven, M. J., Stewart, R. T., Milne, D. K., and Haynes, R. F.: 1992, G308.8-0.1 - an unusual supernova remnant containing a short-period pulsar, PSR J1341-6220. *Astrophysical Journal Letters* **399**, L151–L153

De Buizer, J. M.: 2003, Testing the circumstellar disc hypothesis: a search for H_2 outflow signatures from massive young stellar objects with linearly distributed methanol masers. *Monthly Notices of the Royal Astronomical Society* **341**, 277–298

De Buizer, J. M., Redman, R. O., Longmore, S. N., Caswell, J., and Feldman, P. A.: 2009, SiO outflow signatures toward massive young stellar objects with linearly distributed methanol masers. *Astronomy and Astrophysics* **493**, 127–143

de Wit, W. J., Hoare, M. G., Oudmaijer, R. D., and Lumsden, S. L.: 2010, The origin of mid-infrared emission in massive young stellar objects: multi-baseline VLTI observations of W33A. *Astronomy and Astrophysics* **515**, A45

de Wit, W. J., Hoare, M. G., Oudmaijer, R. D., et al.: 2011, Mid-infrared interferometry towards the massive young stellar object CRL 2136: inside the dust rim. *Astronomy and Astrophysics* **526**, L5

Duschl, W. J., Gail, H., and Tscharnuter, W. M.: 1996, Destruction processes for dust in protoplanetary accretion disks.. *Astronomy and Astrophysics* **312**, 624–642

Ellingsen, S. P., Shabala, S. S., and Kurtz, S. E.: 2005, Extended emission associated with young HII regions. *Monthly Notices of the Royal Astronomical Society* **357**, 1003–1012

Feautrier, P.: 1964, Sur la resolution numerique de l'equation de transfert.. *Comptes Rendus Academie des Sciences (serie non specifiee)* **258**, 3189–+

Follert, R.: 2011, *The atmospheric piston simulator for LINC-NIRVANA and Interferometric observations of massive young stellar objects*, *Ph.D. thesis*, University of Heidelberg, Germany

Follert, R., Linz, H., Stecklum, B., et al.: 2010, Mid-infrared interferometry of massive young stellar objects. II. Evidence for a circumstellar disk surrounding the Kleinmann-Wright object. *Astronomy and Astrophysics* **522**, A17

Fontani, F., Beltrán, M. T., Brand, J., et al.: 2005, Search for massive protostellar candidates in the southern hemisphere. I. Association with dense gas. *Astronomy and Astrophysics* **432**, 921–935

Foster, J. B., Jackson, J. M., Barnes, P. J., et al.: 2011, The Millimeter Astronomy Legacy Team 90 GHz (MALT90) Pilot Survey. *Astrophysical Journal Supplement Series* **197**, 25

Grave, J. M. C. and Kumar, M. S. N.: 2009, Spitzer-IRAC GLIMPSE of high mass protostellar objects. II. SED modelling of a bona fide sample. *Astronomy and Astrophysics* **498**, 147–159

Grellmann, R., Ratzka, T., Kraus, S., et al.: 2011, Mid-infrared interferometry of the massive young stellar object NGC 2264 IRS 1. *Astronomy and Astrophysics* **532**, A109

Gürtler, J., Henning, T., Krügel, E., and Chini, R.: 1991, Dust continuum radiation from luminous young stellar objects. *Astronomy and Astrophysics* **252**, 801–811

Henning, T., Friedemann, C., Guertler, J., and Dorschner, J.: 1984, A catalogue of extremely young, massive and compact infrared objects. *Astronomische Nachrichten* **305**, 67–78

Henning, T., Pfau, W., and Altenhoff, W. J.: 1990, Infrared and radio emission from very young and massive stellar objects. *Astronomy and Astrophysics* **227**, 542–552

Henning, T. and Stognienko, R.: 1996, Dust opacities for protoplanetary accretion disks: influence of dust aggregates.. *Astronomy and Astrophysics* **311**, 291–303

Hofner, P., Wiesemeyer, H., and Henning, T.: 2001, A High-Velocity Molecular Outflow from the G9.62+0.19 Star-forming Region. *Astrophysical Journal* **549**, 425–432

Kemper, F., Waters, L. B. F. M., de Koter, A., and Tielens, A. G. G. M.: 2001, Crystallinity versus mass-loss rate in asymptotic giant branch stars. *Astronomy and Astrophysics* **369**, 132–141

Kraus, S., Hofmann, K.-H., Menten, K. M., et al.: 2010, A hot compact dust disk around a massive young stellar object. *Nature* **466**, 339–342

Kurucz, R. L.: 1979, Model atmospheres for G, F, A, B, and O stars. *Astrophysical Journal Supplement Series* **40**, 1–340

Laor, A. and Draine, B. T.: 1993, Spectroscopic constraints on the properties of dust in active galactic nuclei. *Astrophysical Journal* **402**, 441–468

Leinert, C., Haas, M., Ábrahám, P., and Richichi, A.: 2001, Halos around Herbig Ae/Be stars - more common than for the less massive T Tauri stars. *Astronomy and Astrophysics* **375**, 927–936

Leinert, C., van Boekel, R., Waters, L. B. F. M., et al.: 2004, Mid-infrared sizes of circumstellar disks around Herbig Ae/Be stars measured with MIDI on the VLTI. *Astronomy and Astrophysics* **423**, 537–548

Levine, E. S., Heiles, C., and Blitz, L.: 2008, The Milky Way Rotation Curve and Its Vertical Derivatives: Inside the Solar Circle. *Astrophysical Journal* **679**, 1288–1298

Linz, H., Follert, R., Boley, P. A., et al.: 2011, MIDI interferometry of massive YSOs: Updates on the MPIA programme. *arXiv 1111.0821*

Linz, H., Henning, T., Feldt, M., et al.: 2009, Mid-infrared interferometry of massive young stellar objects. I. VLTI and Subaru observations of the enigmatic object M8E-IR. *Astronomy and Astrophysics* **505**, 655–661

Malfait, K., Waelkens, C., Bouwman, J., de Koter, A., and Waters, L. B. F. M.: 1999, The ISO spectrum of the young star HD 142527. *Astronomy and Astrophysics* **345**, 181–186

Martins, F., Schaerer, D., and Hillier, D. J.: 2005, A new calibration of stellar parameters of Galactic O stars. *Astronomy and Astrophysics* **436**, 1049–1065

Men'shchikov, A. B. and Henning, T.: 1997, Radiation transfer in circumstellar disks.. *Astronomy and Astrophysics* **318**, 879–907

Mitchell, G. F., Allen, M., Beer, R., et al.: 1988, The detection of high-velocity outflows from M8E-IR. *Astrophysical Journal Letters* **327**, L17–L21

Molinari, S., Swinyard, B., Bally, J., et al.: 2010, Hi-GAL: The Herschel Infrared Galactic Plane Survey. *Publications of the Astronomical Society of the Pacific* **122**, 314–325

Monnier, J. D., Millan-Gabet, R., Billmeier, R., et al.: 2005, The Near-Infrared Size-Luminosity Relations for Herbig Ae/Be Disks. *Astrophysical Journal* **624**, 832–840

Ossenkopf, V. and Henning, T.: 1994, Dust opacities for protostellar cores. *Astronomy and Astrophysics* **291**, 943–959

Ott, S.: 2010, The Herschel Data Processing System — HIPE and Pipelines — Up and Running Since the Start of the Mission, in *Astronomical Data Analysis Software and Systems XIX*, Y. Mizumoto, K.-I. Morita, & M. Ohishi (ed.), Vol. 434 of *Astronomical Society of the Pacific Conference Series*, pp 139–+

Phillips, C. J., Norris, R. P., Ellingsen, S. P., and McCulloch, P. M.: 1998, Methanol masers and their environment at high resolution. *Monthly Notices of the Royal Astronomical Society* **300**, 1131–1157

Pilbratt, G. L., Riedinger, J. R., Passvogel, T., et al.: 2010, Herschel Space Observatory. An ESA facility for far-infrared and submillimetre astronomy. *Astronomy and Astrophysics* **518**, L1+

Poglitsch, A., Waelkens, C., Geis, N., et al.: 2010, The Photodetector Array Camera and Spectrometer (PACS) on the Herschel Space Observatory. *Astronomy and Astrophysics* **518**, L2+

Reid, M. J., Menten, K. M., Zheng, X. W., et al.: 2009, Trigonometric Parallaxes of Massive Star-Forming Regions. VI. Galactic Structure, Fundamental Parameters, and Noncircular Motions. *Astrophysical Journal* **700**, 137–148

Roussel, H.: 2012, Scanamorphos: a map-making software for Herschel and similar scanning bolometer arrays. *arXiv 1205.2576*

Saito, H., Mizuno, N., Moriguchi, Y., et al.: 2001, The Most Massive $C^{18}O$ Molecular Complex in Centaurus and Star Formation Therein. *Publications of the Astronomical Society of Japan* **53**, 1037–1051

Saito, R. K., Hempel, M., Minniti, D., et al.: 2012, VVV DR1: The first data release of the Milky Way bulge and southern plane from the near-infrared ESO public survey VISTA variables in the Vía Láctea. *Astronomy and Astrophysics* **537**, A107

Schuller, F., Menten, K. M., Contreras, Y., et al.: 2009, ATLASGAL - The APEX telescope large area survey of the galaxy at 870 μm. *Astronomy and Astrophysics* **504**, 415–427

Semenov, D., Henning, T., Helling, C., Ilgner, M., and Sedlmayr, E.: 2003, Rosseland and Planck mean opacities for protoplanetary discs. *Astronomy and Astrophysics* **410**, 611–621

Siringo, G., Kreysa, E., Kovács, A., et al.: 2009, The Large APEX BOlometer CAmera LABOCA. *Astronomy and Astrophysics* **497**, 945–962

Smith, C. H., Wright, C. M., Aitken, D. K., Roche, P. F., and Hough, J. H.: 2000, Studies in mid-infrared spectropolarimetry - II. An atlas of spectra. *Monthly Notices of the Royal Astronomical Society* **312**, 327–361

Tan, J. C.: 2004, The Becklin-Neugebauer Object as a Runaway B Star, Ejected 4000 Years Ago from the θ^1 Orionis C System. *Astrophysical Journal Letters* **607**, L47–L50

Thamm, E., Steinacker, J., and Henning, T.: 1994, Ambiguities of parametrized dust disk models for young stellar objects. *Astronomy and Astrophysics* **287**, 493–502

Vehoff, S., Hummel, C. A., Monnier, J. D., et al.: 2010, Mid-infrared interferometry of the massive young stellar object NGC 3603 - IRS 9A. *Astronomy and Astrophysics* **520**, A78

Wheelwright, H. E., Oudmaijer, R. D., de Wit, W. J., et al.: 2010, Probing discs around massive young stellar objects with CO first overtone emission. *Monthly Notices of the Royal Astronomical Society* **408**, 1840–1850

Chapter 7

Future outlook

As described in Chapter 2, high-spatial-resolution observations at near- and mid-infrared wavelengths form a critical and irreplaceable tool for addressing the question of how massive stars form. In particular, the diffraction limit of single-telescope imaging, which can be overcome via long-baseline interferometry, severely restricts the information which can be gathered on these distant objects. Thus, optical/infrared long-baseline interferometers like the European Southern Observatory's Very Large Telescope Interferometer (VLTI) and Georgia State University's Center for High-Angular-Resolution Astronomy (CHARA) array are essential to the field.

To date, the VLTI is the only such facility to successfully observe MYSOs (de Wit, 2012). However, the mid-infrared instrument MIDI at the VLTI, with which the vast majority of the observational material presented in this thesis was obtained, is planned to be decommissioned within the coming year. As the only other long-baseline mid-infrared interferometer in the world (ISI) is not suitable for observations of faint targets, studies similar those presented in this thesis will have to wait for the next generation of mid-infrared interferometric instruments to come online.

However, the wait should be worth it. In particular, one of these next-generation instruments, known as MATISSE (Lopez et al., 2008), is planned to be a direct successor to MIDI at the VLTI. Because it will utilize four telescopes at once (compared to two with MIDI), it will be able to simultaneously observe *six* visibility points (compared to *one* with MIDI) and *four* closure phases (compared to *none* with MIDI). This will finally make model-independent image reconstruction at mid-infrared wavelengths feasible, and interpretation of interferometric data will no longer be hostage to simplified geometric models. A further limitation which will be lifted, with the availability of phase information, is the *de facto* necessity for axisymmetric models (*all* of the models examined in this thesis, for example, include axial symmetry as a basic assumption).

No less important than the greatly-expanded *uv* coverage is the additional wavelength coverage which MATISSE will provide, being able to observe in the L, M and N bands (i.e., 3–13 μm) at baselines up to the maximum provided by the VLTI infrastructure (i.e., > 128 m). Currently, observations with MIDI are limited to the N-band atmospheric window, which owes its existence to the details of H_2O and CO_2 absorption properties. By a truly cosmic coincidence, the broad 10 μm silicate feature, which arises due to stretching modes in molecules of interstellar/circumstellar dust, lies at exactly the same wavelength range. While this may be regarded as highly fortuitous, as it gives one access to the dust composition, column densities of absorbing material, etc., the current impossibility of performing observations at mid-infrared wavelengths *outside of the silicate feature* complicates interpretations of the observational data. Additionally, there are many other interesting features, including those arising from ices, gas lines and PAH molecules which lie at L and M-band wavelengths. So far, these wavelength ranges have yet to be opened to long-baseline interferometers.

MATISSE is planned to begin operations at the VLTI in 2016 or 2017. In the meantime, interferometric observations of MYSOs will remain limited to near-infrared wavelengths[1], with continued efforts on AMBER; hopefully, the CHARA array (ten Brummelaar et al., 2005) will be utilized for the study of MYSOs in the future. Any other attempts to resolve the circumstellar disks around massive stars at infrared wavelengths will have to rely on other techniques.

In the near future, the Large Binocular Telescope Interferometer (LBTI) is expected to begin science operations. Although many aspects of the capabilities and operating modes of the various interferometric instruments remain unclear at this point[2], it is worth considering the prospects in a broad sense. The maximum possible baseline of 23 m means the interferometer will have a resolution of $\lambda/2B \approx 45$ mas at a wavelength of 10 μm. This will, however, be inadequate for studying the compact components of most MYSOs: as seen in Chapter 4, the typical angular sizes of these compact components are on the order of 10–20 mas. The European Extremely Large Telescope (E-ELT), which is planned to begin operations sometime in the 2020s, will suffer from the same angular resolution problem as the LBTI. Although the planned METIS instrument (Brandl et al., 2008) will offer attractive wavelength coverage (3–13 μm), imaging and spectroscopic capabilities, the 40 m E-ELT will deliver essentially the same angular resolution as the LBTI[3]. Thus, mid-infrared studies of MYSOs with the LBTI and E-ELT will be largely limited to the extended envelopes.

Finally, it is worth mentioning that interferometry is not the only way of overcoming the barrier on spatial resolution imposed by the diffraction limit. The technique of spectroastrometry uses extremely high *spectral* resolution to map small photocenter shifts of spectral lines, and can reach an accuracy down to a level of $\lesssim 1$ mas. This technique can be applied today, using existing facilities: for example, Pontoppidan et al. (2008) used CRIRES on the VLT to reveal gaps in gaseous planetary disks around low-mass stars, and Wheelwright et al. (2010) used CRIRES and Phoenix (Gemini South Observatory) to measure emission lines from gaseous molecules around MYSOs, which seem to be consistent with models for circumstellar disks. Further applications of this technique to MYSOs are ongoing (e.g. Ilee et al., 2012), and additional exciting results can be expected to appear soon.

---

[1] This statement, of course, applies only to so-called "optical" interferometry. As mentioned briefly in Chapter 2, there is rapid progress in the application sub-mm interferometric observations to the study of MYSOs.

[2] Long-term plans exist to equip the LBTI with a mid-infrared Fizeau imaging interferometer (Mainzer et al., 2006). Currently it is not clear, however, if and when such a new instrument mode might be installed at the LBT (T. Herbst, priv. comm.).

[3] In fact, the resolution of the E-ELT *operating as a single-aperture telescope*, given now by $\sim 1.22\lambda/B \approx 63$ mas at 10 μm, will be slightly worse than the LBTI.

References

Brandl, B. R., Lenzen, R., Pantin, E., et al.: 2008, METIS: the mid-infrared E-ELT imager and spectrograph, in *Ground-based and Airborne Instrumentation for Astronomy II*, I. S. McLean and M. M. Casali (eds.), Vol. 7014 of *Society of Photo-Optical Instrumentation Engineers (SPIE) Conference Series*

de Wit, W. J.: 2012, Advances in Understanding Young High-Mass Stars Using Optical Interferometry, in *Circumstellar Dynamics at High Resolution*, A. C. Carciofi and T. Rivinius (eds.), Vol. 464 of *Astronomical Society of the Pacific Conference Series*, p. 329

Ilee, J. D., Wheelwright, H. E., Oudmaijer, R. D., et al.: 2012, CO bandhead emission of massive young stellar objects: determining disc properties. *arXiv 1212.0554*

Lopez, B., Antonelli, P., Wolf, S., et al.: 2008, MATISSE: perspective of imaging in the mid-infrared at the VLTI, in *Optical and Infrared Interferometry*, M. Schöller, W. C. Danchi, and F. Delplancke (eds.), Vol. 7013 of *Society of Photo-Optical Instrumentation Engineers (SPIE) Conference Series*

Mainzer, A. K., Young, E., Hong, J., et al.: 2006, MegaMIR: a Fizeau thermal infrared camera for the LBTI, in *Ground-based and Airborne Instrumentation for Astronomy*, I. S. McLean and I. Masanori (eds.), Vol. 6269 of *Society of Photo-Optical Instrumentation Engineers (SPIE) Conference Series*

Pontoppidan, K. M., Blake, G. A., van Dishoeck, E. F., et al.: 2008, Spectroastrometric Imaging of Molecular Gas within Protoplanetary Disk Gaps. *Astrophysical Journal* **684**, 1323–1329

ten Brummelaar, T. A., McAlister, H. A., Ridgway, S. T., et al.: 2005, First Results from the CHARA Array. II. A Description of the Instrument. *Astrophysical Journal* **628**, 453–465

Wheelwright, H. E., Oudmaijer, R. D., de Wit, W. J., et al.: 2010, Probing discs around massive young stellar objects with CO first overtone emission. *Monthly Notices of the Royal Astronomical Society* **408**, 1840–1850

Chapter 8

Summary and conclusions

In this thesis, I have investigated the nature of circumstellar material around massive young stellar objects (MYSOs) from an observational standpoint, relying heavily on spatially-resolved observations at near- and mid-infrared wavelengths. Thanks to long-baseline interferometers like the Very Large Telescope Interferometer (VLTI), this is the first time in the history of the field when it has become possible to *spatially resolve* MYSOs down to the level of tens of AUs.

The survey of 20 MYSOs with the mid-infrared interferometric instrument MIDI at the VLTI, presented in Chapter 4, represents the largest collection of such objects with observations which probe spatial scales capable of resolving potential circumstellar disks. Thus, the problem of circumstellar disks around massive stars is no longer strictly limited to theoretical predictions and computer simulations. However, the field of spatially-resolved observations of young massive stars is still very much in its infancy. Although huge advancements in telescope facilities have been made in the last decades, a significant level of ambiguity remains in interpreting interferometric observations at infrared wavelengths. Some of the MYSOs studied as part of the aforementioned survey show very strong indications for the presence of a circumstellar disk. Others show structure which can be readily attributed to an outflow component, but the presence or absence of an actual disk remains unclear. Finally, for a few objects, it is clear that some kind of circumstellar material is present, but its nature and role in the system, for the time being, remain difficult to decipher.

Detailed studies of two of the objects for which a particularly large volume of data was obtained, IRAS 13481-6124 and AFGL 4176, are presented in Chapters 5 and 6, respectively. These studies move beyond just mid-infrared wavelengths, with the first including near-infrared (K band) infrared observations, and the second including spatially-resolved observations at far-infrared through sub-mm wavelengths.

Analysis of the temperature profile of the disk of IRAS 13481-6124 indicates that it is *much* steeper than one would naively predict from established theoretical disk models. Although the steep profile can be qualitatively explained in terms of the strong influence the inner rim of the disk is expected to have, this is by far not the only explanation. Alternative scenarios may be provided in the future by detailed radiative transfer models, as well as additional observations at other wavelengths (e.g. near-IR spectroastrometry or sub-mm interferometry).

In the case of AFGL 4176, the mid-infrared interferometric observations were able to provide the first indications of *any* kind of asymmetry in this very luminous ($L \gtrsim 10^5$ $\mathrm{L}_\odot$), envelope-enshrouded object. The interferometric observations are consistent with a very large circumstellar disk, extending out to a radius of a few hundred AU. The envelope of this source (resolved by the Herschel Space Observatory and APEX sub-mm telescope), which contains the vast majority of the mass in the system, is several orders of magnitude larger than the disk ($\gtrsim 100\,000$ AU), and appears mostly spherical. The one-dimensional radiative transfer models presented in

Chapter 6 reproduce both the spectral energy distribution and wavelength-dependent spatial extent of the source quite well. However, the transition from the large-scale, one-dimensional appearance down to the small-scale, two-dimensional structures remains poorly constrained by observations.

As mentioned in Chapter 7, direct analogs to the mid-infrared interferometric studies presented here will be impossible until the arrival of the next generation of VLTI instrumentation in about 2017. However, the observations and results presented in this thesis will be of lasting use, both in continuing studies of these specific objects, and in building a broader understanding of massive young stellar objects on the whole.

Acknowledgements

It is my pleasure to thank Hendrik Linz and Roy van Boekel for the integral part they played at all stages of the research presented in this thesis. I also want to express my gratitude to Thomas Henning, who contributed a great deal, and, together with Cornelius Dullemond, graciously agreed to referee this thesis during the winter holiday period of 2012–2013.

I am of course grateful to all my coauthors (listed at the beginning of Chapters 4–6), but here I would like to specifically acknowledge the contributions of Jeroen Bouwman, Willem-Jan de Wit, Stefan Kraus and Andrey Sobolev.

Financial support during the course of my doctoral studies was provided by the Max Planck Society through the IMPRS program, and via the Max Planck Institute for Astronomy in various forms. The binding of this thesis was supported by the Ernst Patzer Foundation.